

Aus der Klinik für Strahlentherapie und Radioonkologie
der Medizinischen Fakultät Mannheim
(Direktor: Dr. med. Michael Ehmann)

**EVALUATION OF AN ADAPTIVE RADIATION THERAPY
WORKFLOW FOR HYPOFRACTIONATED PROSTATE CANCER
TREATMENT BASED ON SYNTHETIC CONE-BEAM COMPUTED
TOMOGRAPHY**

Inauguraldissertation
zur Erlangung des Doctor scientiarum humanarum (Dr. sc. hum.)
der
Medizinischen Fakultät Mannheim
der Ruprecht-Karls-Universität
zu
Heidelberg

vorgelegt von
Miriam Tatjana Eckl
aus
Ludwigshafen am Rhein
2021

Dekan: Prof. Dr. med. Sergij Goerd
Referent: Prof. Dr. Dr. h.c. Frederik Wenz

TABLE OF CONTENTS

	Page
TABLE OF CONTENTS	I
LIST OF ABBREVIATIONS	III
1 INTRODUCTION	1
2 MATERIALS AND METHODS	9
2.1 Generation of a pelvic synthetic CT model	10
2.1.1 Patient population	10
2.1.2 Architecture of the cycle-generative adversarial network.....	11
2.2 Validation of the pelvic sCT model	13
2.2.1 Treatment workflow	13
2.2.2 Image quality of sCT	14
2.2.3 Segmentation accuracy of sCT	15
2.2.4 Dosimetric accuracy of sCT	18
2.3 Evaluation of adaptive treatment planning on sCT	20
2.3.1 The PACE-C trial	20
2.3.2 Study design and workflow	21
2.3.3 SBRT dose criteria.....	24
2.3.4 Segment aperture morphing and adaptive replanning approaches ...	25
2.3.5 Dosimetric and statistical evaluation.....	27
3 RESULTS.....	30
3.1 Evaluation of sCT	30
3.1.1 Image quality	30
3.1.2 Segmentation accuracy	33

3.1.3	Dosimetric accuracy	35
3.2	Evaluation of adaptive treatment planning approaches	39
3.2.1	Dosimetric evaluation	39
3.2.2	Treatment plan penalty scoring system	45
3.2.3	Anatomical metrics and correlation with dose.....	48
3.2.4	Treatment planning time	52
4	DISCUSSION	53
4.1	Evaluation of sCT	53
4.1.1	Image quality	54
4.1.2	Segmentation accuracy	55
4.1.3	Dosimetric accuracy	57
4.2	Evaluation of adaptive treatment planning approaches	60
4.2.1	Standard treatment plan evaluation methods	60
4.2.2	Additional treatment plan evaluation methods	64
4.2.3	Efficiency and clinical feasibility.....	67
5	SUMMARY	70
6	BIBLIOGRAPHY.....	72
7	APPENDIX	87
8	CURRICULUM VITAE	92
9	OWN PUBLICATIONS.....	93
10	ACKNOWLEDGEMENT	95

LIST OF ABBREVIATIONS

3D-CRT	3-Dimensional conformal radiation therapy
AAPM	American association of physicists in medicine
ADMIRE	Advanced medical image registration engine
ART	Adaptive radiation therapy
CBCT	Cone-beam computed tomography
CT	Computed tomography
CTV	Clinical target volume
DCNN	Deep convolutional neural network
DD	Dose difference
DDR	Dose difference pass rate
DICOM	Digital imaging and communications in medicine
DIR	Deformable image registration
DSC	Dice similarity coefficient
DL	Deep learning
d_{mean}	Mean surface distance
DTA	Distance-to-agreement
DVF	Deformation vector field
DVH	Dose-volume histogram
ED	Electron density
EPID	Electronic portal imaging device
ESTRO	European society for radiotherapy and oncology
FFF	Flattening-filter-free
FOV	Field-of-view
GAN	Generative adversarial network
GPR	Gamma pass rate
GPU	Graphics processing unit
GTV	Gross tumor volume
Gy	Gray
HD	Hausdorff distance
H&N	Head & neck
HU	Hounsfield Units
IGRT	Image-guided radiation therapy
IMRT	Intensity-modulated radiation therapy
IQR	inter-quartile range
ISO	Isocenter (Center of rotation for gantry, couch, collimator)
IVH	Intensity-volume-histogram
kV	Kilovoltage
Linac	Linear accelerator
MAE	Mean absolute error

ME	Mean error
MLC	Multi-leaf-collimator
MRI	Magnetic resonance imaging
MU	Monitor unit
MV	Megavoltage
OAR	Organs at risk
PACE	Prostate advances in comparative evidence
pCT	Planning computed tomography
PDD	Percentage dose difference
PTV	Planning target volume
QA	Quality assurance
RT	Radiation therapy
SAM	Segment aperture morphing
sCT	Synthetic cone-beam computed tomography
SD	Standard deviation
SEN	Sensitivity
SBRT	Stereotactic body radiation therapy
SPEC	Specificity
SV	Seminal vesicles
TPS	Treatment planning system
UHF	Ultra-hypofractionated
VMAT	Volumetric modulated arc therapy
VOI	Volume of interest
WSO	Warm start optimization
XVI	X-ray volume imaging (kilovoltage imaging system from Elekta AB)

1 INTRODUCTION

Cancer is the second leading cause of death with 239 591 deaths in 2019 in Germany¹ and 9.96 million estimated deaths worldwide in 2020². In particular, prostate cancer is the most diagnosed cancer type besides breast and colorectal cancer in Germany with an incidence of 607 373 in 2020 and has the second largest mortality among men with 15 500 deaths last year. On a global scale, 375 304 deaths in 2020 were caused by prostate cancer³.

Regarding the treatment of cancer diseases, radiation therapy (RT) gained more and more relevance amongst chemotherapy and surgical procedures during the last decades. Around 50-60% of all cancer patients are treated with radiation therapy⁴ which aims to destroy malignant tumor tissue while preserving the surrounding healthy tissue at the same time. Usually, the necessary treatment dose is applied in multiple fractions over the course of several weeks in order to minimize negative side effects^{5,6}. Current radiation therapy standards are on the cusp of being transformed by the clinical introduction of new treatment methods of adaptive radiation therapy (ART) and deep learning (DL)⁷⁻⁹, also with regard to the recently introduced magnetic resonance imaging(MRI)-based linear accelerators (linac)¹⁰. Figure 1.1 illustrates the clinical workflow steps of conventional intensity modulated radiation therapy (IMRT) and their progress throughout the development of treatment techniques, as further described in the following.

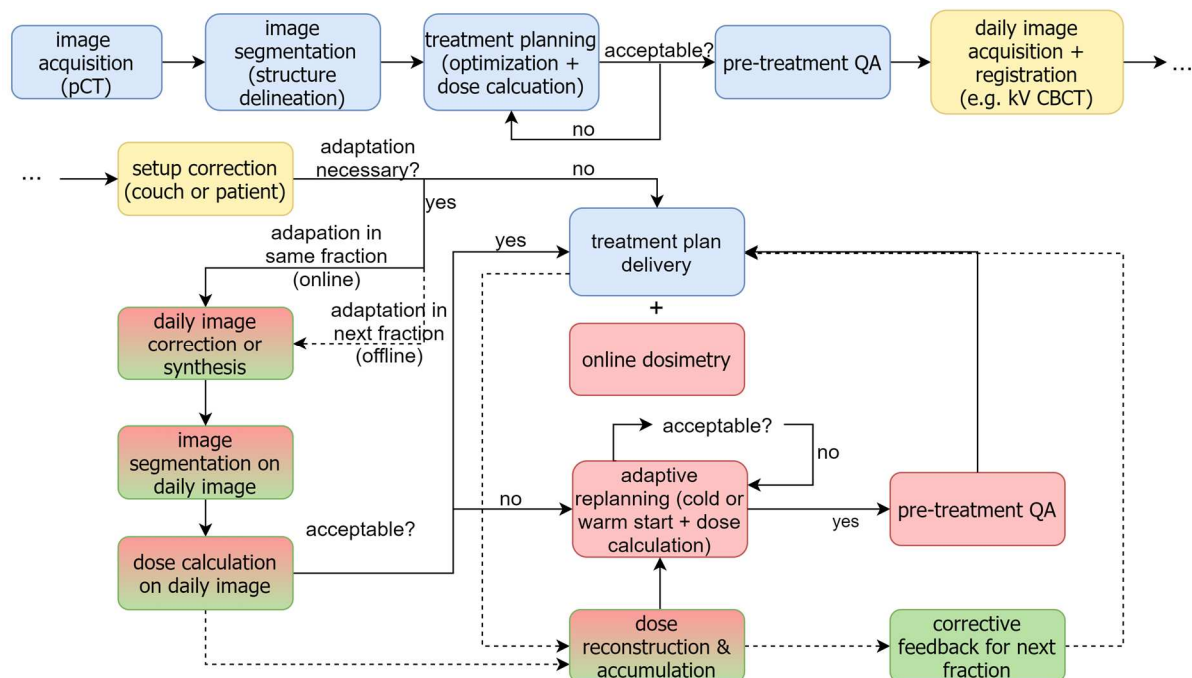


Figure 1.1: Steps of IMRT (blue), image-guided RT (IGRT) (yellow), offline ART (green) and online ART (red) treatment workflows, partly adapted from ^{25,8}. Daily image correction, segmentation and dose calculation can either be performed with the patient remaining on the treatment couch (online) or for the next fraction (offline). Dashed lines indicate potential offline steps for subsequent treatment fraction. (Abbreviations: pCT: planning CT, CBCT: cone-beam CT, QA: quality assurance)

First, in order to get an image of the patient's anatomy, a computed tomography for treatment planning purposes, the planning CT (pCT), is being acquired while the patient is immobilized on the treatment couch. This technique aims to achieve sufficient image quality that allows for a precise piecewise linear assignment of relative-to-water electron densities (ED) to image grey values in Hounsfield Units based on linear attenuation coefficients (HU-ED-calibration)⁶. Therefore it is fundamental to an accurate dose calculation during the subsequent treatment planning workflow.

In a second step of image segmentation (also referred to as contouring or structure delineation), the physician defines the volumes that contain all macroscopic cancer tissue (GTV: Gross tumor volume), sub-clinical disease spread (CTV: Clinical target volume) and treatment uncertainties (PTV: Planning target volume)^{11,12}. Adjacent healthy organs, referred to as organs at risk (OAR), are defined during the contouring procedure as well. Depending on the tumor site, the total prescription dose in Gray (Gy) including its delivery in single fraction doses is determined. An optimum balance between maximum tumor damage and simultaneous maximum sparing of the OAR based on international guidelines for normal tissue tolerance¹³ constitutes the major goal of every dose prescription concept as well as of RT treatments in general. The third substantial step in radiation therapy comprises treatment plan generation. Within a dedicated software (TPS: treatment planning system), the previously generated image and structure information is used to create a treatment plan that contains a sequence of machine-specific parameters for the actual treatment delivery at the linear accelerator. The treatment plan sequence mainly consists of parameters that relate the gantry angle, collimator angle, beam isocenter (ISO), monitor units (MU), nominal acceleration potential of the photon beam and positions of the multi-leaf-collimator (MLC) including its aperture jaws.

Since the beginning of first RT treatments in the 1970s, treatment sequences were entirely delivered by rectangular fields with a fixed fluence from different beam angles which added up to the desired prescription dose at the center of the PTV (3D RT). With the advent of enhanced computing power and the development of new technologies at the linac such as the MLC, the improved three-dimensional conformal RT (3D-CRT) was further refined by a modulation of single beam intensities within the concept of IMRT, replacing the forward planning procedure with inverse optimization algorithms^{6,14}. It became feasible to modulate the dose fluence with an increased number of degrees of freedom and achieve highly conformal dose distributions for complex target shapes with steep dose gradients towards the OAR. Several techniques are available today to perform fluence modulation: Step-and-shoot IMRT delivers the dose in discrete beam angles with stationary leaves per beam segment, sliding window techniques allow for a dynamic MLC movement during every segment and volumetric modulated arc therapy (VMAT) enables an additional gantry rotation simultaneous to the dynamic leaf motion^{15,16} while the dose is being delivered. Once a clinically acceptable treatment plan has been generated in the TPS, pre-treatment

quality assurance (QA) is being performed in a final step prior to the actual delivery to detect potential errors at the linac and compare the measured dose distribution to the reference^{17,18}. In conventional IMRT workflows, subsequent treatment plan QA is not necessary as the same treatment plan is being applied for every fraction over the entire treatment course.

The introduction of image-guided RT (IGRT) during the 2000s decade posed another major improvement for the clinical workflow of radiation therapy. Kilovoltage (kV) imaging represents the most common technique being used in clinical routine for target localization prior to the daily treatment plan delivery. An additional kV X-ray source attached to the linac gantry enabled daily 3D imaging of the patient anatomy and enhanced the patient positioning based on isocenter matching by a rigid 3D registration of the pCT to the daily acquired cone-beam CT (CBCT)^{19,20}. Thus, treatment accuracy was improved for every single fraction and due to daily monitoring PTV margins could be reduced. IGRT also paved the way for the introduction of new treatment modalities such as high precision stereotactic body RT (SBRT) which involves the application of high-dose radiation to a comparably small PTV delivered in a few treatment fractions^{21,22}. The pelvic region constituted a pilot site for the introduction of various new treatment techniques and research studies including ART approaches on account of its large proportion within all tumor sites and the comparably stable geometry of the prostate gland or CTV, respectively, throughout the entire treatment course^{8,23-25}. Starting from simpler delivery modes like 3D-CRT, the treatments for prostate cancer have been evolving over more elaborate IMRT techniques towards the current and complex VMAT deliveries with high fluence modulation, dose escalation strategies and small CTV-to-PTV margins of a few mm, not least because of modified radiobiological models²⁶. Along with head&neck (H&N) and lung cancer, most IGRT-induced modifications have been identified for the pelvic region²⁷, indicating a need for further refinements of conventional clinical methods, especially concerning the potential of adaptive treatment techniques in respect of improved individual treatment quality and automation⁸.

However, an increasing complexity of treatment techniques also demands for a more precise treatment monitoring on a daily basis and more elaborate QA. Current standards of an IGRT treatment mostly neglect morphological changes during the fractionated treatment course that go beyond translational or rotational couch shifts. Daily acquired CBCT are today rarely being used to adapt the initial treatment plan sequence to the daily organ variations although tumor sites in the H&N, thoracic, pelvic or abdominal region could additionally benefit from compensating uncertainties in the form of weight loss, tumor shrinkage or organ deformations²⁸⁻³⁰. These issues could be addressed with techniques of adaptive radiation therapy (ART) that target all four essential fields of the clinical workflow: imaging, contouring, treatment planning and QA^{8,31}. First concepts of ART have already been proposed by Yan et al. in 1997³² but could only be realized on the basis of clinically established 3D imaging within IGRT. The adjustment of the dose distribution based on the daily anatomy of the patient

represents the major goal of ART. This involves potential adaptation of the structure set and the treatment plan triggered by either anatomical deformation between two fractions (interfractional changes) or during the delivery of one treatment fraction (intrafractional changes). Various “offline” ART techniques like repeated pCT acquisition for H&N cancer due to weight loss, IGRT-induced replanning for subsequent fractions or patient-specific prediction of organ deformation of abdominal treatment sites^{8,33} are already being applied. However, the widespread use of adaptation procedures faces several difficulties such as an increased workload, numerous software interfaces and a lack of guidelines or thresholds. These issues are of particular importance with regard to the “online” ART concepts that target the modification during every single treatment fraction prior to the plan delivery^{25,34}.

Inferior image quality of CBCT and resulting imprecise HU-ED-calibration poses the major challenge towards the clinical implementation of ART techniques since a sufficient visualization of the patient’s anatomy with reliable density assignments is indispensable for accurate structure delineation and dose calculation. kV CBCT at conventional C-arm linacs are subject to image artifacts due to image lag, beam hardening, detector scatter and patient-specific scatter^{35,36}. Currently, several CBCT calibration approaches exist that allow for dose calculations on daily acquired images³⁷: Electron bulk density override techniques compensate the lack of patient-specific HU-ED-calibration³⁸ and post-processing algorithms further improve image properties like contrast or a cropped field-of-view (FOV)^{35,39,40}. Moreover, a deformable image registration (DIR)⁴¹ between the CBCT and the pCT can be used to generate a deformed CT or to deform daily delivered doses onto one reference image in order to assess anatomical and dosimetric changes⁴²⁻⁴⁴. All of these techniques demonstrated to be feasible for multiple tumor sites but still showed dosimetric inaccuracies of several percent, only worked reliably for single body regions or a small test collective, required specific data preparation or treatment protocols and potentially distorted the anatomy (in case of DIR involvement)³⁷, thus preventing an imminent use in daily routine.

Recently, the use of deep learning (DL) algorithms and associated neural networks gained popularity with respect to accelerate and automate time-consuming workflow steps in ART, especially since they can be custom tailored to individual workflow procedures^{9,45-49}. The potential of utilizing DL methods becomes particularly apparent with regard to image processing^{50,51}. Artificial neural networks can be trained with multimodal image datasets (e.g. CT and CBCT or CT and magnetic resonance images (MRI)) in order to generate synthetic CT images (sCT) which possess image properties close to reference images like CT and furthermore preserve the daily patient’s anatomy. Several recent studies demonstrated a significant reduction of image uncertainties in combination with accurate dose calculations on daily images of different tumor sites, hence increasing the potential for a clinical implementation of ART methods⁵¹⁻⁵⁴. Applications based on DIR and DL algorithms also gained relevance in image segmentation^{42,55,56}. The contouring or editing of a patient’s relevant organs, especially the OAR, is usually not completed within a few minutes and

therefore can be regarded as a time-consuming step during ART procedures alongside elaborate treatment planning. Initial approaches of automated segmentation evolved parallel with the accessible computing power from intensity threshold and edge detection algorithms over voxel classification and uncertainty models to algorithms using prior knowledge⁵⁵. Prior knowledge can either contain a single anatomical atlas (e.g. a contoured reference image) or multi-atlas approaches that are being used to transfer contoured structures onto an object image (e.g. CBCT). Most commonly, a DIR between the reference image and object image is used to generate the respective structures on the object image. This procedure is highly dependent on image quality, the organs' similarity and the deployed DIR algorithm^{43,55,57}. In the past few years, DL-based auto segmentation has been increasingly used in the form of fully-convolutional networks since they can adapt to a department's individual setup of image modalities and contouring procedures^{47,58}. It has been shown that a neural network trained with only 12 patients already produced robust results⁵⁹, although the segmentation output varies due to the prior-knowledge input characteristics and the training of the DL model. Still, fully-convolutional networks were able to prevail over multi-atlas approaches in recent segmentation challenges due to their velocity and soft-tissue delineation quality⁶⁰.

Constantly modified structures on a basis of daily acquired images demand for an adaptation of the treatment plan for every treatment fraction. Within IGRT, a full re-optimization of the initial treatment plan typically takes too much time while the patient is being positioned on the treatment couch. Taking advantage of a library with previously generated treatment plans^{61,62} might solve this issue but this approach still lacks an accurate estimate of possible organ deformations. Alternatively, the initial treatment sequence can be altered by a fast fluence modification technique based on morphological fiducial points⁶³ or by the application of segment aperture morphing (SAM) which can be followed by an adaptation of the weights, i.e. monitor units (MU), and shapes of the original plan segments⁶⁴⁻⁶⁶. These adaptation techniques are categorized as warm start approaches since their re-optimization procedure involves a-priori information of the reference treatment plan such as MLC apertures, single leaf positions, segment weights, beam angles or fluence maps of single control points, thus tremendously reducing the required calculation time. A further development of warm start approaches can be found in knowledge-based treatment planning, protocol-based iterative optimization⁶⁷ or the combination of DL algorithms which can be trained, for instance, to predict optimal beam and machine parameters or clinically acceptable dose-volume histograms (DVH) based on the given anatomical deformation or plan parameters^{68,69}.

Lastly, methods of QA play an important role within the framework of ART. Elaborate and daily performed modifications of the initial structure set and treatment plan stress the need for a more extensive and efficient QA on a daily basis⁷⁰. For this purpose, various approaches for the critical review of every core step in ART workflows exist: Guidelines for image registration and segmentation accuracy⁴¹, plan integrity control⁷¹, phantom-based measurements⁷²⁻⁷⁴, secondary dose engines for validation of the dose

distribution of the reference TPS⁷⁵, online dose monitoring systems⁷⁶⁻⁷⁸ or MLC together with machine logfile analysis tools^{79,80} to assess the daily delivered dose. In addition to the daily monitoring of adapted treatment sequences, the accumulation of the delivered dose constitutes another substantial goal of adaptive QA. In order to evaluate the total treatment dose, fraction doses on daily CBCT can be reconstructed and thus enable online modifications in case dosimetric adjustments are needed⁸¹⁻⁸³. On the whole, it emerges that various approaches of ART are available; some of them being ready for automation with the help of DL and hence could be implemented in the clinical workflow. However, multiple software interfaces, tremendous additional workload, missing standard guidelines and the quantification of actual benefits within an ART workflow still prevent the latest innovations from being clinically introduced on a larger scale³³. Besides, also due to the Covid-19 pandemic^{84,85}, treatment techniques like SBRT in combination with hypofractionation have experienced an increased interest, making the application of ART techniques even more inevitable⁸⁴.

When the same treatment plan is being applied over the course of several weeks during a conventional RT, the treatment quality and dosimetric accuracy are potentially compromised, especially in case of non-systematic or random anatomic variations as experienced for prostate cancer patients^{86,87}. Residual motion of the prostate or the seminal vesicles (SV) constitutes a relevant issue during the delivery of a treatment plan (referred to as interfractional). However, dosimetric deviations predominantly arise from interfractional changes like fluctuating organ fillings or relative distances between the CTV and the bladder or rectum^{88,89}. These daily variations might have a chance to cancel each other out within the entire normo-fractionated treatment course of, for example, 30 single fractions but the daily modification of treatment plans becomes indispensable if the fraction number is reduced to 5 in case of ultra-hypofractionated (UHF) treatment regimens.

Specific fractionation approaches are connected to the biological principle of radiosensitivity and its application to healthy or malignant tissue which is being reflected by the α/β -ratio in the linear-quadratic model (LQM)⁹⁰. The herein implemented characteristics of the cell damage and surviving fractions enable a therapeutic window for the delivery of RT doses since the treatment dose can be split up into many small exposures (fractionation) with simultaneously allowing for healthy tissue regeneration⁹⁰. Although the LQM constitutes a reliable approximation of standard fraction doses between 1 and 5 Gy, it exhibits deficiencies when it comes to the effects of high fraction doses >5 Gy, pauses of irradiations, extreme hyperfractionation or accelerations of treatment regimens⁹¹. Moreover, the α/β -ratio is relevant for clinical applications as it defines the dose for which both linear and quadratic terms of the LQM possess the same proportion of cell destruction. Both healthy and tumor tissues exhibiting early response to irradiation usually have α/β -ratios of 6-20 Gy and less sensitive tissues have α/β -ratios of 0.1-5 Gy⁹¹.

The prostate carcinoma is categorized as late-response tissue and has an α/β -ratio of around 1.2-1.5 Gy⁹¹. Thus, and in order to further increase the time-related therapeutic window between tumor cells and late-responding healthy tissue, initial RT treatments

of prostate cancer aimed for a hyperfractionated regimen, delivering small single doses in a comparable high number of fractions⁹². However, due to the technical innovations towards highly modulated as well as more accurate dose deliveries and increasing follow-up studies about RT toxicity in the last decades, hypofractionated RT (HF RT) has been used increasingly, leading to an improved tumor control with almost unaltered toxicity⁹³ also in case of prostate cancer^{94,95}. Furthermore, an increasing number of surveys revealed large inhomogeneities within outcomes of α/β -ratios, making them a subject of constant correction⁹⁶, also with regard to an adjusted value for prostate tumors of approximately 1^{96,97}. This ongoing uncertainty of the LQM is connected to new findings regarding interaction of radiation therapy with the immune system and the cellular connection between tumor cells and surrounding tissue⁹⁸. Besides, different categories of risk staging influence the debate about the most suitable fractionation approach. While consisting of adenocarcinomas up to a proportion of 95%, the malignancy of a prostate carcinoma is typically connected to the identified Gleason score which is composed of the two most dominant patterns of growth and represents the summed grading of the tumor with scores of 2-4 (well differentiated), 5-6 (moderately differentiated) and 7-10 (poorly differentiated)⁹¹.

Altogether, technical progress, adjusted dose-effect models and latest findings of RT toxicity research paved the way towards increased fraction doses for prostate cancer treatment along with a variety of clinical trials^{85,99,100}. The CHHip trial constitutes one of the major surveys with more than 3000 patients included, evaluating the side effects and long-term toxicity of moderate hypofractionation. It demonstrated a non-inferiority of 60Gy in 20 fractions compared to 74Gy in 37Gy fractions, also concerning patient-reported bowel symptoms^{101,102}. Another large-scale study, the HYPRO trial, investigated over 800 patients and could also prove the competitiveness of delivering 3-4 Gy in 19 fractions against CF RT with a slightly higher toxicity of the hypofractionated arm¹⁰³. More and more phase 3 clinical trials concerning HF RT were completed during the last couple of years and even UHF RT trials started to enter phase 3¹⁰⁴. The largest phase 3 UHF RT trial is the HYPO-RT trial, with more than 1200 patients acquired in 12 centers of Sweden and Denmark. Obtained results showed that 42Gy delivered in 7 fractions lead to more early side-effects but late toxicity was almost similar to CF RT¹⁰⁵. Another ongoing phase 3 clinical trial is the PACE trial. Also carried out on an international platform with more than 2000 patients, the published results confirmed the non-inferiority of delivering 36.25 Gy in 5 fractions at both Cyberknife and C-arm linacs compared to the CF RT and surgical prostatectomy. In contrast to the HYPO-RT trial, slightly larger acute toxicity indications were inclined towards the CF RT arm¹⁰⁶.

Whereas HF RT is already recommended for example by the National Comprehensive Cancer Network or ASTRO guidelines as a reliable alternative to CF RT for all clinically indicated prostate cancer patients, UHF RT merely remains non-inferior for favorable-good intermediate risk disease and the treatment of high risk patients is still lacking substantial prospective evidence^{107,108}. Still, UHF RT can significantly shorten the

overall treatment time, increase the quality of life for patients or reduce hospital costs which consequently justifies the growing relevance of UHF prospective trials.

On account of these developments in the field of DL applications for RT as well as latest prostate cancer treatment and fractionation approaches, the goal of this research study was to evaluate the advantages of a novel synthetic CBCT-based adaptive workflow within the framework of a UHF prostate cancer treatment regimen over the conventional IGRT approach. Aiming for an implementation of the proposed ART workflow in clinical routine, the specific objectives of this work were twofold:

First and in order to overcome the major challenge of imprecise ED assignment in daily kV CBCT, the accuracy of a novel DL-based CBCT-to-sCT generation approach with regard to a potential unsupervised usage in a complete ART workflow was analyzed. A cycle-generative adversarial network (cycle-GAN) algorithm was previously trained with clinical 3D-image datasets (pCT and daily CBCT) in order to create a sCT model for the pelvic body region. So far, a large amount of published research on sCT-based ART either mainly focused on imaging properties^{53,109-111} or contained basic results about dosimetric uncertainties¹¹²⁻¹¹⁴. Therefore, the performance of this pelvic sCT model on a separate test dataset of pelvic CBCT concerning its accuracy was subsequently analyzed for all essential and successive workflow components of image quality, image segmentation and dose calculation, all being available within one clinically established software. The aim of this thesis was to answer the following specific questions for the novel cycle-GAN-based sCT generation method:

- (1) Is the image quality of a sCT similar to that of a pCT?
- (2) Is the automated image segmentation on the sCT of comparable quality to manually generated contours or can contours at least be modified while the patient remains on the couch during the treatment fraction?
- (3) Is the dosimetric accuracy of a sCT comparable to a pCT?

Furthermore, the methods' feasibility including competitiveness to alternative, current end-to-end ART procedures and potential further refinements are being discussed.

Second and targeting the subsequent issue to image and segmentation modifications in a daily ART workflow (see Figure 1.1), the proposed sCT-based ART workflow was complemented with techniques of adaptive treatment planning that were evaluated in respect of dosimetric benefits over the current standard of IGRT. For this purpose, several replanning approaches ranging from dose recalculations within IGRT over segment aperture morphing (SAM)-based warm-start optimization to a full re-optimization were compared to each other. Based upon a larger patient cohort of prostate cancer patients and within an exemplary UHF SBRT treatment regimen (PACE-C trial), standard plan analysis methods plus additional scoring systems were employed to categorize the benefit of ART replanning methods over IGRT on a broader scale. Furthermore, practical efficacy and correlations with anatomical parameters were also assessed for guiding the decision of when to apply which adaptation strategy. Regarding a transition of the analyzed adaptive workflow from an offline to an online type, its capacity for automation, application to other body sites than pelvis and potential improvements are presented.

2 MATERIALS AND METHODS

In order to pave the way for a clinical introduction of ART techniques within prostate SBRT, the central issue of insufficient CBCT image quality was solved by applying a cycle-generative adversarial network (GAN) for the generation of synthetic CBCT (sCT). Three core procedures were implemented within this research study as depicted in Figure 2.1:

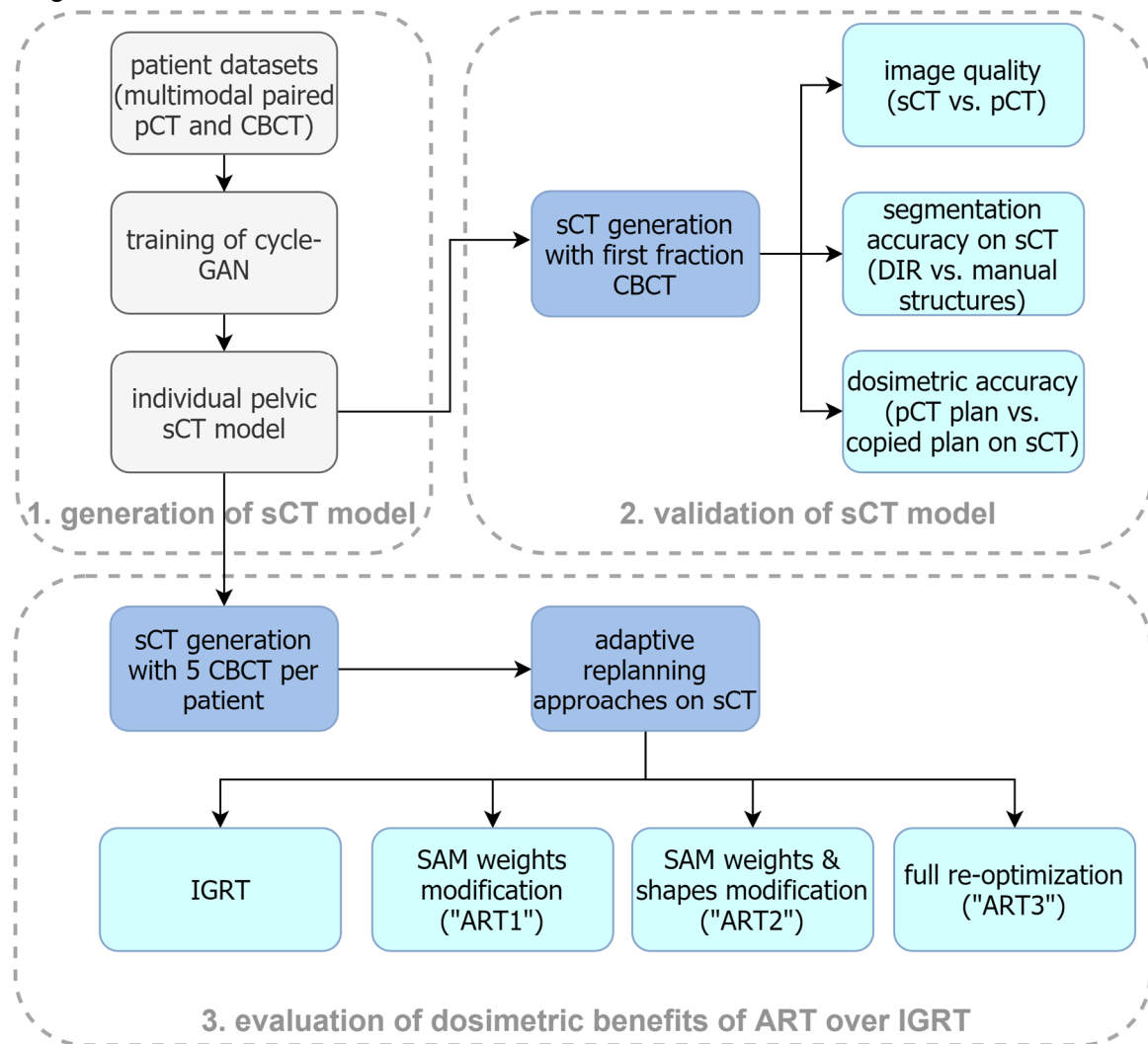


Figure 2.1: Relevant components of realizing an end-to-end ART workflow based on synthetic CBCT. The three core procedures involved the generation of the cycle-GAN-based pelvis sCT model, its validation for every crucial treatment component and the evaluation of dosimetric benefits of sCT-based adaptive replanning over IGRT.

In a prior step, multimodal paired image data were collected from prostate cancer patients for training a cycle-GAN for the pelvic body region in order to create a body site specific sCT model. After giving a short general overview of image processing with artificial neural networks, the first part of this chapter is therefore concerned with the architecture of the applied cycle-GAN being provided within the TPS software.

The second part contains the general validation and analysis of the generated individual pelvic sCT model. By applying the sCT model to first fraction CBCT of 15

prostate cancer patients, relevant treatment components of imaging, segmentation and dose calculation on sCT were being analyzed, also with a focus on clinical applicability. The third section addresses methods of adaptive replanning approaches within the scope of the UHF PACE-C trial treatment regimen of the prostate (40Gy in 5 fractions). Methods of warm start optimization based on segment aperture morphing (SAM) are explained, followed by the study design of retrospectively comparing four different treatment planning approaches on sCT: Conventional IGRT, SAM with weight optimization (ART1), SAM with weight and shape optimization (ART2) and a full re-optimization (ART3). The objective of quantifying the dosimetric benefits of ART techniques over today’s conventional IGRT approach was implemented by comparing standard dose-volume metrics and characterizing treatment plan quality with a penalty score as well as anatomical parameters.

2.1 Generation of a pelvic synthetic CT model

2.1.1 Patient population

Regarding the general architecture of neural networks, it is relevant to distinguish between the dataset being employed for the training process and the test dataset which is used to evaluate the performance of the neural network. The two datasets can share characteristics but in case of sufficiently large data collectives it is desirable to avoid any overlap between them, i.e. respective patient populations have to be separated from each other. Table 2.1 contains the patient and treatment characteristics of the training and test population for the cycle-GAN based pelvic sCT model.

Table 2.1: Patient and treatment characteristics of the training and evaluation dataset for the cycle-GAN-based sCT model for the pelvic body region. All included datasets belonged to prostate cancer patients.

Patients for training / evaluation	Diagnosis	Tumor stage	Gleason score (of evaluation dataset)	Energy (MV) and treatment modality	Prescription dose (Gy), fraction dose (Gy)	Average patient age and range for training / evaluation
205 / 15	Malignant neoplasm of prostate (c61) (including seminal vesicles)	T1c- T2c	6: 5 patients 7: 7 patients 8: 2 patients 9: 1 patients	10 MV (with flattening filter), VMAT delivery	60, 2 or 3	71.6 (50-82) / 73.6 (57-84)

All patients included in this sCT research were retrospectively analyzed after IRB approval (2018-836R-MA). In total, paired CBCT and planning CT (pCT) volumes of 205 different prostate patients were used for the training of the pelvic sCT model with

each patient having one pCT and a maximum of three associated CBCT. The training datasets were collected at seven different clinical centers including the University Medical Center Mannheim. The performance of the final sCT model was subsequently evaluated for 15 prostate cancer patients. All patients in the training and evaluation dataset had tumor stages from T1c-T2c and were treated with a prescription dose of 60Gy in 30 or 20 fractions. Patients in prone position or having a total endoprosthesis (TEP) were excluded from the study.

The pCT of every patient was obtained with a CT scanner (Brilliance Big Bore, Philips Healthcare, Amsterdam, Netherlands) using the pelvic site-specific scan protocol with a slice thickness of 3 mm shown in Table 2.2.

Table 2.2: Image acquisition parameters of the pCT (Brilliance Big Bore, Philips) and kV-CBCT (XVI 5.0, Elekta).

Modality	Field-of-view (cm*cm)	Matrix	Slice thickness (mm)	Voltage (kV)	Current*time (mAs)	Acquisition time (s)	Filter, Collimator	Acquisition interval (°)
pCT	-	512	3	120	145	13	Standard (B)	-
CBCT	27.6 * 42.6	512	3	120	132	120	F1 (bow-tie), M20	-180 to 180

Prior to each treatment fraction, the daily kV CBCT were acquired with the linac-attached kV source and volumetric imaging system (XVI 5.0, Elekta AB). The applied “M-preset” for pelvic tumor sites used the F1 bow-tie filter with a M20 collimator for a full 360°arc acquisition interval and thus had a FOV of 27.6cm*42.6cm in the ISO of the imaging area. After reconstruction, the CBCT were rigidly registered to the pCT and exported for training/evaluation with a slice thickness of 3 mm.

2.1.2 Architecture of the cycle-generative adversarial network

The importance of DL in the form of artificial neural networks has undeniably increased over the last few years⁴⁸. Regarding the field of image processing, neural networks have been widely and successfully employed to achieve denoising, improve reconstruction and create new images, also cross-modality wise. Besides the types of convolutional or encoder-decoder networks, generative adversarial networks (GAN) have demonstrated their promising performance in terms of denoising and image synthesis even for unpaired datasets¹¹⁵⁻¹¹⁷. The fundamental functionality of a GAN is depicted in a simplified diagram in Figure 2.2. The noise and artifacts of an image belonging to the domain A constitute the input for the first involved network called “generator” that has the task to create new images (B’) which are close or ideally indistinguishable to the image quality of reference images in domain B.

This is handled by employing a second network. The “discriminator” compares the generated to the real reference images and thus is able to provide a feedback input for the generator in order to improve its performance. This comparison is represented by the network’s loss term which manages the two tasks of evaluating the similarity of B and B* as well as deciding if B* is real or fake. In general, the balance between the two competing networks of the generator and discriminator and their mutual dynamics constitutes the largest difficulty during the training process. However, once this challenge is overcome, GANs were demonstrated to be capable of providing superior outcomes in terms of efficient performance, enhanced image quality and content preservation for several body sites^{46,51,117}. Further enhancements can be realized by the use of cycle-GANs which combine two GANs in both forward and backward direction in order to better minimize differences between synthetic and real images by additional help of cycle-consistency loss⁵¹ (see panel (b) of Figure 2.2).

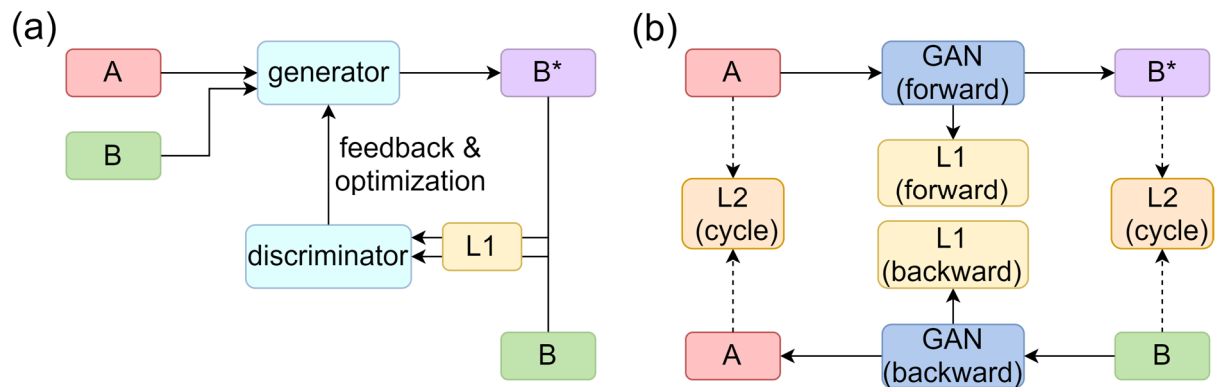


Figure 2.2: Principle functionality of a generative adversarial network (GAN) (a) and a cycle-GAN (b) (adapted from ^{117,51}).

Alternatively, deep convolutional neural networks (DCNN) or U-nets can also be employed for purposes of image translations or artifact corrections^{110,118}. They are characterized by reducing the input data’s processing with multiple convolutional and pooling layers aiming for a systematic and specifically weighted subsampling. U-nets represent a subtype of the DCNN that are further refined with a contracting and an expanding branch, also including the ability to skip specific layer connection in order to enable a modelling of high-resolution multi-scale tasks⁴⁵.

The research software ADMIRE (Advanced Medical Image Registration Engine) (Elekta AB), embedded in the commercially available treatment planning system (TPS) Monaco (Elekta AB), offers an approach to generate sCT based on CBCT with the help of a 2D cycle-GAN. Here, the term 2D refers to the networks’ separated processing of every two-dimensional slice of an entire 3D image (CBCT or pCT). The utilized cycle-GAN was based on generators, discriminators and network structures similar to the work from Xu et al.¹¹⁹ and Zhu et al.¹¹⁶ and further optimized by Elekta towards a CBCT application based on the clinical data provided by our research group. Two issues needed to be resolved in order to apply such a network for medical image synthesis. Geometry or structure distortion and insufficient pixel-level accuracy due to the mere distribution match in two domains were additionally modified by Elekta and are

implemented in the ADMIRE sCT module¹²⁰. Paired CBCT and pCT, obtained by applying a DIR in ADMIRE on the native pCT, form the basis for the training strategy of the sCT module, in contrast to unpaired training mechanisms presented in several other research studies^{111,121,122}. Moreover, an L1 term was employed in addition to the original adversarial loss and the cycle loss terms. The L1 penalty term between the sCT and the respective paired images for specific regions was used for both “forward” and “backward” direction. Lastly, in order to avoid potential distortion of image structures, transform layers were added into the original network architecture. Both training and deployment modules were implemented with the help of a TensorFlow library using Python as well as C++ interfaces.

All paired CBCT and CT for the pelvis model were clipped into the value range from -1000 to 1000 HU, thus achieving an improved representation of high density structures like bones. Within all training procedures, a linear scaling of [-1.0 1.0] was applied to all images as input and predicted output. Furthermore, a resampling to a size of 224x224 pixels was performed for standardization and reduction of training time. The training procedure itself involved an Adam solver with the initial learning rate of 0.0002 and a total of 200 epochs, whereas a fixed learning rate was used for the first 100 epochs and a linear decay for the following epochs. Originally, all hyperparameters were implemented by Elekta in a standalone module and were not changed afterwards for the purpose of evaluating the pelvic sCT model. The minimum HU threshold, being the only parameter that can be tweaked during the application of the final pelvic sCT model in ADMIRE, was found to perform best at a value of -800HU.

2.2 Validation of the pelvic sCT model

In order to include every essential step of an adaptive end-to-end workflow at a conventional C-arm linac the first main part of this research study aimed to validate the novel cycle-GAN-based sCT model for the three core treatment components of imaging, image segmentation and dose calculation. While this thesis targets ART advances by the example of the pelvic body region, the complete evaluation of the sCT model performance was originally carried out for two additional body regions (H&N and thorax) and is available in the literature¹²³.

2.2.1 Treatment workflow

The performance of the pelvic sCT model was based on the analysis of 15 CBCT of 15 prostate cancer patients, being entirely independent from the aforementioned training datasets. Only CBCT of the first treatment fraction were used to generate sCT with the intention to minimize potential anatomical differences between the pCT and the CBCT. At the beginning of every patient’s standard IGRT-based treatment workflow, a pCT was acquired and assigned with a scanner-specific ED-HU-calibration. A tissue-characterization phantom (model 467, Gammex, Middleton, WI, USA) was used for obtaining the standard deviation (SD) of the pCT’s image noise.

Subsequently, an expert physician delineated the following volumes of interest (VOI): prostate, seminal vesicles (SV), gross tumor volume (GTV), bladder, rectum and pelvic bones. Thereafter, treatment plan dose calculations based on the Monte Carlo algorithm were performed in the TPS (Monaco 5.11, Elekta AB) with a statistical uncertainty of 0.5% and a grid size of 2 mm. All prostate treatment plans had a prescription dose of 60Gy to the GTV and were delivered at a C-arm linac (VersaHD with Agility MLC, Elekta AB) with a nominal beam acceleration potential of 10 MV (with flattening filter) via a dual-360° arc VMAT. kV-CBCT were acquired daily at the linac prior to each treatment fraction with the linac-attached imaging system (XVI 5.0, Elekta), reconstructed and eventually rigidly registered to the pCT. On average, the time between the acquisition of the pCT and the CBCT at the first treatment fraction was (4.0 ± 2.3) days. The CBCT was then imported into Monaco and processed with the embedded pelvic sCT model via ADMIRE. The same HU-ED-calibration curve of the pCT was applied to the generated sCT. Relevant VOIs on the sCT were manually delineated by an expert physician and afterwards compared to automatically generated VOIs based on DIR, as explained later on. In order to evaluate dosimetric deviations between the pCT and the sCT, the reference treatment plan on the pCT was copied to the sCT and recalculated with identical settings. The detailed methods of analyzing image quality, segmentation accuracy and dosimetric accuracy are described in the following sections.

2.2.2 Image quality of sCT

Sufficient image quality is indispensable for precise daily imaging and for all subsequent treatment components in a potential adaptive workflow. Eliminating artifacts and noise enables an accurate HD-ED-calibration and thus precise dose calculations. Furthermore, manual structure delineation or automatic image segmentation can only yield robust results if underlying images are not impaired by a low soft tissue contrast or other image uncertainties. Essential characteristics of good image quality are quantified by parameters such as the mean error (ME), mean absolute error (MAE) or peak signal-to-noise ratio (PSNR)^{53,124}. The ME and MAE compare each voxel within a specific volume of interest (VOI) between a reference image (here: pCT) and an evaluation image (here: sCT):

$$\text{ME}(X, Y) = \frac{1}{N} \sum_{i=1}^N X_i - Y_i \quad (2.1)$$

$$\text{MAE}(X, Y) = \frac{1}{N} \sum_{i=1}^N |X_i - Y_i| \quad (2.2)$$

N denotes the number of voxels within the specific VOI, X_i the i -th grey value of the sCT and Y_i the i -th pixel value of the pCT in HU. In this research study, the ME and MAE were analyzed for three different VOIs for the pelvic body region in order to identify material-specific noise characteristics. An expert physician manually contoured

organ structures on both the pCT and the respective sCT. The patient outline formed the “body contour VOI”, the bladder, prostate and rectum the “soft tissue VOI” and the pelvic/femoral bones were used for the “bone VOI”. Furthermore, and solely for the image uncertainty analysis, the following negative margins were applied to the three VOIs with the intention to compensate potential anatomical differences between the pCT and the sCT: 15 mm margin to the body contour VOI, 10 mm to the soft tissue VOI and 4 mm to the bone VOI.

All relevant image datasets were imported in the software Velocity (version 3.2.1, Varian Medical Systems, Palo Alto, USA). After the CBCT and sCT had been rigidly registered to the pCT, pixel-wise subtraction images were created between the pCT-CBCT and pCT-sCT within the FOV of the CBCT to obtain the pixel-wise differences for the calculation of the ME, MAE and PSNR. Additionally, the mean of the obtained results for the ME were compared to 0 HU by means of a two-tailed t test in order to distinguish between a Gaussian noise distribution around 0 HU and actual image noise. A p-value of ≤ 0.05 indicated statistically significant differences. This part of the image analysis was not further expanded by means of other common metrics like the normalized cross correlation or the structural similarity since the CBCT and pCT were not acquired on the same day which led to slight anatomical discrepancies.

Apart from single metrics, all images were evaluated via intensity-volume-histograms (IVH) which display the distribution of the CT number-assigned image grey value in (HU) in relation to their respective volume proportion in cubic centimeters (cc). The CT number histograms of the reference (pCT) were compared to the CBCT and the sCT for the total body contour VOI (-15 mm margin) for all 15 prostate patients. The histograms were created in Velocity (version 3.2.1, Varian Medical Systems, USA) based on the rigid registration between the CBCT/sCT and the pCT and then further processed in the software Origin (version 9.7, OriginLab Corporation, USA), including a smoothing process of the discretely binned grey values.

2.2.3 Segmentation accuracy of sCT

As the output of the image generation process is always used as an input for consecutive treatment steps, the second part of the general validation of the pelvic sCT model consisted of the evaluation of image segmentation on sCT. It focused on the question of whether differences in image quality between the pCT and generated sCT could affect the segmentation accuracy. For this purpose, an expert physician manually delineated the GTV (prostate plus seminal vesicles) and OAR bladder and rectum on both pCT and sCT. Afterwards, a DIR within the intra-patient segmentation module of ADMIRE was performed between the pCT and sCT to transfer the manually created structures from the pCT onto the sCT (“contour propagation”). The deformed structures on the sCT were eventually corrected by the same expert physician and compared to each other by means of standard segmentation metrics, as shown in

Figure 2.3 and Equations (2.3)-(2.7). The required time for modifying the deformed structures was recorded as well. In general, the process of an image registration involves the determination of a spatial transform which maps the points from one image (“atlas image”) to the respective points of a second image (“subject image”). In contrast to a rigid registration where every image point between the two images is connected by the same linear transformation matrix, every fixed point of an image can, for example, be subject to its own unique transformation vector^{41,125}.

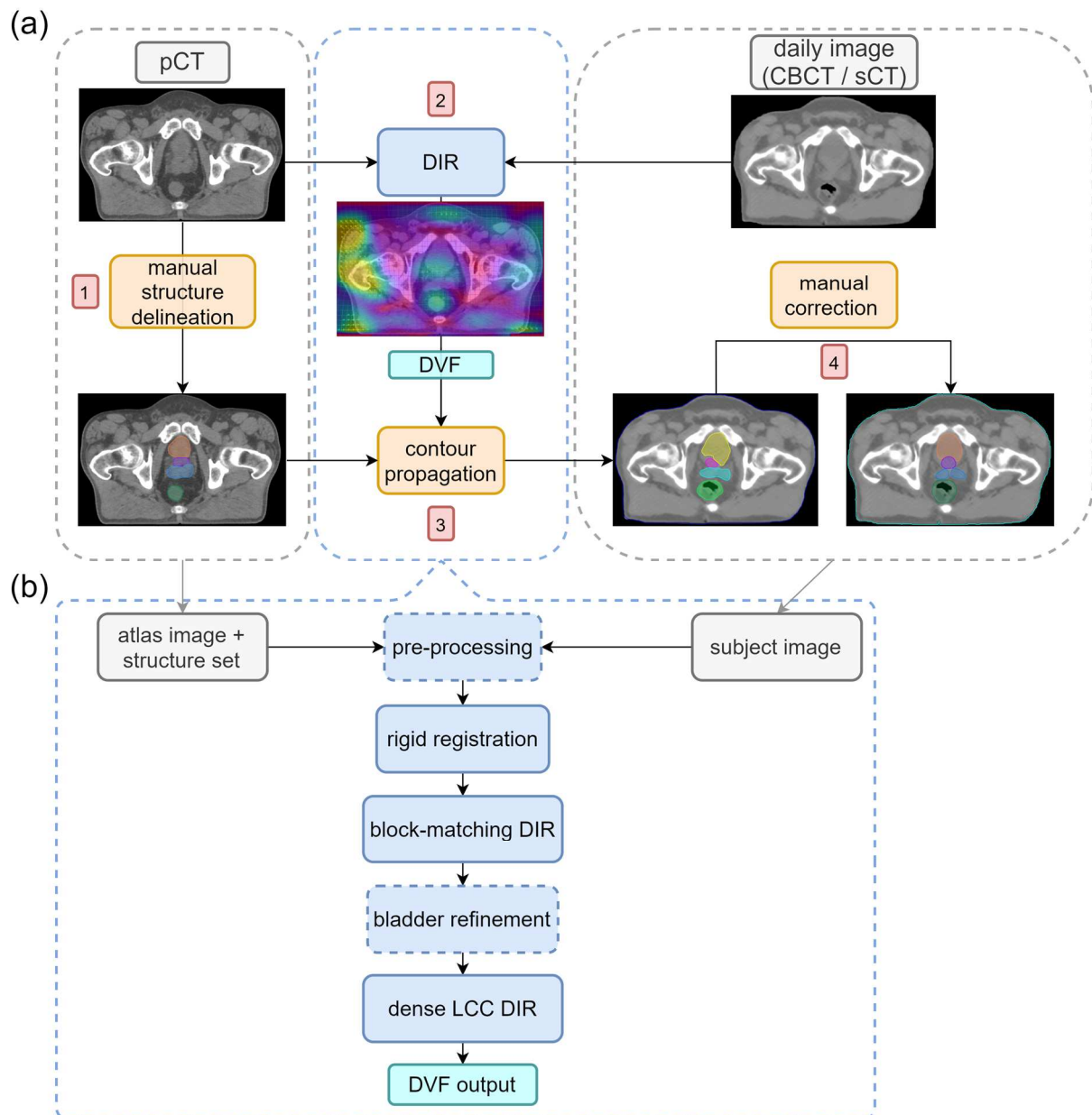


Figure 2.3: (a) Image segmentation workflow based on deformable image registration (DIR) and automated contour propagation including subsequent manual correction (adapted from ⁴²). (b): Workflow of the intra-subject deformable image registration tool of the ADMIRE GUI for contour propagation in Monaco research v5.19 (see ¹²⁶). Dashed boxes indicate pelvis-specific steps.

As a consequence, the entire spatial transform for the atlas image is defined by an array of displacement vectors called the deformation vector field (DVF). This DVF forms the basis for transferring the structures from an atlas image onto a subject image, i.e. the daily sCT, in the process of a contour propagation (see Figure 2.3, panel (a), adapted from ⁴²). The results of the contour propagation are prone to uncertainties that arise mainly from insufficient image contrast and too large anatomical variations between the two involved image datasets. Thus, a manual correction of the automatically created DIR-based structures is still inevitable in most cases. Furthermore, and due to the great variety of applied registration methods, detailed QA in form of, for example, end-to-end tests with phantoms or an independent report system with error tolerances is highly recommended by the AAPM task group 132⁴¹. The employed DIR algorithm of the ADMIRE software in this research study is based on three registration steps which gradually increase the freedom for image matching as illustrated in Figure 2.3, panel (b) (adapted from ¹²⁶). First, a pre-processing is performed in order to manage the adverse effect of rectal gas on pelvis image registration. Afterwards, the software ADMIRE performs a linear registration to compensate for larger offsets between the atlas and subject images based on maximizing the global mutual information with a multi-resolution stochastic gradient-descent optimization scheme. The first non-linear step consists of a block-matching method using a normalized-sum-of-squared-differences in all three dimensions of the physical space that is defined by the DICOM images. Especially developed for pelvic images, the structure propagation of the bladder can be further refined by a deformable surface model in case larger shape changes occur.

This step is followed by the computation of a dense deformable registration based on a local-correlation-coefficient (LCC) metric to additionally improve the previous block-matching and to align image details. All these registration steps eventually generate a deformation vector field which is being applied to the organ structures on the reference pCT, resulting in propagated structures on the sCT. These DIR-based structures (D) on the sCT were compared to the manually delineated structures (M) on the sCT by means of the following five commonly used segmentation metrics^{57,127}:

$$DSC = \frac{2 |M \cap D|}{|M| + |D|} \quad (2.3)$$

$$d_{\text{mean}} = \frac{\overrightarrow{d_{\text{avg}}}(M,D) + \overrightarrow{d_{\text{avg}}}(D,M)}{2} \quad (2.4)$$

$$HD(M, D) = \max_{m \in \partial M, d \in \partial D} \{d(m, \partial D), d(d, \partial M)\} \quad (2.5)$$

$$SEN = \frac{|M \cap D|}{|M|} \quad (2.6)$$

$$SPEC = \frac{|\overline{M} \cap \overline{D}|}{|\overline{M}|} \quad (2.7)$$

The overlap of two volumes M (manually created) and D (deformed) is defined by the standard metric of the Dice similarity coefficient (DSC). Additional common parameters for expressing the 3D distance between two volumes are the mean surface distance (d_{mean}) and the Hausdorff distance (HD). d_{mean} compares a point of the reference volume M to its nearest respective neighbor in the object volume D by calculating the average of two directed mean surface distances d_{avg} . Functioning as an indicator for the maximum segmentation error, HD represents the largest distance of two adjacent structure points m and d being part of the corresponding subsets of surface voxels denoted as ∂M and ∂D ⁵⁷.

Moreover, the measures Sensitivity (SEN) and Specificity (SPEC) can quantify the amount of the artificially created volumes that is a false positive or false negative. The SEN calculates the proportion of correctly identified non-zero structures voxels inside manually contoured structures M. The SPEC quantifies the amount of overlapping voxels outside the manually contoured ground truth volume M, with \bar{M} and \bar{D} denoting the volumes outside the manually created and automatically deformed structures. These five segmentation metrics were calculated for the bladder, prostate, rectum and seminal vesicles.

2.2.4 Dosimetric accuracy of sCT

The third part of the sCT model validation involved the accuracy analysis of dose distributions on the sCT. The reference treatment plans on the pCT were recalculated with identical settings of beams and segments on the first fraction sCT with a grid size of 2 mm and a statistical uncertainty of 0.5% per dose calculation. No additional DIR between the pCT and sCT was performed. Consequently, potential dose deviations between the reference and recalculated dose distributions could not only originate from image uncertainties but also from anatomical differences.

The following standard DVH parameters were used for comparing the dose distributions on the pCT and sCT with regard to either target volumes or OAR: Near-minimum, median and near-maximum doses D_{98} , D_{50} and D_2 for the GTV as well as V_{40} , V_{50} and V_{60} for the bladder and rectum. D_i denotes the dose in (Gy) that is received by a certain amount i of the volume in (%) and V_j denotes the volume that receives a specific dose j in (Gy). Relative differences between the DVH parameters of both pCT and sCT were calculated in (%), taking the dose distribution on the pCT as reference. Results were defined as outliers in case they were outside the interquartile range (IQR) of 25-75% of all obtained values. In contrast to the image accuracy analysis, no negative margins were applied to the analyzed structures for any part of the dosimetric comparison. Furthermore, Pearson's correlation coefficients between the MAE of the body contour VOI as well as soft tissue VOI and the target as well as OAR dose-volume parameters were obtained in order to identify potential coherences between the image quality of the sCT and the respective dosimetric results.

In addition to that, the recalculated plans on the sCT were compared to their reference plan on the pCT by means of 3D global gamma pass rate and a 3D point-wise dose difference. Originally documented by Low et al.¹⁸ and still recommended by the AAPM TG No.218 as a gold standard¹⁷, the gamma index and gamma pass rate calculation was specifically developed for the verification of IMRT treatment plan sequences. Equations (2.8) and (2.11) describe the detailed calculation:

$$\text{gamma value} \quad \Gamma = \sqrt{\frac{r^2}{\Delta r_{\text{tol}}^2} + \frac{\delta^2}{\Delta \delta_{\text{tol}}^2}} \quad (2.8)$$

$$\text{DTA} \quad r = |\vec{r}_{\text{ref}} - \vec{r}_m| \quad (2.9)$$

$$\text{PDD} \quad \delta = D_{\text{ref}} - D_m \quad (2.10)$$

$$\text{gamma index} \quad \gamma = \min\{\Gamma\} \forall \{\vec{r}_m\} \quad (2.11)$$

The calculation involves a quantitative comparison between a reference and a test dose distribution which is based on two criteria. The distance-to-agreement (DTA) r expresses the minimum distance between two points having the same dose in the test and reference dose distribution whereas the percentage dose difference (PDD) represents the relative difference between the test dose D_m and reference dose D_{ref} .

Δr_{tol} denotes the spatial tolerance and $\Delta \delta_{\text{tol}}$ the dosimetric tolerance. \vec{r}_{ref} and \vec{r}_m are identified as the position vectors of the reference dose point and the test dose point, respectively. The definition of specific tolerance levels of the PDD in (%) and the DTA in (mm) yields multiple gamma values for every dose point from <1 (below tolerance) to >1 (above tolerance), with 1 being equal to the ellipsoid's surface that functions as a limiting criteria for the gamma calculation in 2D. The use of a gamma index γ based on the minimum gamma value condenses this evaluation complexity to a single value per dose point¹²⁸. Consequently, the agreement between the reference and test dose distribution is highest for very small gamma indexes and acceptable for gamma indexes being less or equal to 1. The gamma pass rate (GPR) eventually reflects the amount of dose points fulfilling the tolerance of the gamma value. Common GPR criteria are 3%/3mm and 2%/2mm for the purpose of verifying measured dose distributions or comparing two treatment plans with each other¹⁷.

Another relevant parameter for calculating GPR or PDD is the low dose threshold that represents the minimum dose value being included for the dosimetric analysis. While a very low threshold of e.g. 5% can lead to whitewashed results as low dose areas are rarely subject to high dose inaccuracies, especially when globally normalized to the maximum planned dose, very high thresholds of $>90\%$ can cause undesirable low gamma pass rates due to dosimetric peaks in high dose regions unless those are of specific interest. On account of the aforementioned conditions and most popular

metrics applied for CBCT-to-CT image synthesis⁵¹, the dosimetric accuracy analysis of dose distributions via 3D dose cube comparisons of the pCT and sCT in this work was performed with the following settings:

- (1) A global GPR with a low dose threshold of 10%/25%/50% and criteria of 2%/2 mm as well as 3%/3 mm
- (2) A dose difference pass rate (DDR) with a low dose threshold of 25%/50%/90% and deviation threshold of 1%/2%/3%, focusing on the evaluation of median- and high-dose regions.

The low dose thresholds referred to the prescription dose of 60Gy of the reference plan. Furthermore, dose difference plans between the sCT-pCT with a low dose threshold of 2% were created for several exemplary patients with the purpose of localizing largest dose discrepancies.

2.3 Evaluation of adaptive treatment planning on sCT

The second part of this thesis was concerned with evaluating the dosimetric benefits of different ART replanning strategies compared to the conventional IGRT approach. After having validated the application of the sCT model for every essential treatment component, the subsequent objective was to perform actual adaptations of the initial treatment plan on daily generated sCT and modify the segments according to the daily anatomy based on the methods of segment aperture morphing and a full re-optimization. Moreover, this research aimed to express a recommendation for the most appropriate replanning approach depending on image segmentation information. The concept of ultra-hypofractionated radiation therapy (UHF RT), i.e. the PACE-C trial, was chosen as a framework for this retrospective replanning study. Hence, section 2.3.1 describes the detailed characteristics of the PACE-C trial. Sections 2.3.2 and 2.3.3 are concerned with the investigated patient collective and the preliminary work on generating a robust treatment planning template. The four different treatment plan adaptation approaches are explained in section 2.3.4, followed by the details on the dosimetric and statistical evaluation in section 2.3.5. Most relevant outcomes of this research has been previously published¹²⁹.

2.3.1 The PACE-C trial

The trial of Prostate Advances in Comparative Evidence (PACE) was initiated by the Royal Marsden NHS and the British Institute of Cancer Research (ICR) in 2012. It is an international, multi-center randomized study and investigates clinical outcomes of different treatment modalities for early stage organ-confined prostate cancer in terms of comparing prostatectomy versus SBRT and conventional normo-fractionated RT vs. SBRT. Latest analyses of patient outcomes suggest non-inferiority with regard to gastrointestinal and genitourinary toxicity¹⁰⁶. The PACE trial has three study arms A, B, and C, with the latter being focused on patients that receive six months of hormone

therapy and were not considered candidates for surgery. Further information and latest updates can be obtained from the official PACE homepage of the ICR¹³⁰.

According to the PACE-C eligibility criteria¹³⁰, patients are included in the trial that possess low or intermediate risk prostate cancer, with a maximum Gleason score of 7 (3+4), a pre-treatment prostate-specific antigen (PSA) level of ≤ 20 ng/ml and a tumor stage of $\leq T2c$. They are randomized to receive either prostate SBRT (36.25 Gy or 40 Gy in 5 fractions to the PTV or CTV, respectively) or conventional RT (60 Gy in 20 fractions to the PTV). A strict organ preparation protocol, image-guidance such as fiducial markers and additional matching to a pelvic MRI are recommended. While for the conventional arm PTV margins of 4-8 mm are used, the range of margins in the SBRT arm is confined to 3-6 mm, depending on the application of markers. Treatment planning should strictly fulfill given dose-volume criteria (also shown for SBRT in Table 2.4). A monitoring with soft tissue matching by means of CBCT, beacons, ultrasound or fiducial markers is recommended during the plan delivery, with the overall treatment of a patient not exceeding 34 days or 14 days for the conventional and SBRT arm, respectively.

2.3.2 Study design and workflow

This retrospective treatment planning study comprised a total of 32 prostate cancer patients with low to intermediate risk disease. After IRB approval obtained by the ethics committee II of the University of Heidelberg (2018-836R-MA), three different adaptation approaches were calculated on synthetic CBCT to evaluate potential dosimetric benefits of ART over the conventional IGRT approach. Patients with total endoprostheses, positioned in prone position or unsuitable for the PACE eligibility criteria¹³⁰ were excluded from this examination. Relevant patient characteristics are displayed in Table 2.3.

Table 2.3 Characteristics of the 32 prostate cancer patients included in the adaptive treatment planning study. Only patients fulfilling the PACE eligibility criteria were selected for evaluation.

Average age and range in (years)	Pre-treatment PSA in (ng/ml)	Gleason score	Tumor stage	Average target volume in (cm³)	Comorbidity	Body-mass-index (BMI)
71.9 (48-88)	<10: 20 patients 10-20: 12 patients	6 (3+3): 9 patients 7 (3+4): 23 patients	T1c: 9 patients T2a-T2c: 23 patients	65.3 ± 26.3 (prostate) 18.3 ± 5.5 (seminal vesicles)	Diabetes: 6 Hyper- tension: 18 Cardio- vascular condition: 9	26.6 ± 2.8

Originally, all patients received a conventional normo-fractionated RT with a cumulative dose of 75 Gy delivered in 2 Gy x 30 fractions and subsequent 3 Gy x 5 fractions delivered with VMAT at a C-arm linac (VersaHD, Agility MLC, Elekta AB). The planning CT (pCT) was acquired at a standard CT (Brilliance BigBore, Philips Healthcare) with a tube voltage of 120 kV, an exposure time product of 146 mAs, a slice thickness of 1 mm and a reconstruction protocol of SBRT, according to the guidelines of SBRT imaging protocols¹³¹. Daily image guidance was performed based on kV-CBCT (XVI 5.0, Elekta AB) prior to each fraction delivery in order to enable soft tissue matching for the translational couch correction. No fiducial markers or additional intrafractional tracking were used due to the clinical routine treatment setup at the UMM department.

Machine parameters used for acquiring CBCT with a slice thickness of 2 mm were 120 kV tube voltage, 132 mAs exposure time product, an axial length of 27.7 cm (“M-preset”) and a gantry speed of one revolution per minute. Starting with the first treatment fraction, CBCT of every second treatment fraction were selected (min. 2 days and max. 3 days between every selected fraction), adding up to five CBCT per patient, as stated in the PACE-C trial guidelines (7.25 Gy x 5 fractions)¹³⁰. The time between the pCT and the first fraction CBCT was on average 4.2 ± 1.7 days. Thus, the validity of this retrospective treatment planning approach is dependent on the assumption that anatomical variations hardly differ between a CF RT and a UHF RT. After the translational and rotational image registration of the CBCT and the pCT in the XVI system, every selected CBCT was reconstructed in the reference system of the pCT and imported into the treatment planning system (TPS) (Monaco research version 5.17, Elekta AB). Subsequently, all CBCT were transformed into sCT within the aforementioned cycle-GAN-based pelvic sCT model in ADMIRE and, just like the pCT, assigned with the scanner-specific HU-ED-calibration curve.

In a next step, the organ structures of the prostate, seminal vesicles (SV), bladder, rectum, small bowel, bilateral femoral heads, anus and penile bulb were delineated on both pCT and the five respective sCT by an expert physician. According to the contouring guidelines of the PACE-C trial, the CTV was obtained by adding the total volume of the prostate to the proximal 1 cm-volume of the SV. This was handled by creating a 1 cm margin around the prostate contour and expanding the CTV to the intersection line with the SV. In contrast to CF RT where the planning target volume (PTV) margin is usually defined as the CTV+5-9 mm (except for smaller margins at the posterior rectum-interface), the PTV margin for UHF RT is defined as CTV+4-5 mm and PTV+3-5 mm at the rectum interface. In this study, a uniform PTV margin of 4 mm around the CTV was utilized. A schematic and exemplary slices of the delineated target structures are presented in Figure 2.4.

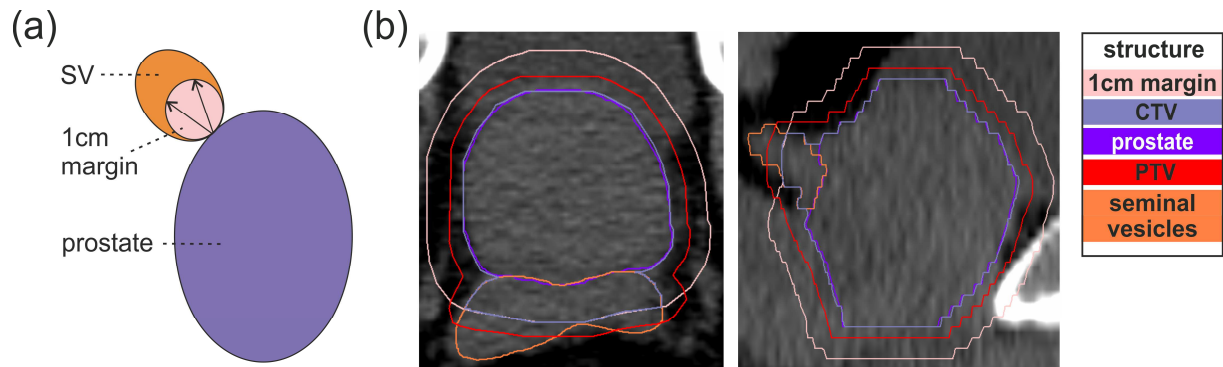


Figure 2.4: Schematic for creating the CTV according to the PACE guidelines (a) and exemplary axial as well as sagittal views (b) of the delineated target structures of the 1 cm margin, CTV, prostate, PTV and seminal vesicles (SV).

The process of treatment planning consisted of two major parts: First, a general SBRT treatment planning template in Monaco was generated in line with the guidelines and dosimetric criteria of the PACE-C trial¹³⁰ (see section 2.3.3). It was then applied with minor adjustments to the pCT of every patient in the total collective in order to create reference plans. Second, these reference plans were used to generate new treatment plans on the daily sCT which represented the IGRT approach and the three different adaptive replanning approaches (see section 2.3.4). For all treatment plan calculations, a nominal beam acceleration potential of 10 MV with a flattening filter, VMAT delivery with a dual arc of 360° and a maximum of 120 control points per arc with a minimum segment width of 0.5 cm were used. The dose calculation algorithm was Monte Carlo-based and calculation properties of 1% statistical uncertainty as well as a grid size of 2 mm were selected for all treatment plans according to the recommendation guidelines for SBRT treatment planning¹³². As time is of crucial essence in a daily performed ART workflow, all treatment plans were furthermore calculated with a grid size of 3 mm. In total, 21 plans for every of the 32 patients were created, summing up to 672 treatment plans being analyzed within the scope of the second part of this thesis.

2.3.3 SBRT dose criteria

The SBRT treatment planning template was constructed to fulfill all dose criteria given by the PACE-C trial guidelines¹³⁰, which are presented in Table 2.4. Grey shaded areas denote specific dose criteria which were most difficult to achieve and thus the most substantial ones during the treatment plan optimization process.

Table 2.4: Dose criteria of the PACE-C trial¹³⁰

Target volumes	Dose in (Gy)	Volume
CTV	40	≥ 95% (allowed minor variations: 90%-94.9%)
PTV	36.25	≥ 95% (allowed minor variations: 90%-94.9%)
	34.4	98%
Organs at risk		
Rectum	36	< 2 cm ³
	29	< 20 %
	18.1	< 50 %
Bladder	37	< 10 cm ³
	18.1	< 40 %
Bowel	18.1	< 5 cm ³
	30	< 1 cm ³
Femoral heads	14.5	< 5 %
Penile bulb	29.5	< 50 %

The generation process of the template involved five treatment planning test runs, each being performed for the pCT of 10 patients of the total population that represented the complete range of anatomical variations from convenient to unfavorable locations of the OAR adjacent to the PTV. The center of the CTV was selected as isocenter (ISO). Additional to the standard evaluation of the PACE-C dose criteria, their standard deviation (SD), the spatial distribution of the isodose lines in the 4mm margin around the CTV and the rescaling factor of the normalization to the prescription dose of each plan was taken into account. Ideally, a treatment plan already comes very close to all target dose criteria without normalization and does not need to be rescaled more than 5% in order to avoid uncontrollable dosimetric deviations after the optimization process. If comparably large rescaling is inevitable, it is usually more favorable to aim for a downscaling as this prevents OARs from receiving overdose by means of the normalization. The final PACE-C treatment planning template, valid for Monaco research v5.17, can be obtained from Figure 2.5.

Both CTV and PTV coverage are managed by a “target penalty” cost function with a selected coverage of 99% for the CTV and 95% for the PTV. A very small isoconstraint of the CTV “quadratic overdose” ensures a steep dose gradient for the maximum dose, ideally below 48 Gy. “Parallel” and “serial” cost functions for the bladder and rectum control the overdose of these two most relevant OAR. The utilized shrink margins were introduced to enable a more balanced dynamic between target and OAR cost functions during the optimization process. Together with the isoconstraint parameter, the shrink margins can be used most efficiently to adjust OAR overdose, especially for the serial cost function. The bowel and sigmoid colon were not included in the IMRT constraints since they were never subject to receive potential overdose due to the high conformal VMAT dose distribution. Although not directly mentioned by the PACE-C guidelines, the anus was included since its constraint functioned as an additional help structure to shield high doses in the inferior direction towards the penile bulb.

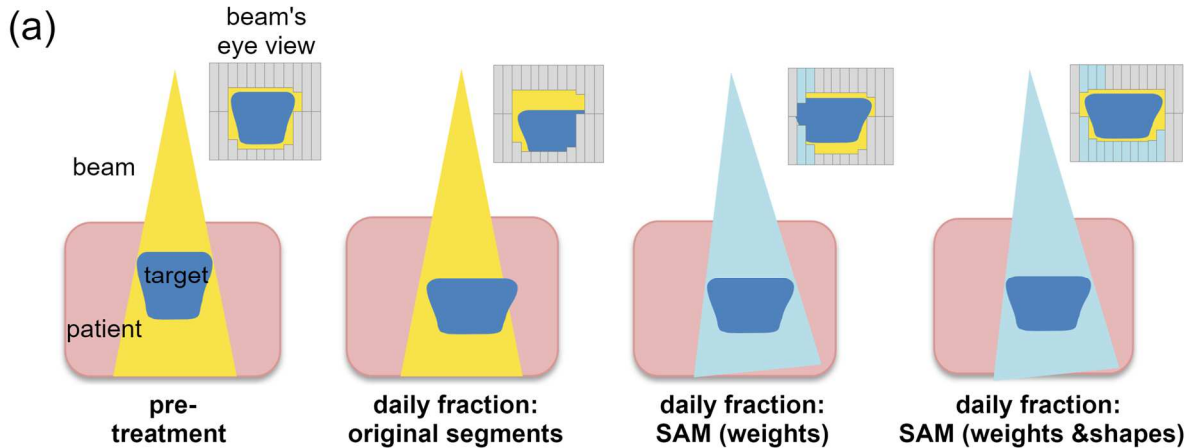
Structure	Cost Function	Reference Dose (cGy)	Multicriterial	Power Law Exponent	Shrink Margin (cm)	Isoconstraint
CTVpsv_4000	Target Penalty					4250.0
	Quadratic Overdose	4700.0				2.0
PTVpsv_3625	Target Penalty				0.00	3800.0
	Quadratic Overdose	3800.0			0.00	90.0
	Quadratic Underdose	3750.0			0.00	75.0
Bladder	Parallel	1400.0	<input type="checkbox"/>	2.00	0.55	20.00
	Serial		<input type="checkbox"/>	6.00	0.35	1600.0
Rectum	Parallel	1500.0	<input type="checkbox"/>	2.00	0.25	28.00
	Serial		<input type="checkbox"/>	3.00	0.25	1250.0
Anus	Serial		<input type="checkbox"/>	2.00	0.00	1600.0
FemorallHead_L	Serial		<input type="checkbox"/>	3.00	0.10	1000.0
FemorallHead_R	Serial		<input type="checkbox"/>	3.00	0.10	1000.0
PenileBulb	Serial		<input type="checkbox"/>	2.00	0.10	2800.0
patient	Quadratic Overdose	2000.0	<input type="checkbox"/>		0.70	100.0
	Conformality		<input type="checkbox"/>			0.55

Figure 2.5: Treatment planning template for optimization constraints in Monaco research v5.17 in accordance with the PACE-C trial guidelines for prostate SBRT.

2.3.4 Segment aperture morphing and adaptive replanning approaches

Apart from using pre-built treatment plan libraries^{61,62} or fast automated “morphology of the day” approaches driven by fiducial points⁶³, the technique of segment aperture morphing (SAM) constitutes a promising solution for efficiently adapting a treatment plans on a daily basis. SAM approaches are associated with the field of warm start optimization (WSO) procedures which make us of a-priori information of a given reference plan in order to reduce the total plan calculation time. Previous plan parameters like fluence, beam angles, segment widths, MLC shapes and/or weights help to guide the complex optimization process and thus avoid a start from scratch. The technique of SAM was initially established by Ahunbay et al.⁶⁴ and is described in Figure 2.6. Due to anatomical variations the original treatment plan segments of the pre-treatment situation will not fit to the daily situation of every treatment fraction, triggering a mandatory plan adaptation. The SAM approach solves that issue by modifying every single leaf position of the MLC for every plan control point via the beam’s eye view according to the respective change between the reference target shape and the actual target shape. Depending on fully or partially blocking the target,

each leaf either preserves its distance to the target edge in every direction or only in the leaf travel direction¹³³, as shown in Figure 2.6, panel (b). Subsequently, further adjustments of the segment weights, i.e. the monitor units, can be performed or additional modifications of the segment shapes for achieving dosimetric goals of the reference dose distribution on the pCT. Additional refinements of the SAM procedure like gradient maintenance or reduced warm start complexity through automated plan choice of pre-shifted plans were proposed in related literature^{134,135}.



(b)

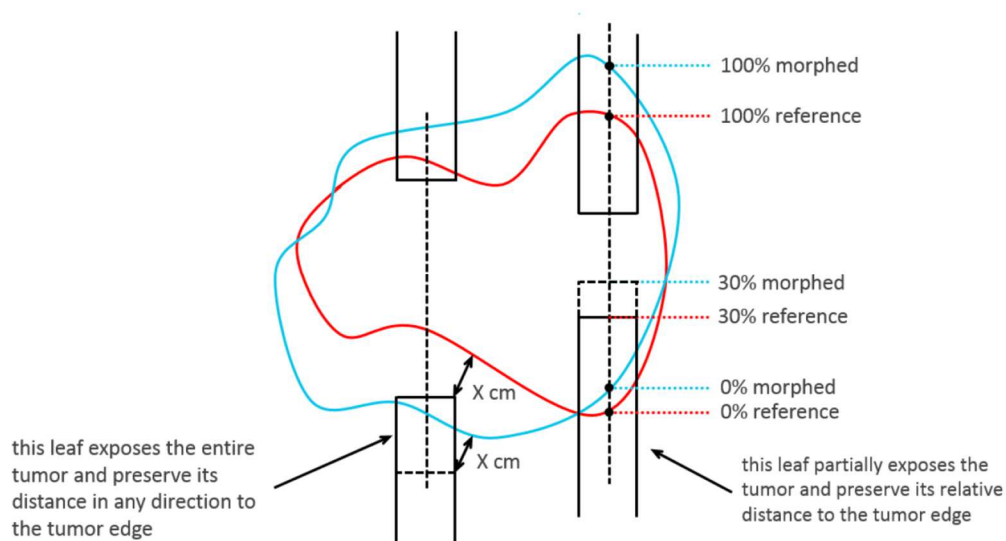


Figure 2.6: a) Schematic overview of MLC modifications of the SAM technique (adapted from ⁶⁶) and b) detailed SAM of single leaves with respect to the target shape (see ¹³³)

In this research study, the following parameters were used in the plan adaptation settings via SAM: maximum leaf change of 3 cm, model 2 with an OAR weight of 300 and activated gradient control, a calculation frequency of 0.5 for VMAT and maximum iteration of 50, 20 and 5 for the segment weight optimization (SWO), the segment shape optimization (SSO) and the overall iterations of SWO+SSO, respectively. The SWO+SSO is able to stop before reaching the maximum number of iterations if the convergence criterion of the objective function of not being decreased by 5% in the last three iterations is met. Further parameters for the WSO process can be obtained from the WSO whitepaper of Elekta¹³⁶.

In order to quantify the dosimetric benefits of ART compared to the conventional IGRT treatment, four different treatment plan adaptation approaches were calculated on each daily sCT of the 32 patients. In all of the following scenarios, the center-of-mass of the respective CTV was selected as ISO for dose calculations on the pCT and sCT:

- (I) “IGRT” approach: In order to reconstruct the IGRT treatment, an unmodified copy of the reference plan was generated on the rigidly registered sCT. The treatment plan on the sCT was not rescaled. While the isocenter position (ISO) on the pCT was the center-of-mass of the CTV, the ISO on the sCT was generated based on the translational and rotational corrections.
- (II) “ART1” approach: SAM was performed based on the original treatment plan, followed by a segment weight optimization. The adapted dose distribution on the sCT was then rescaled to cover 95% of the CTV with a prescription dose of 40Gy, as given by the PACE-C guidelines. This rescaling was also applied for the approaches (III) and (IV)
- (III) “ART2” approach: The same procedures as in approach (II) were performed, complemented by an additional modification of the MLC segment shapes within the WSO.
- (IV) “ART3” approach: In contrast to all previous approaches, no a-priori information was used. Using identical settings of the IMRT constraints as the reference plan on the pCT, the ART3 approach comprised a full re-optimization of the treatment plan on the sCT.

All dose calculations were carried out on a workstation with a dual core Intel Xeon E5-2687W v4 3.0GHz processor, 64GB RAM and an Nvidia Quadro P 6000 GPU. Moreover, the calculation time of every treatment plan process (optimization + dose calculation) was recorded to assess clinical feasibility.

2.3.5 Dosimetric and statistical evaluation

In total, four different treatment plans on each of the five daily sCT for all 32 patients were created, resulting in 160 treatment plans being calculated per treatment plan adaptation approaches within this study (4 different replanning approaches x 5 sCTs x 32 patients). First and with regard to the spatial characteristics of the treatment plans, exemplary sagittal slices of the ISO location were analyzed by creating difference maps between the re-optimization approaches and the IGRT approach in the TPS with a low dose threshold of 1% of the prescription dose (40 Gy). Second, mean dose-volume histograms (DVH) for the organ structures of the CTV, PTV, bladder and rectum were generated for the four adaptation approaches which contained a point-wise standard deviation (SD) of the 160 treatment plans per adaptation approach of the total patient collective.

Third, the dose criteria of the PACE-C treatment planning guidelines were evaluated by means of boxplots, including the dose-volume parameters of the 32 reference plans and the 160 respective adapted treatment plans. The dosimetric evaluation focused

on the dose-shaping and thus most relevant dose criteria which were identified to be $V_{40\text{Gy}}(\text{CTV})$, $V_{36.25\text{Gy}}(\text{PTV})$, $D_{98\%}(\text{PTV})$, $V_{37\text{Gy}}(\text{bladder})$ and $V_{36\text{Gy}}(\text{rectum})$ as well as the exemplary $V_{14.5\text{Gy}}(\text{right femoral head})$. The analysis of the remaining dose criteria can be found in the appendix in Figure 7.3. A paired t-test ($p < 0.05$ considered as statistically significant) between the results of the four relevant PACE-C dose criteria between the four different adaptation approaches IGRT, ART1, ART2 and ART3 was performed in order to identify possible coherences between all adaptive replanning techniques.

The aforementioned standard evaluation metrics were extended by applying a scoring system to the generated treatment plans similar to the one proposed by the ESTRO QUASIMODO group¹³⁷ in order to quantify the overall benefit of adaptive replanning over the conventional IGRT approach with respect to single treatment plans as well as single dose criteria. The penalty score S was defined as the percentage difference between the actual result of a certain dose criteria on the sCT “M” and its respective dose constraint given by the PACE-C treatment planning guidelines¹³⁰ (see Table 2.4). Thus, only violations of dosimetric criteria lead to counts of S , resulting in a value of $S=0$ for treatment plans fulfilling all PACE-C dose constraints:

$$S = \sum_n \begin{cases} \left| \frac{M_n - C_n}{C_n} \right| \times 100, & \text{if the dose-volume criteria is exceeded} \\ 0, & \text{else} \end{cases} \quad (2.12)$$

Dependent upon the evaluation purpose, the index n represents two different summations:

1. Inter-patient comparison: A summation over all four dose criteria per treatment plan and per patient.
2. Inter-modality comparison: A summation over all 160 treatment plans per approach and per dose criterion.

The penalty evaluation was performed for the four most relevant dose criteria which were $V_{36.25\text{Gy}}(\text{PTV})$, $D_{98\%}(\text{PTV})$, $V_{37\text{Gy}}(\text{bladder})$ and $V_{36\text{Gy}}(\text{rectum})$. The criterion $V_{40\text{Gy}}(\text{CTV})$ was excluded since all treatment plans were rescaled to this dose-volume parameter to cover 95% of the CTV. Moreover, a simple count of violations was performed for the four relevant dose criteria (“pass”=count 0, “violation”= count 1) in order to portray the potential benefits of a percentage penalty scoring.

The last part of the treatment plan evaluation was concerned with predicting certain dosimetric deviations by assessing organ segmentation results in order to give guidance for finding the most suitable of the proposed adaptation approaches. Overlap volumes between the bladder and PTV “ $V_{\text{PTV} \cap \text{bladder}}$ ” as well as between the rectum and the PTV “ $V_{\text{PTV} \cap \text{rectum}}$ ” were determined in (cm^3) for every pCT and sCT. Figure 2.7 shows the properties of the two overlap volumes for an exemplary patient.

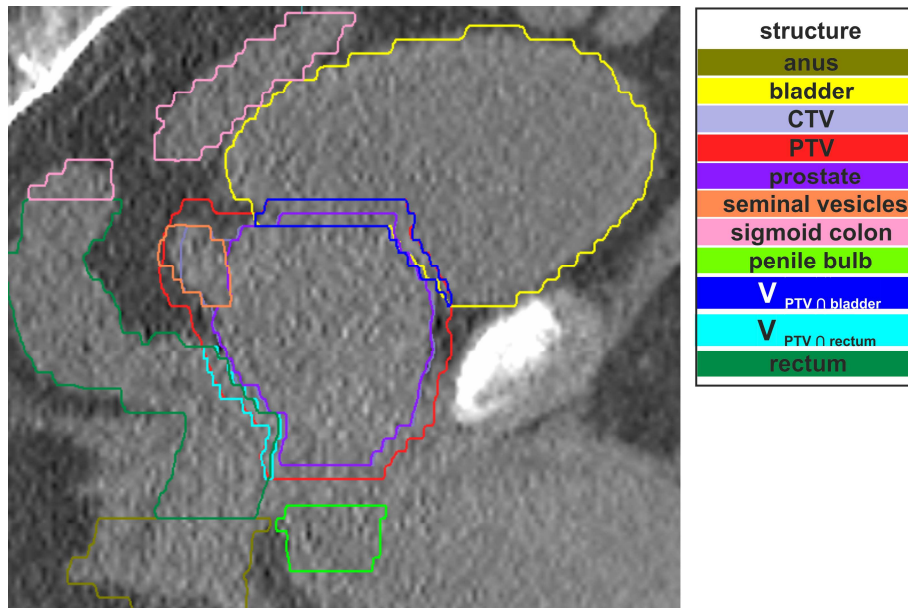


Figure 2.7: Overlap volume between the PTV and the bladder (dark blue) and between the PTV and the rectum (light blue) for a sagittal slice of the planning CT of an exemplary patient.

Furthermore, Pearson's correlation coefficients were calculated between the two OAR overlap volumes and the total penalty score S of the respective treatment plan for every re-optimization approach (ART1-ART3) to evaluate the general correlation between the extent of the overlap and the single treatment plan quality. Eventually, a ratio was calculated for all four adaptation approaches, aiming for identifying a threshold for the overlap volume that defined potential overdose to the OAR. The amount of above-average overlap volumes and coinciding, close-to-threshold dose criteria $V_{37\text{Gy}}(\text{bladder}) > 9\text{ cm}^3$ or $V_{36\text{Gy}} > 1.5\text{ cm}^3$ was divided by the amount of all treatment plans in the total collective possessing $V_{37\text{Gy}}(\text{bladder}) > 9\text{ cm}^3$ or $V_{36\text{Gy}} > 1.5\text{ cm}^3$:

$$\frac{V_{\text{PTV} \cap \text{bladder}} > 7.2\text{cm}^3 \text{ AND } V_{37\text{Gy}} > 9\text{cm}^3}{V_{37\text{Gy}} > 9\text{cm}^3} \quad (2.13)$$

$$\frac{V_{\text{PTV} \cap \text{rectum}} > 2.6\text{cm}^3 \text{ AND } V_{37\text{Gy}} > 1.5\text{cm}^3}{V_{36\text{Gy}} > 1.5\text{cm}^3} \quad (2.14)$$

Moreover, the DSC of the bladder and rectum were calculated for every sCT and its related pCT in order to perform similar evaluation in terms of Pearson correlations as well as overdose prediction. Additionally, mean DVH of the $V_{\text{PTV} \cap \text{bladder}}$ and $V_{\text{PTV} \cap \text{rectum}}$ were generated and compared with their related entire organ structures.

3 RESULTS

Aiming for a complete evaluation of the adaptive workflow using the GAN-based synthetic CT model for the pelvic body site, its performance with regard to image uncertainties, segmentation quality and dosimetric accuracy were analyzed. In section 3.1.1, the image quality of the sCT is presented in contrast to the pCT and the native CBCT by means of visual slice comparison, IVHs and common image uncertainty metrics of specific VOIs. Section 3.1.2 is concerned with the segmentation quality of the ADMIRE DIR-based automatic structure generation compared to manually created structures. Section 3.1.3 contains the results with regard to the dosimetric accuracy between dose distributions on the pCT and the sCT.

In order to complement the aforementioned sCT-based ART workflow with techniques of adaptive replanning using warm start optimizations, SAM-based approaches and a full re-optimization approach were compared to the conventional IGRT approach. Dosimetric benefits of the adaptive replanning techniques over IGRT are presented in section 3.2.1 on the basis of dose difference maps, mean DVH and specific PACE-C dose criteria for relevant target volumes as well as OAR. Sections 3.2.2 and 3.2.3 expand on these standard treatment plan evaluation methods by taking a penalty scoring system as well as anatomical metrics and their correlation with dose distributions into account. Lastly, with regard to feasibility and efficiency, section 3.2.4 portrays the required calculation times for the different replanning approaches.

3.1 Evaluation of sCT

3.1.1 Image quality

Sagittal slices of two exemplary prostate patients are shown Figure 3.1 (row a) and b)), each consisting of the reference pCT, the generated sCT and the native CBCT. In row c) the respective IVHs of the pCT, sCT and CBCT are displayed for the two respective patients. Based on the visual impression, the sCT managed to improve the contrast and image intensity to a level close to the reference pCT. This leads to a more accurate assignment of image grey values in (HU) to the CT numbers. For both patients, the green-colored sCT IVH showed a good agreement to the blue-colored pCT whereas the red-colored CBCT IVH deviated in CT number location as well as in shape or volume distribution, respectively. Differences between the two patients can be found in the CT number area above 0 HU where the pCT of P11 exhibited two peaks instead of one like P14. The sCT IVH shape of patient P11 failed to recreate the second minimum of the pCT (around 25 HU) and the third peak (around 50 HU) of the reference pCT. Furthermore, it can be recognized that the CBCT and sCT of P11 exhibited additional flatus in the rectum which was not present in the pCT. Moreover, organ borders appeared to be more distinct through the sCT creation but still showed some

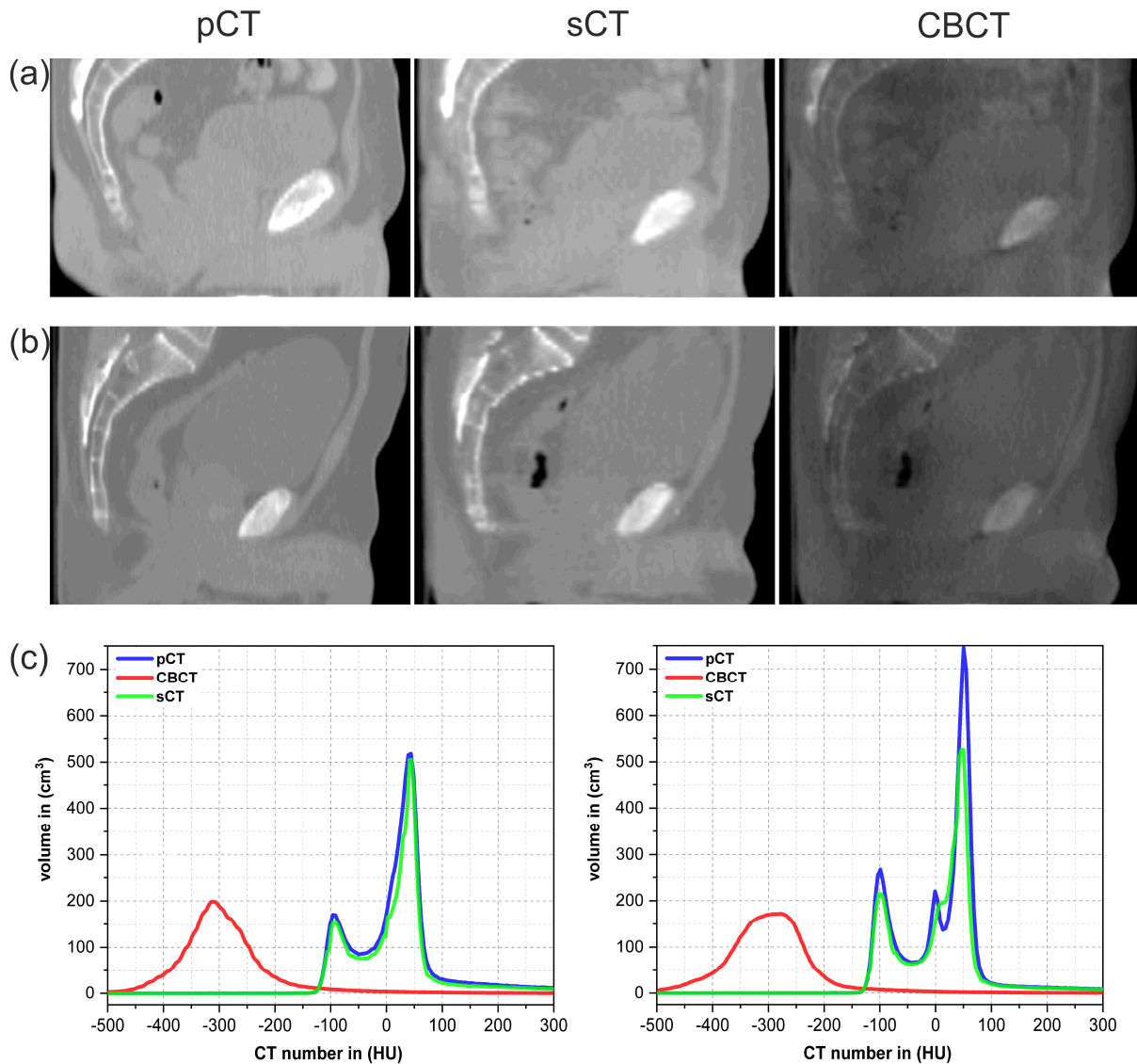


Figure 3.1: Planning CT (pCT), cone-beam CT (CBCT) and synthetic CT (sCT) of two exemplary patients (panel (a): Patient P14, panel (b): Patient P10) with window level settings of [-900 700] HU. Panel (c) depicts intensity-volume-histograms (IVH) for the pCT, CBCT and sCT for the body contour VOI minus a 15 mm margin.

blurred outlines, rather for patient P10 than for patient P14 and especially in the area of the rectum and the small bowel. IVH of all 15 patients containing single plots as well as range plots for the pCT, CBCT and sCT can be found in the appendix. Based on Figure 7.1 it becomes evident that the majority of all patients (9 out of 15) possessed a total of two peaks for the pCT and the sCT IVH, all located around -100 HU and 50 HU. These CT number regions are assigned to EDs of fat and soft tissue⁶. Similar to the exemplary patient P11 largest deviations between the pCT and sCT IVH shape could be detected rather for volume maxima than for minima. Figure 7.2 shows range plots of the three image types pCT, CBCT and sCT together with a generated average curve. The SD calculated over the total relative volume range were 4.56%, 4.36% and 3.66% for the pCT, CBCT and sCT respectively. X/Y coordinates of the identified two peaks for the pCT or sCT, respectively, were on average located at -98.2 HU/195.2 cm³ and 42.8 HU/525.9 cm³ or -95.1 HU/160.1 cm³ and 44.6 HU/467.8 cm³. The CBCT only showed one maximum at -307.4 HU/ 171.1 cm³. Figure 3.2 contains the single results

for the mean error (ME) and the mean absolute error (MAE) for the three VOIs of the total body contour, bones and soft tissue with respect to the CBCT and the respective sCT. While the CBCT exhibited comparably large values of up to -437.7 HU for the mean ME, the sCT achieved mean ME close to 0 HU for the body contour and the soft tissue VOI. Except for the soft tissue VOI, mean ME of the sCT were significantly different from a null distribution of 0 HU (indicated by the symbol *).

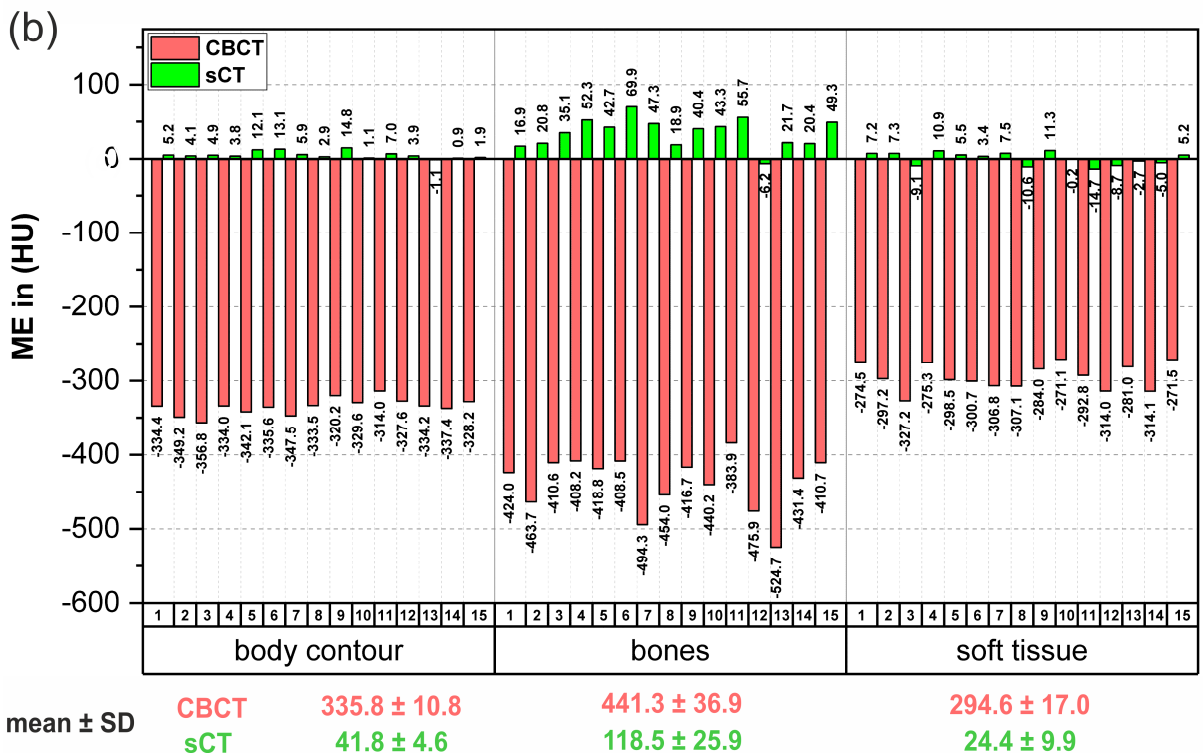
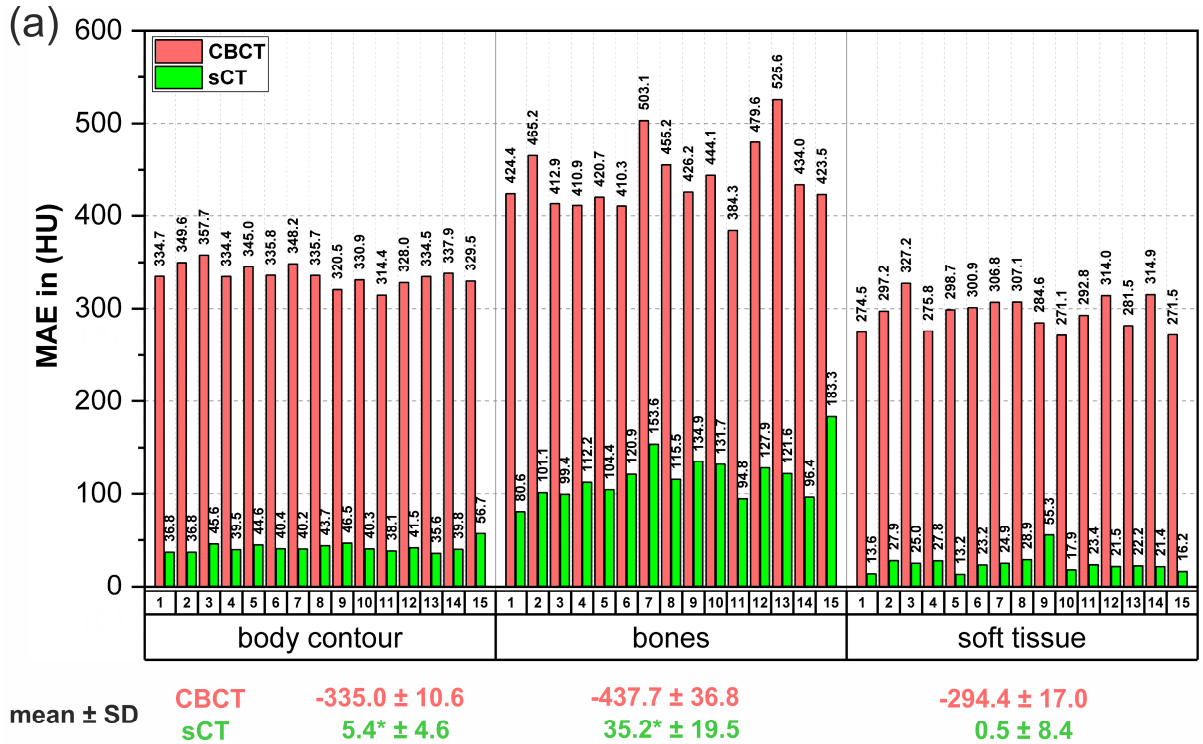


Figure 3.2: Single ME (a) and MAE (b) in (HU) of the red-colored CBCT and green-colored sCT for the VOIs of the total body contour, bones and soft tissue for 15 pelvic patients. Mean ± SD for the ME and MAE of the three VOIs for the CBCT and sCT are displayed below the respective diagram. The symbol * denotes significant differences between the mean ME and 0HU determined by a two-tailed t test ($p \leq 0.05$).

MAE values were substantially reduced from a maximum of 441.3 HU to 118.5 HU by applying the sCT model. For both ME and MAE, the analysis of the bones VOI yielded the largest results for the CBCT/sCT with -437.7/35.2 HU for the ME and 441.3/118.5 HU for the MAE. The image uncertainty of the soft tissue was found to have the lowest values for the soft tissue VOI for the ME as well as MAE with 0.5 HU and 24.4 HU, respectively. Although the inter-patient SD was already comparably small in all scenarios (maximum 36.9 HU), it was further diminished through the sCT conversion to a minimum of 4.6 HU in case of the body contour VOI. The image noise of the reference pCT was obtained through an SD of 11.4 HU.

3.1.2 Segmentation accuracy

In addition to low image uncertainties the accuracy of automatically generated structures on the sCT is of vital essence for a robust and efficient online adaptive workflow since the segmentation on the daily acquired images usually constitutes the most time-consuming part of daily online ART procedures being carried out during the patient remains on the treatment couch. The mean results for the five segmentation metrics of relevant OAR and the SV between the manually and DIR-based generated structures are illustrated in Table 3.1.

Table 3.1: Dice similarity coefficient (DSC), Sensitivity (SEN), Specificity (SPEC), Hausdorff distance (HD) and mean surface distance (d_{mean}) for the organ structures bladder, prostate, rectum and seminal vesicles. Results are displayed with respect to mean values \pm SD based on the collective of 15 pelvic patients.

Organ structures	DSC in (%)	SEN in (%)	SPEC in (%)	HD in (mm)	d_{mean} in (mm)
bladder	90.5 \pm 3.6	88.1 \pm 7.0	95.8 \pm 2.2	15.3 \pm 9.2	2.7 \pm 1.7
prostate	85.9 \pm 3.3	83.6 \pm 5.2	93.4 \pm 2.4	8.6 \pm 3.0	2.2 \pm 0.7
rectum	81.0 \pm 3.3	75.0 \pm 7.9	97.4 \pm 1.7	14.3 \pm 7.2	2.5 \pm 1.3
seminal vesicles	66.7 \pm 8.3	78.9 \pm 8.3	88.3 \pm 3.8	11.5 \pm 2.6	1.9 \pm 0.4

The dice similarity coefficient (DSC) varied between a maximum of 90.5% for the bladder and a minimum of 66.7% for the seminal vesicles (SV). The sensitivity (SEN) was always lower than the specificity (SPEC) for all four analyzed organs. While the largest SEN was obtained for the bladder (88.1%), the rectum possessed the maximum SPEC of 97.4%. Except for the SV, the SD for the DSC and SPEC were comparably small with a maximum of 3.6% and 2.4%.

In contrast to this, the evaluation of the Hausdorff distance (HD) and mean surface distance (d_{mean}) yielded large variations within the patient collective of up to $SD=9.2\text{mm}$ for the HD and $SD=1.7\text{mm}$ for the d_{mean} , both being identified for the bladder. The bladder also showed the largest absolute mean values for both distance metrics with 15.3mm and 2.7mm , followed by the rectum, SV and prostate. Furthermore, the prostate exhibited by far the smallest HD with 8.6mm . The ADMIRE deformable image registration (DIR)-based contour propagation needed on average $(30 \pm 5)\text{s}$ for generating a complete structure set on the sCT. The subsequent manual correction of one automatically generated structure set performed by an expert physician took $(5.2 \pm 1.6)\text{min}$.

Although the five aforementioned segmentation metrics are recommended throughout the available literature^{127,138} and widely used for evaluating automatically generated structures on synthetic images⁵¹, they are not entirely able to substitute the visual inspection of the actual patient anatomy. For this reason, sagittal and transverse slices of three exemplary patients including both the manually contoured and the DIR-based structures are presented in Figure 3.3.

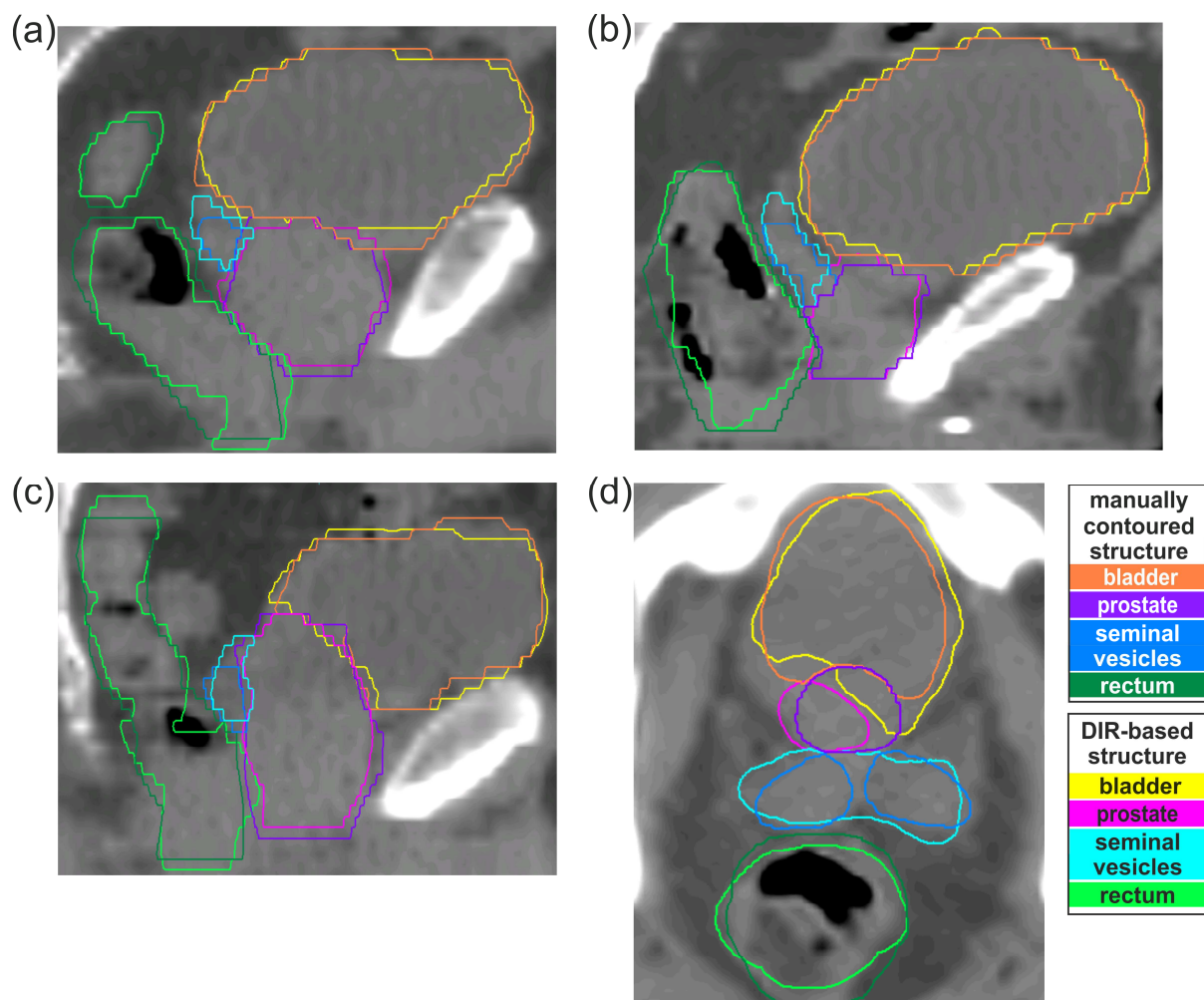


Figure 3.3: Sagittal slices with manually contoured and DIR-based generated structures for three exemplary patients ((a): P6, (b): P9 and (c): P14) on the first-fraction synthetic CBCT. Panel (d) contains a transverse slice of patient P9. For each of the two contouring sets, the four organ structures of the bladder, prostate, rectum and seminal vesicles are displayed.

The visual impression of the bladder and prostate reinforces the results of Table 3.1 as both organs show a high agreement between the two contouring approaches (in panels (a)-(c)). Slight inaccuracies are recognizable for the cranial and anterior region of the bladder as well as for the cranio-caudal extent of the prostate and its overlap with the bladder. The definition of this interface region between the prostate and the bladder or SV, respectively, turned out to be most difficult for the DIR-guided auto-segmentation and also for the manual delineation as shown in Figure 3.3, panel (d). Depending on the fact that entire physical intersections are not anatomically possible for the pelvis body site, the initial contour definition of the prostate and SV (PTV) and the subsequent generation of the OAR has a great impact on the entire structure layout in the high dose region around the PTV.

The discrepancies between the automatically and manually generated structures of the rectum become evident for locations with a lot of rectal gas (panel (b) and (c)), for the cranial transition to the sigmoid colon (panel (c)) and the anterior border towards the SV and the prostate. As already determined by the segmentation metrics, the SV visually showed the worst match between the two contouring approaches. Particularly in the superior region and in terms of defining the junction of both single vesicles larger deviations of the DIR-based structures were noticeable.

3.1.3 Dosimetric accuracy

Accurate dose distributions constitute the third essential component for a reliable ART workflow because they function as a basis for evaluating daily treatment doses to the PTV and OAR and trigger treatment plan modifications, if necessary. Figure 3.4 displays the relative dose differences D_{98} , D_{50} and D_2 for the gross tumor volume (GTV) (panel (a)) and the relative volume differences V_{40} , V_{50} and V_{60} for the bladder and rectum (panel (b)).

Compared to the GTV dose on the pCT, the dose on the sCT was higher for all three target dose parameters but did not exceed a mean value of 1.15%. Inter-quartile ranges (IQR) exhibited very similar results with D_2 having the largest IQR of 0.76%. In spite of being defined as an outlier, the respective value above 2% for the D_{50} parameter was still within the 1.5IQR of the D_2 parameter. Regarding the volume differences for the two relevant OAR, mean results below 0.50% and IQR below 1.0% were obtained for both bladder and rectum. The aforementioned trend of overdose on the sCT was also present for all three volume parameters and mainly expressed by the V_{60} parameter with mean values of 0.41% and 0.43%, respectively. This high dose-volume parameter exhibited the largest IQR of 0.61 for the bladder and 1.02 for the rectum. Among all the six volume parameters for the OAR, the only outlier was obtained for the V_{60} (bladder).

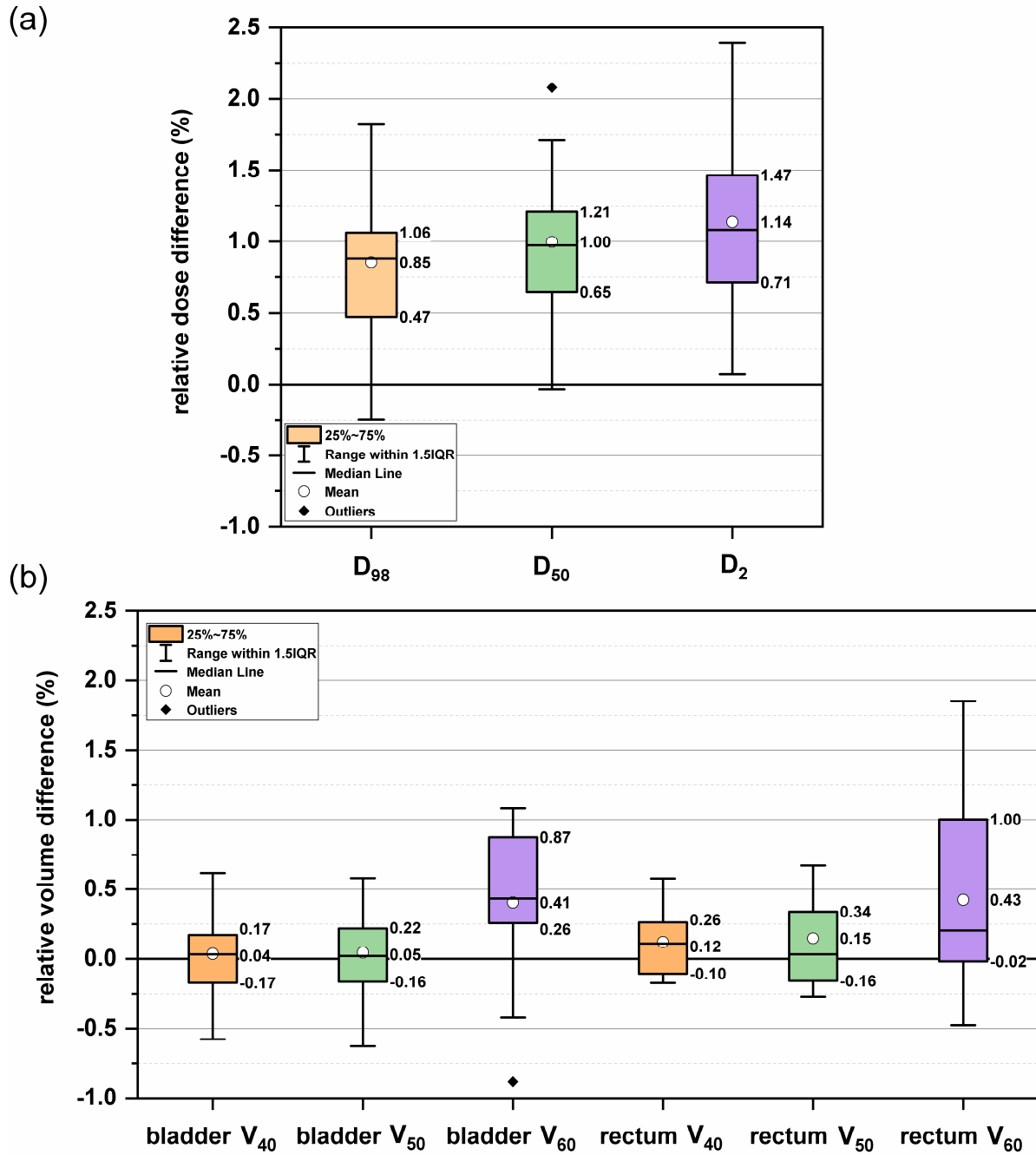


Figure 3.4: Relative dose differences of the dose-volume parameters D_{98} , D_{50} and D_2 for the gross tumor volume (panel (a)) and relative volume differences for V_{40} , V_{50} and V_{60} for bladder and rectum (panel (b)) for 15 patients of the pelvic body site. Dose and volume difference calculations were performed between the synthetic CT and planning CT (sCT-pCT), with the pCT value defined as reference. The whiskers represent the data range within 1.5 times of the inter-quartile range (IQR).

The results of the 3D Gamma pass rates (GPR) and the 3D dose difference pass rates (DDR) are listed in Table 3.2. Only for a low dose threshold of 10% a mean value below the clinically relevant threshold of 95% was obtained with 94.4% for the 2%/2mm criterion. With an increasing low dose threshold the pass rates also increased, showing a maximum of 99.9% with a very low SD of 0.1% for the 3%/3mm criterion (50% low dose threshold). In contrast to the rather consistent results of the GPR, the SD of the related DDR (<1%, <2%, <3%) was substantially higher with 16.2%, 8.2% and 2.3%.

Moreover, the DDR could merely achieve a pass rate of maximum 88.9% for the high dose region above 90% of the prescription dose. The comparison with the DDR of 1% and 3% revealed that a large amount of dose discrepancies was below 2% since the DDR of 1% was close to 55% for all three low dose thresholds, including a comparably high SD of up to 19.7%. For a point-wise difference of 3% the DDR was significantly larger with a minimum of 92.6%. Similar to the GPR, DDR also increased with rising low dose thresholds, thus locating dose differences in low dose rather than in high dose regions.

Table 3.2: Pass rates of the 3D Gamma (3%/3mm and 2%/2mm criteria) and the 3D dose difference calculation (point-wise difference of <1%, <2% and <3%) performed between the dose distributions of the planning CT (reference) and the sCT, Thresholds refer to the prescription dose of 60Gy. Results are reported in terms of mean \pm standard deviation (SD) based on the collective of 15 pelvis patients.

Low dose threshold (%)	Pass rates (%)				
	Gamma (3%/3mm)	Gamma (2%/2mm)	Dose Difference (< 1%)	Dose Difference (< 2%)	Dose Difference (< 3%)
10	96.8 \pm 1.7	94.4 \pm 2.2	-	-	-
25	99.1 \pm 0.9	98.7 \pm 1.0	54.6 \pm 10.3	79.9 \pm 6.7	92.6 \pm 3.0
50	99.9 \pm 0.1	98.5 \pm 1.7	55.3 \pm 16.2	85.1 \pm 8.2	96.4 \pm 2.3
90	-	-	55.9 \pm 19.7	88.9 \pm 9.3	98.1 \pm 1.5

Based on the dose difference plans in Figure 3.5, largest dose deviations between the pCT and the sCT were recognizable for the patient outline region and at the organ interfaces between the prostate and the bladder or rectum, respectively. While patient P6 (panel (a)) exhibited larger overdoses over 7.2 Gy both at the posterior and anterior patient outline on the sCT in comparison to the reference plan on the pCT, dosimetric hotspots for patients P9 and P14 were more concentrated at the anterior patient outline and in the caudal region below the prostate (located at the penile bulb). In general, a trend towards slight overdoses on the sCT is noticeable as already obtained from the results of the detailed dose-volume parameters in Figure 3.4. While for patients P6 and P9 dose discrepancies in the range of \pm 2.4 Gy were present in the regions of rectal gas and of the posterior bladder upon the SV, patient P14 expressed more uniformly distributed dose differences throughout the entire high dose region around the GTV of the prostate and SV. Dosimetric deviations of \pm 0.8 Gy close or in the pelvic bones could be identified for all three exemplary patients.

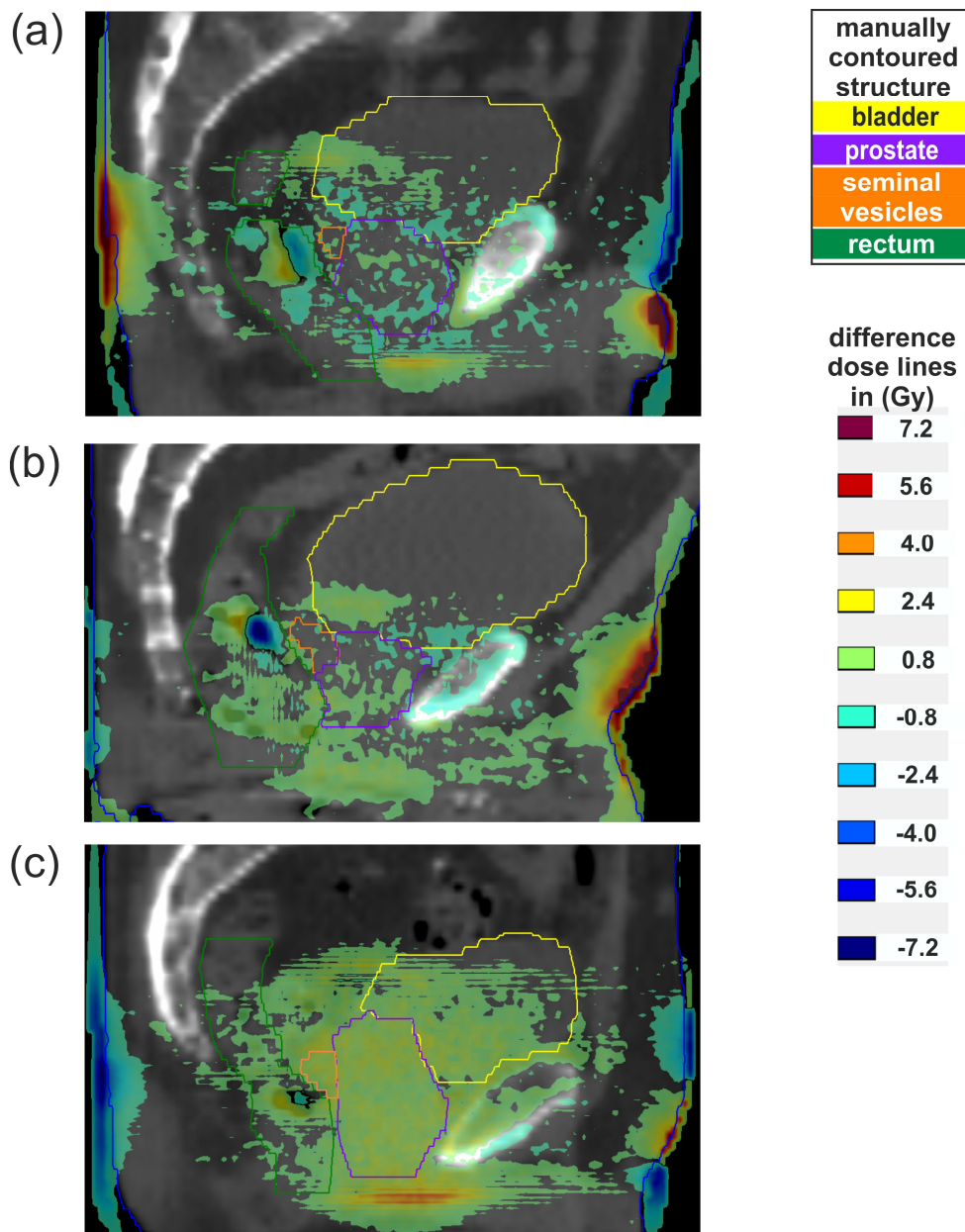


Figure 3.5: Dose difference maps between the reference plan on the pCT and the copied plan on the sCT. Sagittal slices near the isocenter on the sCT of three exemplary patients are shown ((a): P6, (b):P9, (c):P14). A prescription dose of $D(GTV)=60Gy$ and a low dose threshold of 2% was used.

3.2 Evaluation of adaptive treatment planning approaches

After having demonstrated the general applicability of the GAN-based synthetic CT (sCT) generation, the second part of this thesis is concerned with the actual daily modification of treatment plan within the framework of the ultra-hypofractionated treatment regimen of the PACE-C trial (5x8Gy to the CTV). In order to pave the way for the clinical implementation of online adaptive replanning methods, a total of 32 reference plans and 160 treatment plans per adaptation approach IGRT, ART1, ART2 and ART3 were generated on five daily sCT for each of the 32 prostate cancer patients. The aim of this procedure was to quantify dosimetric benefits of different adaptation strategies over the conventional IGRT approach. The analysis of the replanning approaches was based on obtaining and comparing standard dosimetric parameters (section 3.2.1), a penalty scoring system (section 3.2.2), additional evaluation metrics involving anatomical properties (section 3.2.3) and, for the purpose of clinical feasibility, treatment planning times (section 3.2.4).

3.2.1 Dosimetric evaluation

Figure 3.6 shows exemplary sagittal dose distributions of the reference plan (panel (a)), the four adaptation approaches on the first fraction sCT (panel (b)-(e)) and the respective dose difference maps between the three re-optimization approaches ART1-ART3 and the IGRT approach (panel (f)-(h)). Compared to the pCT, the sCT anatomy showed some deviations with respect to a different shape of the prostate, a decreased bladder filling and increased gas volume in the rectum. The reference plan and the ART3 plan demonstrated the best visual dose conformity to the target of both prescription isodose lines of 40 Gy and 36.25 Gy for the CTV and PTV, respectively. The IGRT approach yielded the worst coverage of both target volumes with the 40 Gy isodose line even extending to regions of bladder and surrounding tissue in anterior direction. The ART1 and ART2 plans showed adequate sparing of the OAR with dose gradients similar to the reference plan. Although both re-optimization approaches exhibited an increased target conformity of the two prescription doses some deviations are noticeable particularly in the small 4 mm margin between the PTV and CTV for the ART1 approach. By means of the dose difference maps it becomes evident that overdoses to surrounding tissue and OAR were substantially reduced by up to 8 Gy (denoted by dark blue areas) by re-optimizing the reference plan with the ART1 and ART2 approach. The ART3 approach achieved the highest dose reduction with the largest extent along the PTV-bladder interface and in the superior region of the rectum. Apparently misleading yellow and orange colored areas in the caudal region of the rectum close to the PTV indicate a dose increase by the re-optimization approaches but were actually related to a displaced dose distribution and thus underdosed area in the IGRT plan.

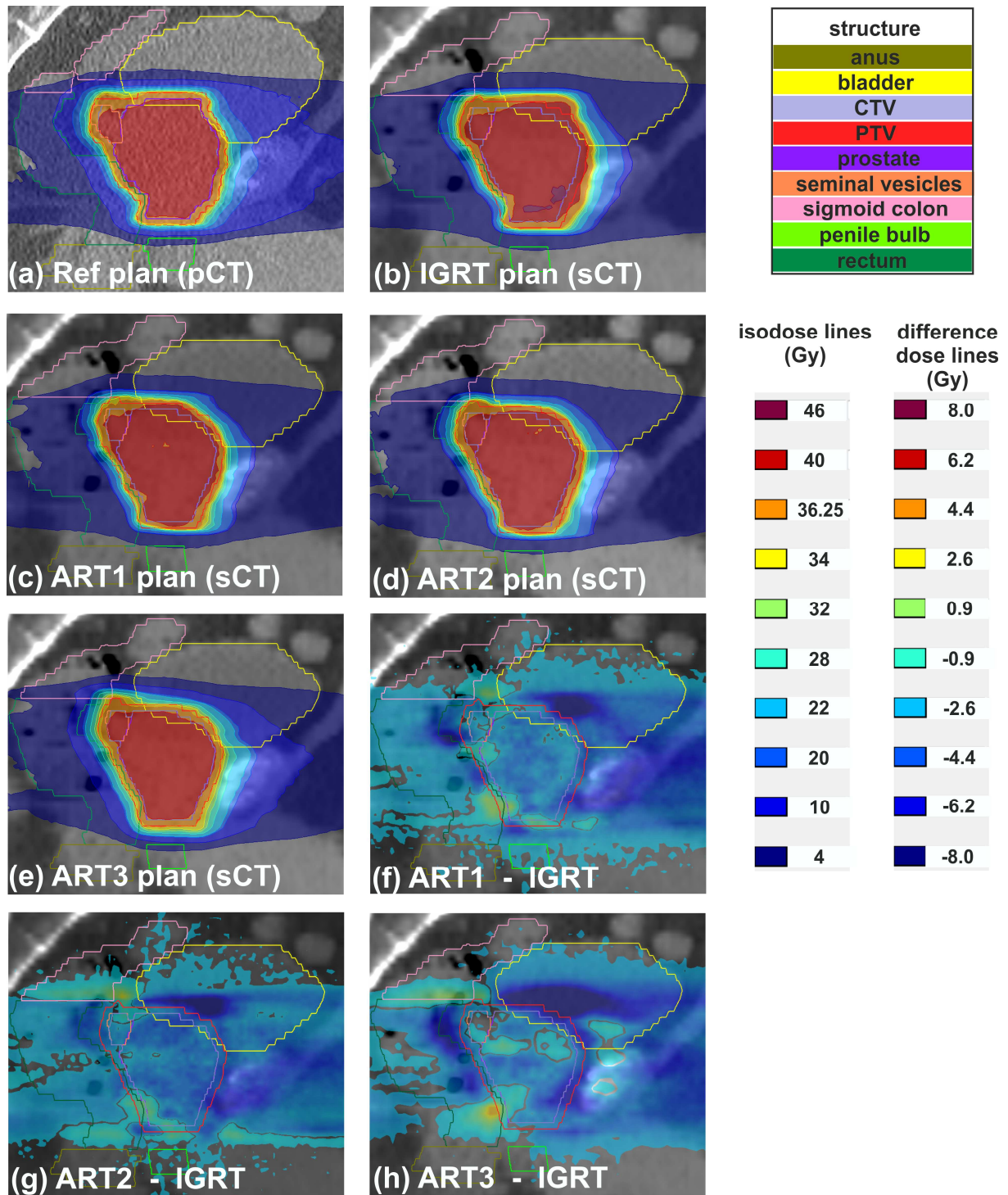


Figure 3.6: Exemplary sagittal dose distributions of the reference plan on the planning CT (pCT) (a), of the ART3 plan on the synthetic CT (sCT) (b) and of the IGRT plan on the sCT (c). Dose difference maps between the IGRT approach and the three adaptive approaches on the sCT (d-f) revealed anatomical regions in the rectum, bladder and soft tissue with dose differences of up to 8 Gy. Prescription doses were $D(CTV)=40$ Gy and $D(PTV)=36.25$ Gy. A low dose threshold of 1% referring to 60 Gy was used for the dose difference maps.

The mean cumulative DVH of the CTV, PTV, bladder and rectum are shown in Figure 3.7 with regard to the reference plans and the treatment plans generated through the IGRT, ART1, ART2 and ART3 approaches. Mean values were based on a number of 32 or 160 treatment plans for the reference plan or the four adaptation approaches, respectively. The light-colored ribbons denote the point-wise volume SD for each structure. It is evident that the IGRT approach showed the largest SD ribbons for all four displayed structures. A comparably wide spread of obtained volumes per dose was especially present in regions around both prescription doses of the CTV (40 Gy) and PTV (36.25 Gy) where targets overlapped with the OAR bladder and rectum.

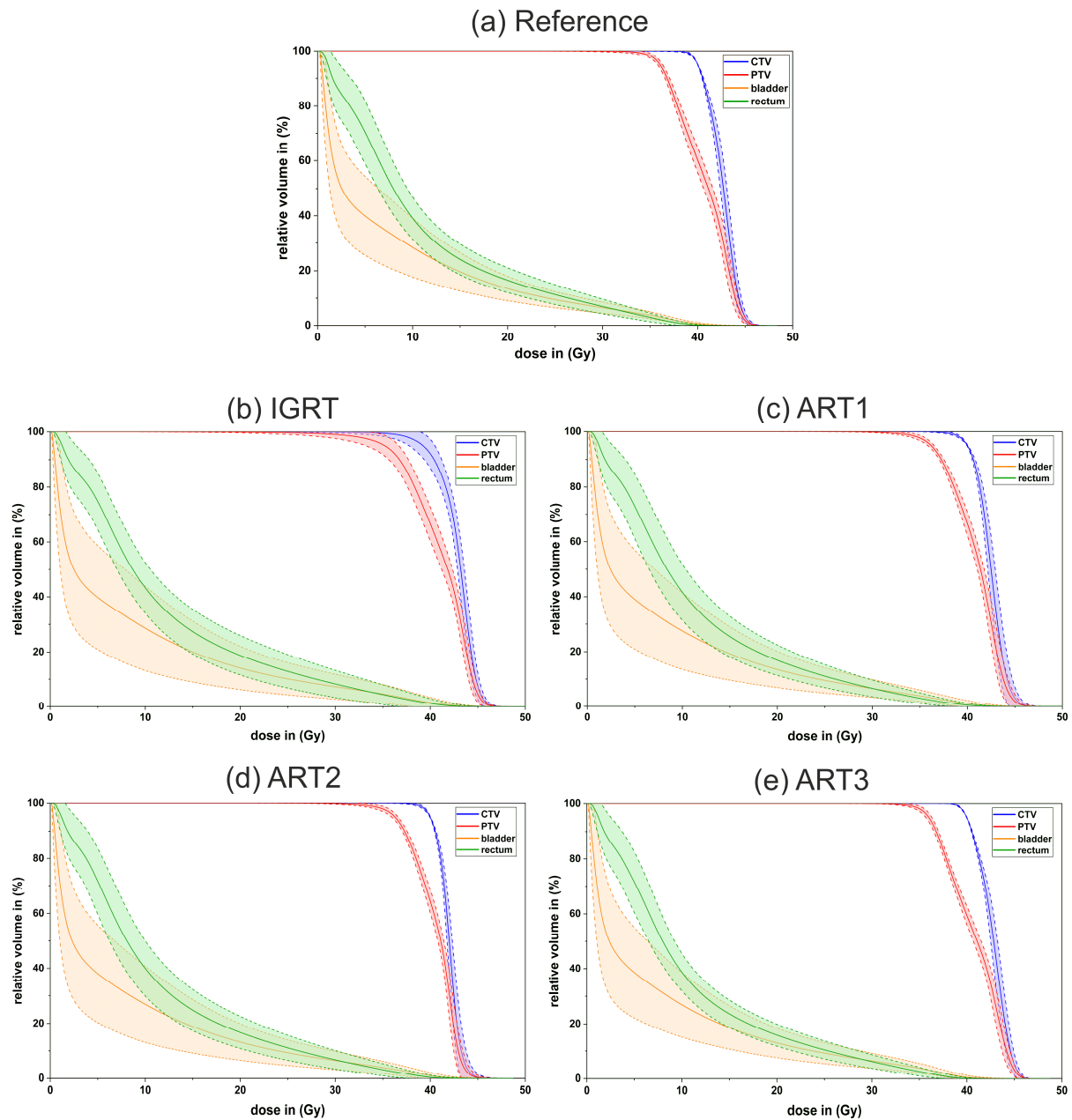


Figure 3.7: Mean dose-volume histogram of the CTV, PTV, bladder and rectum for reference plan and the four adaptation approaches IGRT, ART1, ART2 and ART3. Light colored ribbons represent the point-wise standard deviation among a collective of 160 plans per treatment planning approach. Prescription doses were $D(\text{CTV})=40$ Gy and $D(\text{PTV})=36.25$ Gy.

The SD decreased with an increasing degree of adaptation which was particularly noticeable for the OAR above 30Gy. The mean SD over the total histogram of the bladder/rectum volumes were 5.20/4.16%, 7.87/5.35%, 6.88/4.73%, 7.04/5.02% and 6.11/3.79% for the reference, IGRT, ART1, ART2 and ART3 plans, respectively. The mean SD for the target volumes CTV/PTV amounted to 0.62/0.85%, 1.12/1.43%, 0.76/0.81%, 0.63/0.73% and 0.61/0.70% for the reference, IGRT, ART1, ART2 and ART3 plans, respectively.

Figure 3.8 contains boxplots of the five dose-shaping and thus most relevant dose criteria based on the PACE-C guidelines¹³⁰ $V_{40\text{Gy}}(\text{CTV})$, $V_{36.25\text{Gy}}(\text{PTV})$, $D_{98\%}(\text{PTV})$, $V_{37\text{Gy}}(\text{bladder})$ and $V_{36\text{Gy}}(\text{rectum})$ as well as the exemplary $V_{14.5\text{Gy}}(\text{right femoral head})$ criterion. Each boxplot includes the reference plan as well as the four adaptation approaches IGRT, ART1, ART2 and ART3. Green areas denote optimal results, orange areas mandatory and red areas unacceptable results for the respective dose-volume criteria.

The largest variations for the target volume coverage (panel (a) and (b)) were obtained for the IGRT approach with interquartile ranges (IQR) of 5.9% and 5.2%. For this approach, most outliers below the 1.5IQR are noticeable with values below 75%. However, all IQR of all approaches stayed above the mandatory coverage of 90% with the ART2 approach exhibiting the best mean coverage of $V_{36.25\text{Gy}}(\text{PTV})=95.2\%$. With regard to the $D_{98\%}(\text{PTV})$ criterion, all re-optimization approaches (ART1-ART3) achieved dosimetric results above the goal dose of 34.4Gy. While the ART3 approach yielded the smallest IQR for the $D_{98\%}(\text{PTV})$ criterion it had the largest IQR of all three re-optimization approaches for the $V_{36.25\text{Gy}}(\text{PTV})$. This corresponds to the comparably more pronounced plateau shape of the shoulder region and the steeper descent of the PTV's DVH of the ART3 approach in Figure 3.7, panel (e). The IGRT plans possessed mean point-doses of on average 32.9 Gy, being 1.5 Gy below the mandatory dose and showing the highest IQR with 3.0 Gy.

The doses to the OAR bladder and rectum were highest for the IGRT approach with mean volumes of $V_{37\text{Gy}}(\text{bladder})=7.4\text{cm}^3$ and $V_{36\text{Gy}}(\text{rectum})=2.0\text{cm}^3$ (panel (d) and (e)). Not only the IGRT approach, also the re-optimization approaches ART1, ART2 and ART3 exhibited several outliers of over 15cm^3 for the bladder and 5cm^3 for the rectum. Nonetheless, all IQR of the re-optimization approaches were well within the orange mandatory volume region requested by the PACE-C treatment planning guidelines. The ART3 approach achieved better values than the reference plan for both bladder and rectum with mean volumes of 5.2cm^3 and 1.0cm^3 . The mean results of the reference plan and the ART1, ART2 and ART3 approaches were all below 6cm^3 for the bladder and below 1.4cm^3 for the rectum.

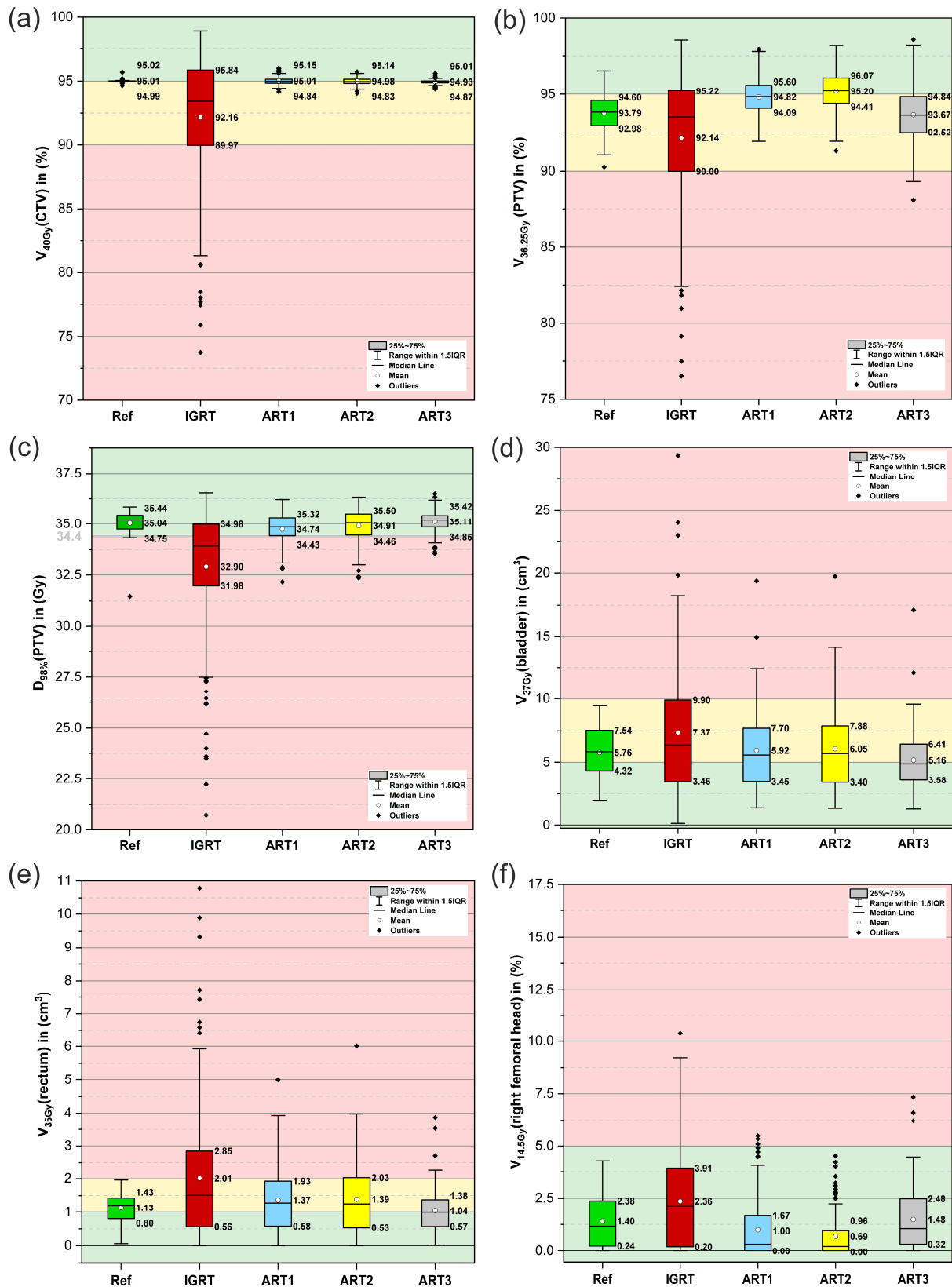


Figure 3.8: Boxplots of six dose-volume criteria for the CTV ((a)), PTV ((b)-(c)), bladder (d), rectum (e) and right femoral head (f) on the planning CT (Ref) and synthetic CT (IGRT, ART1, ART2 and ART3 approaches). Whiskers denote the data within 1.5 times of the inter-quartile range (IQR) based on the 32 plans for the reference and 160 for the four adaptation approaches. Background colors indicate optimal (green), acceptable (yellow) and unacceptable (red) results according to the PACE-C treatment planning guideline.

Although the IQR of the IGRT approach was below the threshold of 10 cm³ for the bladder, its mean volume for the V_{36Gy}(rectum) criterion was located at the maximum acceptable value of 2 cm³ with a comparable large IQR of 2.3 cm³. Overall, most violations for the dose criteria were found for the rectum. With regard to the V_{14.5Gy}(right femoral head) criterion, all IQR were substantially below the threshold of 5%. Only the 1.5IQR of the IGRT approach exceeded 9%. Few outliers could be identified for the IGRT approach as well as for the ART1 and ART3 approaches.

The respective boxplots for the remaining PACE-C dose criteria V_{18.1Gy}(bladder), V_{18.1Gy}(rectum), V_{29Gy}(rectum), V_{14.5Gy}(left femoral head) and V_{29.5Gy}(penile bulb) can be found in Figure 7.3 in the appendix. For all four dose criteria, no significant threshold violations were identified and mean percentage volumes were always best for the ART3 approach. Only in case of the left femoral head, the ART2 approach achieved the smallest mean volume with 0.89% and for this organ structure most outlier above the threshold value of 5% could be identified. The box range for the plot of the penile bulb was adjusted to 5%-95% since a large amount of the volumetric values resulted in 0%. The bowel was never subject to receiving any overdose and thus was excluded from the dosimetric analysis.

With reference to the paired t-test that was performed between the four adaptation approaches IGRT, ART1, ART2 and ART3 for the four most relevant dose criteria, significant differences were obtained for all investigated correlations. The criterion V_{40Gy}(CTV) was neither included in the statistical tests nor in the analysis with the penalty scoring system due to the rescaling of D_{95%}(CTV) to 40Gy amongst all treatment plans (except for the IGRT approach). Only the correlation of the criterion V_{36Gy}(rectum) between the ART1 and ART2 approaches showed insignificant differences with a p-value of 0.32.

3.2.2 Treatment plan penalty scoring system

In order to categorize the benefits of the presented adaptive approaches over the IGRT approach and evaluate the distribution of treatment plan quality among the entire patient collective, a penalty scoring system was applied to all calculated treatment plans. The scoring system was based on penalizing percentage differences between the actual dose-volume metric on the sCT and its reference given by the PACE-C treatment planning guidelines. The four dose criteria $V_{36.25\text{Gy}}(\text{PTV})$, $D_{98\%}(\text{PTV})$, $V_{37\text{Gy}}(\text{bladder})$ and $V_{36\text{Gy}}(\text{rectum})$ contributed to the summation of the penalty score. The respective results per single treatment plan on every sCT for the reference plan and the four adaptation approaches including the SD is displayed in Figure 3.9:

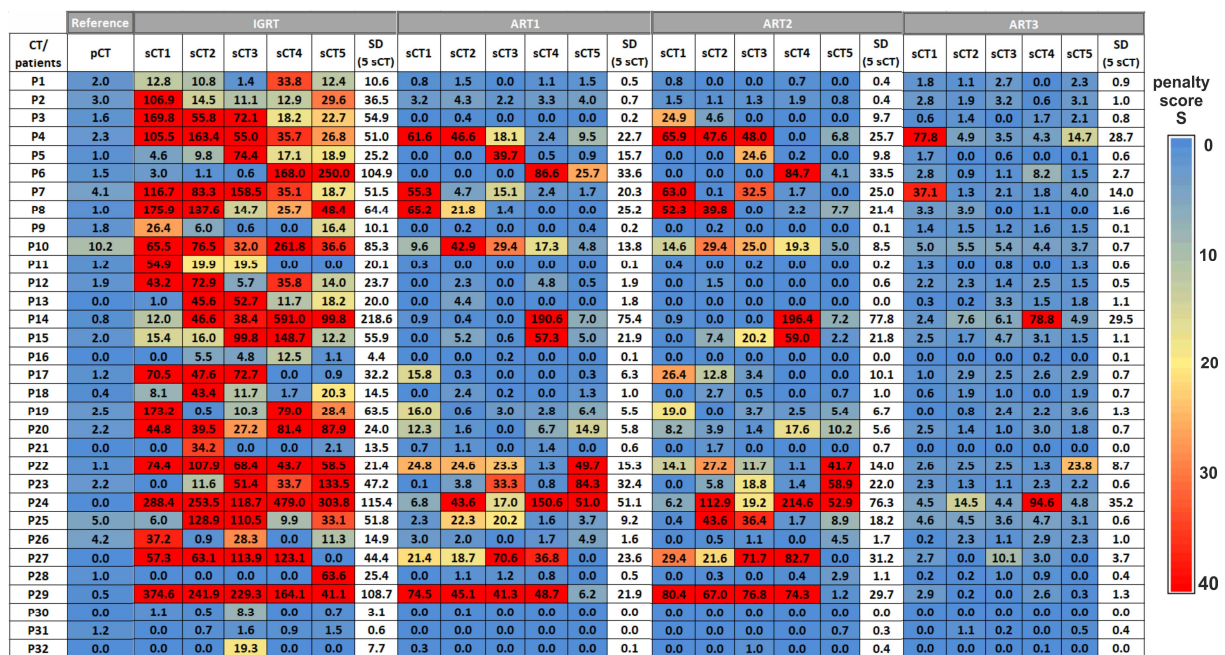


Figure 3.9: Distribution of the penalty score S including SD per treatment plan among the total patient population summed over four relevant PACE-C dose criteria for the four adaptation approaches IGRT, ART1, ART2 and ART3. Relevant dose criteria for the calculation of S were $V_{36.25\text{Gy}}(\text{PTV})$, $D_{98\%}(\text{PTV})$, $V_{37\text{Gy}}(\text{bladder})$, $V_{36\text{Gy}}(\text{rectum})$. The heatmap coloring denotes plans from having a score $S=0$ (blue) to scores $S>40$ (red).

Overall, the largest penalty scores could be identified for the IGRT approach, including the maximum value of all scores with $S=591$ (P14, sCT4). Only for patients P16, P30, P31 and P32 all five sCT achieved penalty scores below 20. The IGRT approach yielded the smallest amount of treatment plans having $S=0$ with 20. In contrast, 53, 64 and 31 treatment plans were obtained for the ART1, ART2 and ART3 approaches, respectively, that exhibited no violation of the four relevant dose-volume criteria. With respect to the ART1 and ART2 approaches, it became evident that four patients (P4, P24, P27 and P29) had at least 3 out of 5 daily treatment plans with $S>20$. Moreover, patients P4, P6, P14, P24, P27 and P29 exhibited comparable large SD within the IGRT, ART1 and ART2 approaches. Only four treatment plans of the ART3 collective possessed penalty scores of $S>35$ (P4, P7, P14 and P24). Although the reference plan of P10 had the largest penalty score of $S=10.2$ on the pCT, the ART3 approach

achieved a considerable reduction of violations through the other approaches to a maximum of $S=5.5$ among all five sCT. Moreover, the ART3 approach was the only adaptation technique being able to reduce the penalty scores of patients P27 and P29 below values of 11 and 3. The largest penalty score reductions through the three re-optimization approaches ART1, ART2 and ART3 averaged over all five sCT were identified for the patients P29, P24 and P14. In total, the number of treatment plans with violations of $S>40$ amounted to 62, 18, 20 and 3 for the IGRT, ART1, ART2 and ART3 approaches, respectively. It is noticeable that these larger penalty scores were rather concentrated on specific patients than randomly spread among the total patient collective, particularly with respect to the red-marked cells for the ART1 and ART2 approaches. Regarding the total penalty count per sCT, the obtained results are highest for the sCT4 throughout every adaptation approach. Besides the summation of S over single treatment plans, a summation per dose criterion over all 160 treatment plans per adaptation approach was performed which is shown in Figure 3.10.

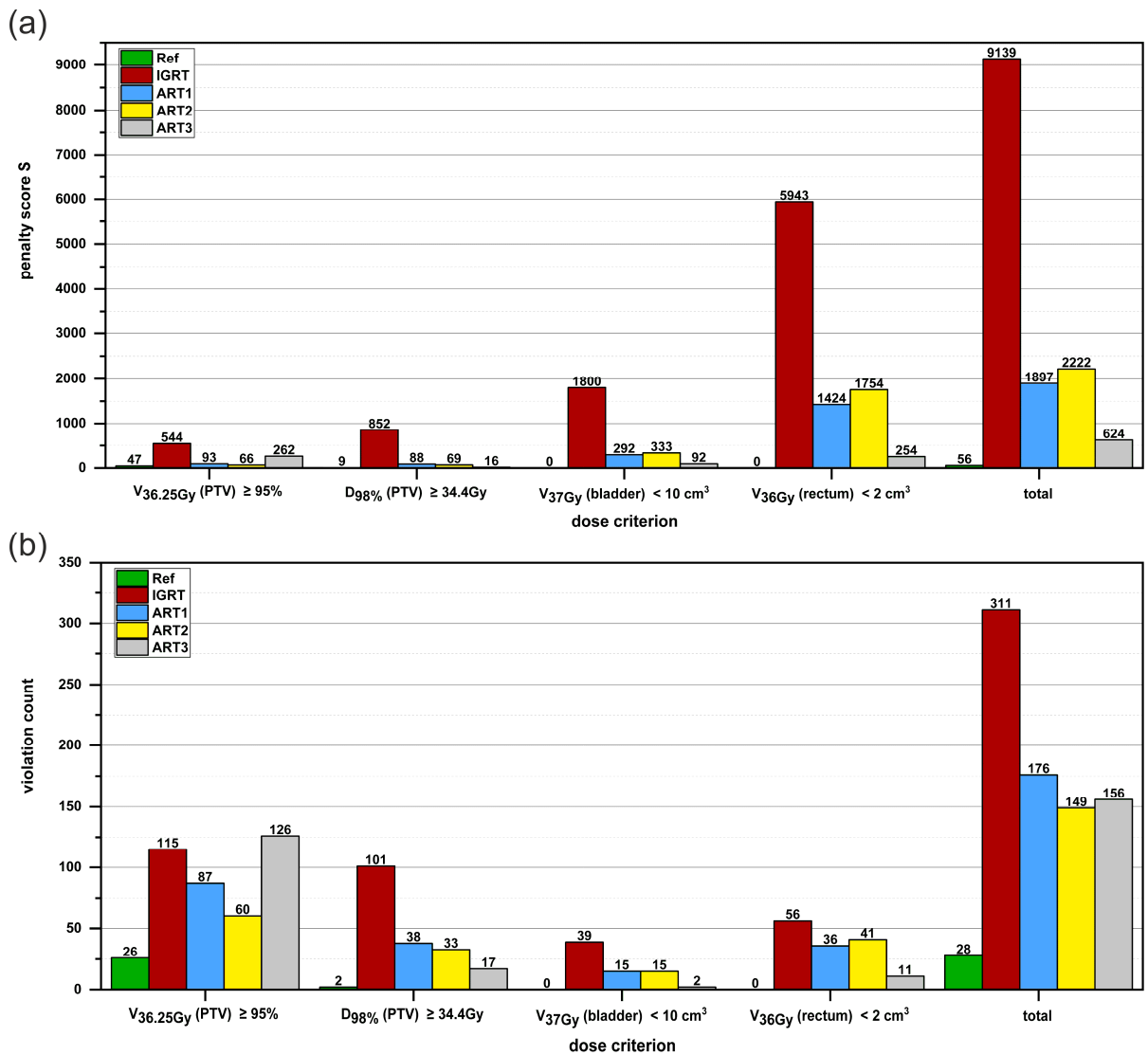


Figure 3.10: Summation of the penalty score S (panel (a)) and the violation count (panel (b)) over the total treatment plan collective separated for the four relevant dose criteria based on the PACE-C guidelines. Bar colors denote the adaptation approaches IGRT, ART1, ART2 and ART3. Bars on the right-handed end indicate the summation over the four dose criteria.

As expected, the IGRT approach yielded the largest penalty scores for all four criteria with the $V_{36\text{Gy}}(\text{rectum})$ criterion showing by far the highest violation with $S=5943$. The ART3 approach achieved the lowest results for S among all three re-optimization approaches except for the $V_{36.25\text{Gy}}(\text{PTV})$ criterion with $S=262$ where the ART2 approach had a score of only $S=66$. Overall, the total penalty scores of the ART1, ART2 and ART3 approaches were considerably lower than the total score of the IGRT approach, having percentage reductions of S by 79.2%, 75.7% and 93.2%, respectively. Whereas the ART1 and ART2 approaches gained a relative larger amount through improving PTV dose criteria (mean PTV/OAR reduction: 86.3%/79.9% and 89.9%/76.0%), the penalty reduction of the ART3 approach was more associated with less violations of OAR dose criteria of the bladder and rectum (mean PTV/OAR reduction: 75.0%/95.3%).

On the contrary, these PTV/OAR reductions were differently distributed for the secondly calculated pass/fail scoring system which simply counted all violations. Here, the ART1 approach achieved slightly more dosimetric goals through OAR sparing than through PTV coverage improvement. The difference between the PTV/OAR reductions was more explicit for the ART3 approach for the second scoring with 36.8%/87.6%. For the $V_{36.25\text{Gy}}(\text{PTV})$ criterion, the ART1 approach even had the largest count accumulated over all treatment plans with $S=126$. Overall, the ART2 approach achieved the smallest number of total violations with $S=149$. Similar to the penalty scoring, the IGRT approach exhibited the largest scores for all other three dose criteria. Regarding all four adaptation approaches of both quality scoring systems, proportionally largest values were obtained for the $V_{36\text{Gy}}(\text{rectum})$ for the penalty score whereas all results for the violation count of the $V_{36.25\text{Gy}}(\text{PTV})$ criterion constituted the largest proportion of the total penalty score.

3.2.3 Anatomical metrics and correlation with dose

Having portrayed the meaning of standard methods of treatment plan quality evaluation as well as the additional benefits generated by a penalty scoring system, the last chapter of this thesis focuses on the impact of anatomical metrics in terms of predicting potential overdosage prior to the actual replanning procedure of the day. Analyzing anatomical information gained through daily segmentation could help guiding the decision between different plan adaptation approaches and thus further accelerate the entire online ART workflow. Figure 3.11 contains the results of the bladder/rectum-PTV overlap volume for every single patient of the total collective of 32 patients averaged over the respective 5 sCT per patient.

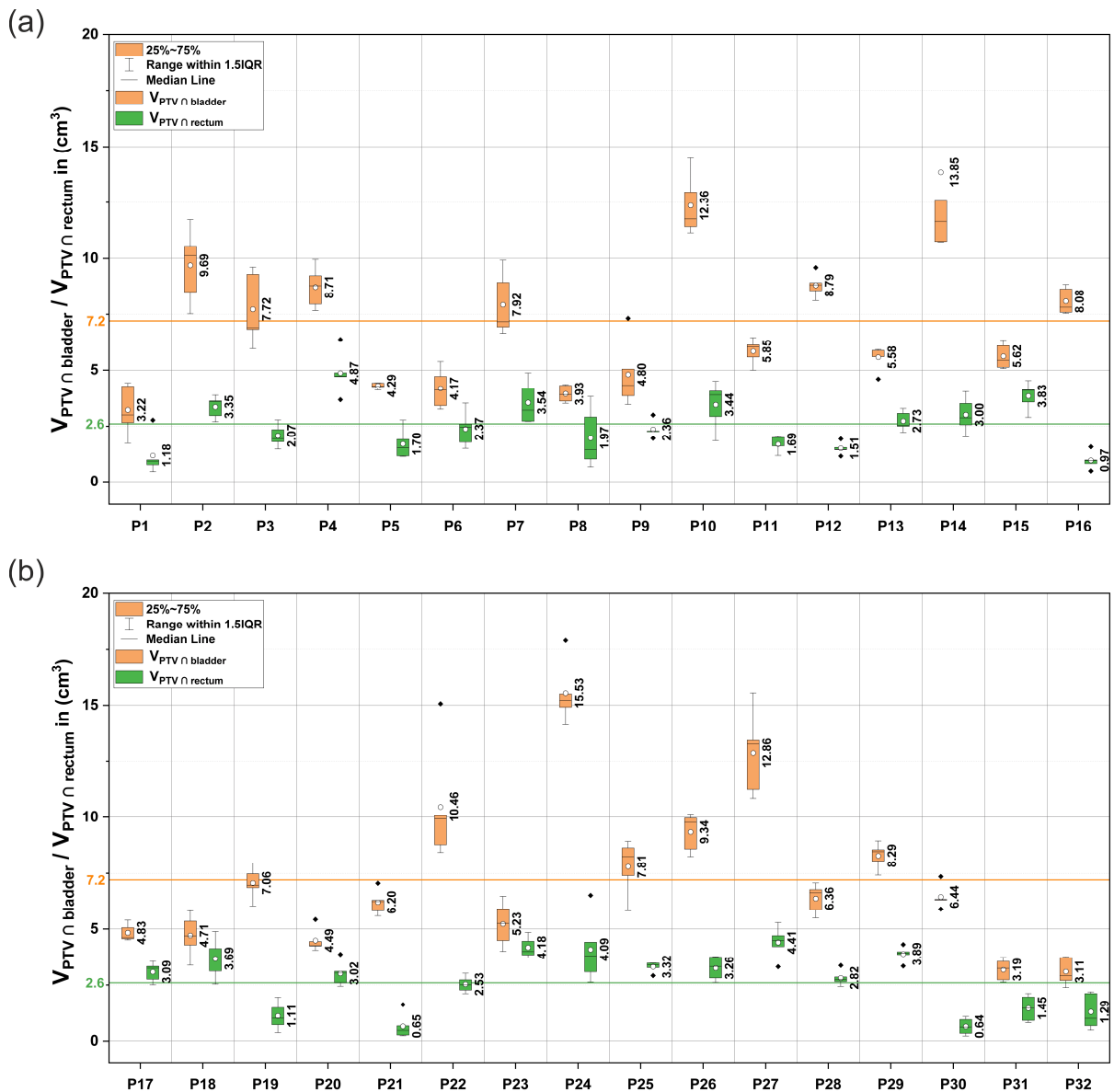


Figure 3.11: Overlap volume of the bladder (in orange) and the rectum (in green) with the PTV for Patients P1-P16 (panel (a)) and P17-32 (panel (b)). Boxplots denote the IQR and whiskers a range of 1.5IQR. Mean values of the two overlap volumes $V_{PTV \cap bladder}$ and $V_{PTV \cap rectum}$ were 7.2 cm^3 and 2.6 cm^3 , as indicated by reference lines.

Averaged over all five sCT of every 32 patients, the mean overlap volumes between the bladder and PTV " $V_{PTV \cap bladder}$ " and the rectum and PTV " $V_{PTV \cap rectum}$ " were $(7.2 \pm 3.4) \text{ cm}^3$ and $(2.6 \pm 1.3) \text{ cm}^3$, respectively. For the bladder, the analysis yielded largest results for patients P10, P14, P24 and P27 with overlap volumes of 12.36 cm^3 , 13.85 cm^3 , 15.53 cm^3 and 12.85 cm^3 . Patients P2, P3, P7 and P27 exhibited the largest IQR, indicating an over-average fluctuation within the five sCT. For the rectum, largest mean overlaps with the PTV were found for patients P4, P23, P24 and P27 with 4.87 cm^3 , 4.18 cm^3 , 4.09 cm^3 and 4.41 cm^3 . In total, the SD for the bladder was in the same range relative to its mean value with $(7.2 \pm 3.4) \text{ cm}^3$ compared to the rectum results of $(2.6 \pm 1.3) \text{ cm}^3$ which also showed a SD amounting to half of the actual mean value.

The Pearson's correlation coefficients between $V_{PTV \cap bladder}$ or $V_{PTV \cap rectum}$ and the total treatment plan penalty score S of the replanning approaches IGRT, ART1, ART2 and ART3 were determined to be 0.53, 0.49, 0.50, 0.46 or 0.47, 0.52, 0.55, 0.43, respectively. In order to anticipate potential OAR overdose by means of overlap volumes, the ratios between treatment plans exhibiting "close-to-tolerance" dose-volume parameters of $V_{37\text{Gy}}(\text{bladder}) > 9 \text{ cm}^3 / V_{36\text{Gy}}(\text{rectum}) > 1.5 \text{ cm}^3$ and over-average overlap volumes of bladder and rectum were determined for all four adaptation approaches. They amounted to 68.5%/69.1% for the IGRT approach and were found to be higher for the re-optimization approaches ART1, ART2 and ART3 with 100%/86.9%, 100%/90.1% and 100%/96.3%.

The results of the $V_{37\text{Gy}}(V_{PTV \cap bladder})$ and the $V_{36\text{Gy}}(V_{PTV \cap rectum})$ are displayed in Figure 7.4. It is recognizable that for both overlap volumes the mean value constitutes a large part of its related V_x value of the whole organ structure (shown in Figure 3.8). With respect to the reference plan, the IGRT, ART1, ART2 and ART3 approaches, this ratio amounted up to 94.1%, 63.4%, 80.2%, 81.7% and 90.3% or to 94.7%, 68.7%, 94.2%, 94.2% and 90.4% for the bladder and rectum, respectively. Thus, for all the re-optimization approaches, mean overdose to the relevant OAR can be located in the overlap region with the PTV. This observation is not valid for the IGRT approach. Mean results of $V_{37\text{Gy}}(V_{PTV \cap bladder})$ and $V_{36\text{Gy}}(V_{PTV \cap rectum})$ are substantially higher (bladder) and show a different distribution of IQR as well as outliers (rectum) compared to the results identified for the re-optimization approaches ART1-ART3. Consequently, substantial parts of the total overdose in this approach are located outside of the overlap region. Moreover, the mean values for the IGRT approach are very close to the results of the re-optimization approaches for both organ structures.

Figure 3.12 shows the DVH for the two overlap volumes $V_{PTV \cap bladder}$ and $V_{PTV \cap rectum}$. In contrast to Figure 3.7 which displayed the DVH of the total bladder and rectum volume, the differences between the IGRT and re-optimization approaches in the high dose region of the overlap volume become more evident. With a mean volume SD of 11.17% for the rectum overlap volume the hereby presented IGRT results have a comparably larger spread than the related aforementioned results of the total rectum with 5.35%.

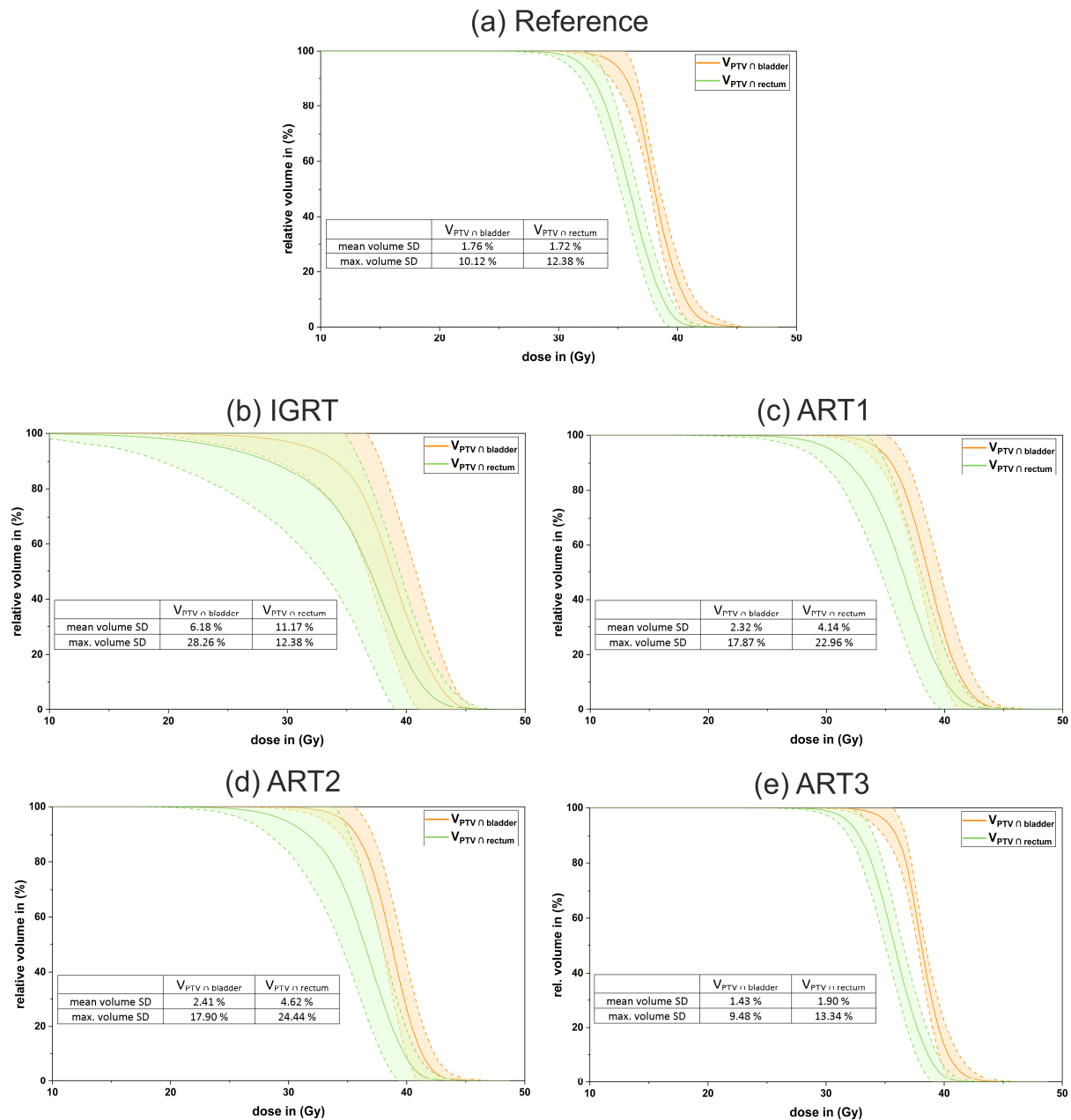


Figure 3.12: Mean dose-volume histogram of the $V_{PTV \cap bladder}$ and $V_{PTV \cap rectum}$ for the reference plans and the four adaptation approaches IGRT, ART1, ART2 and ART3. Light colored ribbons represent the point-wise volume SD among a collective of 160 plans per treatment planning approach. Prescription doses were $D(CTV)=40$ Gy and $D(PTV)=36.25$ Gy. Mean and maximum volume SD are also shown for both overlap-volumes of all five treatment plan collectives.

On the contrary, the SD of the bladder amounted to 6.18% for the overlap volume with the PTV, therefore being smaller than the result for the total bladder of SD=7.87%. The IGRT approach yielded the largest maximum SD for the bladder with 28.26% within all four adaptation approaches. With regard to the re-optimization approaches, both ART1 and ART2 treatment plans were not able to restore the small SD of the reference plan. For the $V_{PTV \cap \text{rectum}}$, mean volume SD were more than twice as high as for the reference (4.14%/4.64% vs. 1.72%). The ART3 approach achieved even smaller variations for the bladder PTV overlap with SD=1.43% and showed a small SD for the $V_{PTV \cap \text{rectum}}$ dose of 1.90% being close to the reference result. Likewise, the ART3 approach exhibited the smallest overall maximum SD with 9.48% for the $V_{PTV \cap \text{bladder}}$.

In order to compare the ability of overdose prediction between the clinically rather uncommon overlap volume and the comparably often used DSC, single values for every patient, Pearson correlations with the penalty score and overdose coincidences were additionally obtained for the DSC of the bladder and rectum. The results of the DSC, calculated between each sCT and the reference pCT, are displayed in Figure 7.5 in the appendix. Mean DSC were $(87.7 \pm 4.5)\%$, $(77.1 \pm 10.8)\%$ and $(76.2 \pm 6.2)\%$ for the CTV, bladder and rectum, respectively. Least congruence between organ structures of the CTV were identified for patients P8 and P20 (DSC=0.79). P20 also exhibited a comparably low DSC with 0.64 for the bladder, together with lowest obtained DSC of patients P13 (0.64) and P32 (0.52). Concerning the rectum, smallest results were found for patients P12, P19 and P24 with a mean DSC of 0.71. Largest SD within the five sCT per patient were detected for P6 (0.07), P23 (0.17) and P14 (0.11) for the CTV, bladder and rectum, respectively.

The Pearson's correlation coefficients between the DSC(bladder) or the DSC(rectum) and the total treatment plan penalty score S of the replanning approaches IGRT, ART1, ART2 and ART3 were 0.057, 0.068, 0.086, 0.078 or -0.061, -0.112, -0.078, -0.084, respectively. Similar to the prediction amount of potential overdose to the OAR obtained by the PTV overlap volumes, the ratios between treatment plans showing "close-to-tolerance" results of $V_{37\text{Gy}}(\text{bladder}) > 9 \text{ cm}^3 / V_{36\text{Gy}}(\text{rectum}) > 1.5 \text{ cm}^3$ and over-average DSC of bladder ($>77.1\%$) and rectum ($>76.2\%$) were calculated. The analysis yielded ratios of 55.6%/58.0%, 57.1%/54.1%, 54.2%/54.6% and 66.7%/59.3% for the IGRT, ART1, ART2 and ART3 approaches, respectively. Thus, these ratios were 12.9%/11.1%, 42.9%/32.8%, 45.8%/36.7% and 33.3%/37.0% lower than the related ratios of the overlap volumes for the rectum and bladder.

3.2.4 Treatment planning time

A short time for the re-optimization and dose calculation of a modified treatment plan constitutes an integral part for a feasible daily ART process as it must be performed while the patient remains on the treatment couch. Table 3.3 displays the total treatment plan generation times for all treatment plans calculated according to the PACE-C treatment planning guidelines. Since time is of crucial relevance for the clinical realization of adaptive warm start techniques, all plan calculations were also performed with a larger grid size of 3 mm. The statistical uncertainty remained at 1% for both the 3 mm and 2 mm calculation grids.

Table 3.3: Mean treatment plan generation times for a calculation grid of 2 mm and 3 mm including respective standard deviations. Reference plans were calculated on the planning CT (pCT) with a slice thickness of 2 mm (3 mm grid) and 1 mm (2 mm grid). Adapted treatment plans were calculated on the sCT with a slice thickness of 2 mm (3 mm & 2 mm grid).

total treatment plan generation time (min) per approach					
calculation grid (mm)	reference on pCT	IGRT on sCT	ART1 on sCT	ART2 on sCT	ART3 on sCT
3	9.7 ± 2.3	0.8 ± 0.1	0.9 ± 0.1	4.8 ± 1.9	6.7 ± 1.7
2	31.5 ± 4.8	2.5 ± 0.3	2.6 ± 0.3	12.1 ± 3.2	19.4 ± 4.0

The generation of a treatment plan on the pCT took on average 9.7 min (3 mm grid) and 31.5 min (2 mm grid). The IGRT and ART1 approaches achieved the fastest calculation times with below 1 min (3 mm grid) and 3 min (2 mm grid). Total generation times of over 4.9/6.7 min (3 mm grid) and 12.1/19.4 min (3 mm grid) were obtained for the ART2/ART3 approaches, respectively, which is directly related to the additionally performed segment adaptation. A full re-optimization from scratch was performed for the ART3 approach with identical IMRT constraints and took a mean of 6.7 min and 19.4 min, respectively. The SD was higher for plans with increased degrees of freedom during the re-optimization, rising from the ART1 to a maximum for the ART3 approach. Single patients showing comparable large variation of the daily anatomy resulted in larger segment modifications and thus required longest calculation times. With respect to its three-dimensional characteristics, the saving of time caused by a grid increase from 2 mm to 3 mm within the Monte Carlo-based dose calculation can be estimated as $3^3/2^3=3.4$. This factor roughly applies to the relation between the obtained calculation times with 3.2, 3.1, 2.9, 2.5 and 2.9 for the reference plan and the IGRT, ART1, ART2 and ART3 approaches, respectively.

4 DISCUSSION

Due to technological progress regarding deep learning application, the increasing complexity of treatment plans for prostate cancer patients and the development towards UHF regimens (higher doses delivered in less treatment fractions), daily RT demands for improved accuracy during every workflow step which potentially leads to the clinical implementation of more and more offline as well as online ART procedures. Insufficient image quality of daily acquired images and the feasibility of actual plan modification methods pose the major challenge on the way towards an efficient realization of CBCT-based ART procedures in clinical routine, not only for the pelvic body site. Consequently, this research study focused on the analysis of the following six core aspects with the aim of developing an efficient and simultaneously robust ART workflow:

- (1) Improvement of daily image quality via generation of synthetic CBCT (sCT)
- (2) Segmentation accuracy on daily sCT
- (3) Dosimetric accuracy on daily sCT
- (4) Dosimetric benefits of certain ART approaches over IGRT
- (5) Dosimetric correlations with anatomical properties
- (6) Feasibility and guidance for daily treatment plan adaptation

In the following, these aspects are discussed in terms of the general validation of the novel cycle-GAN based sCT model of the pelvis (points (1)-(3)) and in terms of actual plan adaptation within the framework of a UHF prostate SBRT (points (4)-(6)).

4.1 Evaluation of sCT

The generation and validation of a fast and reliable correction of daily acquired CBCT represented the first major goal in this work. Every subsequent workflow step in a potential adaptive treatment is compromised if the imaging of the patient's daily anatomy is not displayed accurately enough. Corrected CBCT have the potential to enhance the daily IGRT procedure based on positioning the patients in translational and rotational degrees. Moreover, following segmentation of relevant organ structures and HU-ED-assignments for dose calculation or treatment plan modifications strictly rely on a robust image of the day.

In spite of the superior soft tissue contrast of MRI, also used at the recently introduced MR linac, the potential of enhanced CBCT at C-arm linacs should not be undervalued. Being present for more than 15 years¹³⁹, proven to have the least mitigating impact on plan quality¹⁴⁰ and, for example, enabling the reduction of safety margins together with SBRT techniques at conventional linacs¹⁴¹, kV-CBCT-imaging represent a robust alternative to MR-guided RT; not least because C-arm linacs offer a higher cost efficiency (staff, maintenance, treatment time, etc.) and are widely available.

4.1.1 Image quality

Adequate image quality combined with a sufficient FOV of daily acquired images constitute the most relevant prerequisite for a reliable and fast adaptive workflow that is being daily performed with the patient lying on the treatment couch. Apart from the comparably long history of correction approaches of CBCT image quality with density overrides or methods of DIR over the last decades, the approach of using deep learning for image enhancement has undoubtedly proven its dominance in the last couple of years⁵¹. Thus, a cycle-GAN-based algorithm for sCT generation was investigated in this thesis with a focus on image quality, robustness and clinical feasibility.

With the presented evaluation of 15 prostate cancer patients it was demonstrated that the ADMIRE cycle-GAN algorithm allows for a sCT generation solely on the basis of daily acquired kV-CBCT. Visually, the application of the pelvic sCT model yielded an improved contrast, corrected intensity non-uniformities and removed scatter-induced artifacts, resulting in an overall image quality close to the reference pCT. Based on the results obtained by investigating the IVH of the body contour VOI for all three involved image types, the sCT IVH achieved a CT number distribution being very close to the reference pCT throughout every evaluated pelvis patient as shown in Figure 7.1. Highest deviations were detected for the second maximum of the IVH at approximately 40 HU with an average volume difference between the pCT and sCT of nearly 60 cm³, compared to the first maximum showing a discrepancy of 35 cm³ at nearly -100 HU. These regions of CT numbers are assigned to soft tissue and fat⁶ and clearly substantiate the observation of an improvable soft tissue contrast in the central region around the prostate even after the sCT generation. Although the sCT managed to substantially improve the obtained image quality, missing image information, for example in low contrast areas, cannot be created without prior information. This issue could be targeted with an enhanced CBCT detector that physically removes scatter by means of, for example, an anti-scatter-grid³⁹. Furthermore, 6 of the 15 patients showed an additional peak of the IVH around 0 HU which is assigned to EDs of water and body fluids, mostly pronounced in the pCT. This can be related to the patients' bladder volume and their proportion of the total CBCT body VOI. All 6 patients exhibited large bladder volumes of at least 390 cm³ which led to an additional water-related maximum in the IVH given that the surrounding CT number spreads of soft tissue- and fat-related maxima were sufficiently apart from each other.

With regard to the determined ME/MAE of the sCT in Figure 3.2, most robust results in contrast to the related values of the CBCT were obtained for the body contour VOI with 5.4 HU/41.8 HU. Together with the values of the soft tissue, the results were also smallest in comparison to the findings for the other two ADMIRE sCT models for the thorax and H&N body site presented in reference¹²³. This is clearly correlated to the larger training cohort of the pelvis model with 205 patients spread across 7 different departments being employed for training the GAN. The presented results are in good

agreement with recent related research that reported similar values for the ME/MAE of the total body contour VOI with $-3\text{ HU}/16.1\text{ HU}^{53}$ and $-6\text{ HU}/87\text{ HU}^{142}$. Another study using deformed pCT as ground truth obtained mean HU values for the prostate and bladder of 19 HU and 4 HU for cycle-GAN-based sCT¹²¹. Apart from utilized GAN algorithms, mean MAE results for U-net- and CNN-based sCT generation of 51-88 HU¹⁴³ and 40.5 HU¹⁴⁴ were presented for CBCT and MRI, respectively, for the total body contour VOI, being very close to our obtained findings. Nonetheless, a robust comparison of our results to the related literature can only be performed with some tolerance as each cited study showed variations in terms patient collectives for training and testing, acquisition parameters for daily imaging, the specific architecture of the deep learning algorithm (GAN, DCNN, U-net...) and its training procedure as well as investigated VOIs of the image analysis. Regarding particular VOIs, only one other study was available that analyzed a separate bone VOI of sCT created with a CNN based on MRI¹⁴⁴ and reported a slightly higher MAE of 159.7 HU compared to our presented value of 118.5 HU.

The CBCT-to-sCT conversion took on average 30 s which is slightly slower compared to conversion times of below 10 s reported by related using cycle-GANs^{121,142}. Further acceleration of this process could be achieved through an application of a refined GAN algorithm or improved hardware components. Thummerer et al. stated that through pre-registrations and combination with analytical image-based corrections, the sCT generation time could be further optimized to only a few seconds¹⁴⁵. Three other sCT studies^{52,54,111} already accomplished this very fast sCT generation. However, it should not be neglected that the presented sCT approach of this thesis has the advantage of being implemented in the TPS and results in sCT that are already registered to the reference pCT.

4.1.2 Segmentation accuracy

The workflow step of image segmentation, respectively, is directly related to the underlying image quality and has a great impact on the subsequent decision of adapting the daily delivered treatment plan. Furthermore, the definition of organ structures usually takes several minutes and therefore often poses the most time-consuming step in an entire ART workflow. The analysis of the ADMIRE DIR-based, automatically performed segmentation on the sCT revealed that, among all four investigated organ structures, the bladder achieved the best results for the DSC (90.5%), SEN (88.1%) and SPEC (95.8%). This arises from the general good contrast of the bladder in comparison to its surrounding tissue, except for the intersection with the prostate. Moreover, the ADMIRE DIR algorithm contains a specifically trained term for bladder refinement, including a deformable surface model that is additionally trained to manage comparable large change deformations of this organ. However, the bladder exhibited the largest HD (15.3 mm) and d_{mean} (2.7 mm) of all four organs which could be mainly identified in the cranial region due to substantial filling deviations compared

to the anatomy of the pCT, making it more difficult to create a robust deformation field, or at the overlap with the prostate. Such larger displacements only have a small influence on the general concordance between the manually and automatically generated bladder structures as this organ has the largest size of all four evaluated organs.

In contrast, a small change in shape definition has a great influence on the DSC for the SV due to their small size which is reflected in the smallest of all obtained DSC with 66.7%. In combination with a lower soft tissue contrast and the general high inter-observer variability, also being valid for the prostate¹⁴⁶, this organ is without doubt the most difficult one for auto-segmentation algorithms within the entire pelvic body site. In general, a direct comparison to similar references remains difficult due to varying methods of imaging (pCT, CBCT, MRI and sCT), architectures of applied DIR- or DL-based segmentation algorithms and definitions of ground truths (deformed, manual or DL-based contour sets on the pCT, MRI or same image type). A research study about DL-based auto-segmentation on synthetic MRI presented DSC of 95%, 89% and 92% for the bladder, prostate and rectum, respectively¹⁴⁷. These values are better than our findings since DL approaches in combination with MRI can be regarded as the current gold standard in segmentation accuracy on account of the individual training of the auto segmentation and the superior soft tissue contrast of the MRI. Other related research using DIR-based segmentation on CT or CBCT presented DSC values for the bladder/prostate/rectum/SV of 81.9/81.5/78.2/--%¹⁴⁸, 87/82/-/--%¹⁴⁹ and approximately 80/80/<80/50%¹⁵⁰. These are slightly inferior to our identified DSC of 90.5/85.9/81.0/66.7% and could originate from the enhanced image quality of the sCT in contrast to CBCT. The study of Schreier et al.¹⁵¹ reported better congruence between the manual and DCNN-based contours of 93.2/84/87.1/70.1% for the bladder/prostate/rectum/SV which is mostly related to the large training size of the employed neural network. Besides, localizations of maximum deviations between auto-segmentation and manual delineation was determined to be in the inferior and superior region for the prostate^{146,152,153} as well as in the anterior / right-left direction of the SV¹⁴⁶ which corresponds well to our findings.

With the SEN being on average lower than the SPEC for each body site, the ADMIRE segmentation algorithm tends to identify more voxels inside the manual reference contour as false negatives while at the same only creating a small amount of false positives outside the manual reference contour. Consequently, the automatically generated contours are in general smaller than the manual reference contours. To sum up, largest discrepancies between the manual and DIR-based organ structures occurred on account of insufficient contrast at organ interfaces of the bladder, rectum and prostate on the sCT, of larger displacements between the pCT and sCT as well as of appearing/disappearing voxels such as rectal gas or displacements of the SV and small bowel close to the bladder¹⁴⁸ (as presented in Figure 3.3, panel (c)).

Regarding the essential aspect of performance speed, the ADMIRE intra-patient segmentation module provided a segmentation of the entire pelvic structure set within 30 s which was followed by a manual correction taking on average (5.2±1.6) min. This

resulted in a maximum of 8 min for achieving a complete segmentation of a daily sCT. With respect to other presented, automated segmentation times in the current literature of around 30 s^{58,147,149} this workflow step showed an acceptable performance but still can be further accelerated by means of further enhanced daily images or a combination with an individually trained atlas-based segmentation module. Brion et al.¹⁵⁴ and Liang et al.¹⁵³ demonstrated very fast segmentation times of a few seconds which could be realized by combining methods of data augmentation and parallel computing with a robust neural network.

Further improvements could be achieved by a general enhancement of CBCT quality (as suggested in the first section 4.1.1), an implementation of a department-specific DIR algorithm or an atlas-based approach and a stricter organ preparation protocol to avoid varying organ filling or rectal flatus at all. Large-scale studies on automatic segmentation in the pelvic region have suggested that model-based segmentation yet was able to outperform DIR and other approaches with regards to precision, robustness and required time^{55,155}. Moreover, deep learning-based approaches of image segmentation are on the rise due to their ability of being custom-tailored to individual contouring conditions and fast performance⁵⁵. Thus, it is likely to expect a fundamental conversion in the field of auto segmentation, although the manual inspection and QA of automatically performed segmentation remains indispensable and most time consuming in contrast to automatic image synthesis. Required timeframes for editing automatically generated contours are still located in the range of several minutes¹⁵⁶ or reduced the complete segmentation time by merely 30%¹⁵⁷. On top of that, and although still being recommended by the AAPM report on DIR QA⁴¹, recently developed metrics such as the surface Dice coefficient^{158,159} or an evaluation based on quality scores^{138,151} are more and more replacing established metrics such as the DSC or HD due to their ability to better locate inaccuracies and better correlation with the required time for manual correction.

4.1.3 Dosimetric accuracy

The accuracy of the calculated daily dose constitutes the third essential treatment component in a daily performed adaptive workflow. This is mainly influenced by the remaining image uncertainties of the sCT as well as by the elapsed time during all adaptation procedures until the actual treatment plan delivery. Moreover, a fast recalculation of the initial treatment plan on the anatomy of the day could trigger further modifications to the plan segments for the same or next treatment fraction.

With respect to specific dose-volume criteria shown in Figure 3.4, the deviations between the sCT and pCT were comparably small with all obtained IQR staying well within a range of $\pm 1.5\%$ and $\pm 1.0\%$ for the target volume and the OAR bladder and rectum, respectively. Similar to aforementioned varying characteristics of previously conducted research on sCT only an indirect comparison to our findings can be performed at this point. Furthermore, a large proportion of published studies on CBCT-

based sCT generation rather focused on image quality metrics, scarcely complementing the results with further dose analysis. Kurz et al. reported an absolute dose difference of -1 Gy to 0 Gy for the D_{98} , D_{50} and D_2 of the target volumes and a comparable dose difference range for dose-volume parameters of both rectum and bladder¹⁴². However, it has to be stated that in this case two identical anatomies were compared whereas our findings contained an anatomic discrepancy between the pCT and sCT as well. Furthermore, a tendency of slight dose overestimation could be observed for the presented dose deviations which could have originated from the larger CT numbers expressed by the positive ME. Another study on GAN-based synthetic MRI achieved smaller deviations between the pCT and synthetic image of maximum - 0.5%¹¹⁴ which could originate from the enhanced soft tissue contrast of MRI over CBCT.

Yet the presented approach of cycle-GAN-based sCT generation achieved much higher dosimetric precision in contrast to alternative strategies (presented in a recent review³⁷) that either improved Elekta XVI-based CBCT by application of CT-specific calibration curves and shading corrections with percentage deviations of $D_{\text{mean}}(\text{PTV})=7.5\%$ (in Alderson phantom $D_{\text{mean}}=4.7\%$)¹⁶⁰ or with CBCT-specific calibration curves having deviations of $D_{\text{median}}(\text{PTV})=-2.0\%$ in the Catphan phantom³⁸. Moreover, the last research group also made use of population-based HU override techniques with differences of $D_{\text{median}}(\text{PTV})=1.9\%$ that are in the same range of dose differences of $D_{\text{mean}}(\text{PTV})=-2.8\%$ determined with patient-specified HU calibration curves³⁵. Dunlop et al. achieved a deviation of $D_{\text{mean}}(\text{CTV})=0.8\%$ but also worked with a different planning system using a collapsed-cone dose calculation algorithm instead of Monte Carlo based dose calculations¹⁶¹. Related research using an anti-scatter grid or a combination of override techniques together with DIR methods presented deviations of min. 1.2%³⁹ in the CIRS phantom or of $D_{\text{mean}}(\text{PTV})=0.8\%$ using the Varian on-board imager system¹⁶². On top of that, all aforementioned studies investigated less than 15 patients.

The evaluation of different pass rates for common gamma criteria (GPR) as well as for dose differences (DDR) resulted in values being over the clinical threshold of 95% and a low SD for the GPR of maximum 2.2%, whereas the DDR exhibited comparably higher SD of maximum 9.3% for a related 2% dose threshold. Both GPR and DDR increased with rising low dose thresholds which implies that most of the dose differences were located in low dose regions instead of high dose regions. Based on the comparison between the DDR criteria of point-wise difference of <1%, <2% and <3%, a large proportion of discrepancies between the sCT and pCT could be identified for <1% since at least approximately 80% of all dose points passed the 2% criterion for all three investigated thresholds. These findings are consistent with the spatial distributions of the three exemplary dose difference maps displayed in Figure 3.5 since highest differences were located in low dose areas at the patient outline or in the superior-inferior periphery of the GTV. The central high dose region of the prostate

either showed scattered dosimetric deviations or uniformly distributed low dose differences. This reinforces the robustness of the pelvic sCT model, also with regard to the other two body sites of HN and thorax that were subject to single dosimetric outliers in spite of having a better DDR or GPR over 95%¹²³. Our findings for the GPR are in agreement with the results reported by Kurz et al.¹⁴² of 96% (2%/2mm) and 100% (3%/3mm criterion) while our DDR stayed below the presented results of 100% of the same study. However, the related publications made use of a different GAN architecture and more importantly, performed all VMAT plan calculations with a collapsed-cone algorithm that complicates a direct comparison. Another study¹⁴³ published better results with mean GPR (2%/2mm) and DDR (<2%) of minimum 99.5% but employed a U-net training for sCT generation and, contrary to our study, compared the daily dose to the same underlying anatomy by means of corrected CBCT as ground truth. Similarly, Hansen et al.⁵⁴ reported superior DDR of 100% (<2%) and 90% (<1%) for VMAT plans on intensity-corrected CBCT corrected with a CNN approach.

In general, literature on image conversion for pelvic CBCT is scarce since MRI applications and related synthetic images started to dominate the scientific field in the past couple of years, particularly alongside the introduction of the MR linac^{51,144,163,164}. Nevertheless, CBCT applications remain attractive for reasons of wider distribution, faster treatment times (average prostate treatment on MR linac: 45 min¹⁶⁴) and recent developments of improved detectors as well image enhancement algorithms with deep learning. Based on our analysis of the ADMIRE cycle-GAN sCT generation in the pelvic body site, it was feasible and quantitatively accurate to perform an entire adaptive treatment process in the research environment of an established TPS. All of the obtained results for imaging, segmentation and dose calculations were well within standard clinical thresholds or able to compete with current alternative approaches. The general validation of the novel cycle-GAN-based sCT generation method for the pelvic body site provided an image quality close to the reference pCT with mean MAE and ME of 0.5 HU and 24.4 HU for the most relevant VOI of the pelvic soft tissue. Similar to the sCT generation time, image segmentation was available within (30±5) s and showed good results in comparison to related DIR-based studies on pelvic segmentation, exhibiting a range between 90.5% and 66.7% for the DSC. The obtained dosimetric precision of specific target/OAR parameters of ±1.5% / ±1.0% was in line with related and most commonly obtained DD thresholds of <1% identified by Spadea et al.⁵¹. Moreover, GPR of 99.9 ± 0.1 (3%/3mm criterion) and 98.5 ± 1.7 (2%/2mm criterion) between the sCT and pCT demonstrated satisfying and robust results above the established clinical threshold of 95%. Thus, the presented pelvic sCT model can be regarded as accurate enough for daily adaptation procedures including image segmentation and dose calculation.

In spite of these promising results, the eventual realization in clinical routine demands for further acceleration since accomplished benefits through adaptation decrease the longer the patient remains on the treatment couch until the actual plan delivery. Image segmentation and subsequent manual contour editing have the most potential for additional time reduction by improving involved DIR algorithms for example with

weightings for prioritized pelvic regions, extending patient preparation and drinking protocols to minimize anatomical variations or including protocol guidelines with certain threshold values in clinical routine. This widespread issue of missing standardization also applies to the steps of image synthesis and dosimetric accuracy since a fast and desirably automated adaptive workflow demands for interruptions every time when a threshold parameter is exceeded. It has to be noted though that the research field of deep learning is comparably young with first applications on CBCT being published around 2017⁵¹ and still needs time, much more evaluated patient data, dedicated QA procedures, larger FOV for body sites like thorax or H&N and support from vendors in order to be finally realized in daily RT treatments. Improved neural networks are constantly being developed, for example by integrating attention gating¹⁶⁵ or transfer learning¹⁶⁶ that enable better processing of varying regions (rectum or bowel) or exceptional anatomies. Nonetheless, with this general validation of the pelvic sCT model a crucial step towards the clinical implementation of ART on CBCT-based C-arm linacs was made which will be further complemented by actual plan adaptation techniques presented in the next section.

4.2 Evaluation of adaptive treatment planning approaches

Based on the validation of the cycle-GAN-based pelvic sCT model including successfully performed CBCT conversion and DIR-based image segmentation, the analysis of different treatment plan modification methods constitutes the next pending issue that needs to be solved in the chronological order of a daily adaptive workflow. As explained in Figure 1.1, largely deformed organ structures or inadequate recalculated dose distributions on the daily anatomy can cause the re-optimization of the initial treatment plan with different degrees of freedom. Therefore and with a focus on robustness and time efficiency, the second part of this thesis aimed for the evaluation of dosimetric benefits of different ART approaches (ART1, ART2, ART3) over conventional IGRT based on standard and additional treatment plan analysis methods. Moreover, anatomic properties were assessed in order to develop guidance for dose prediction and guide the daily decision of when to apply which adaptation strategy. The treatment regimen and planning guidelines including dosimetric criteria of the UHF PACE-C trial for prostate SBRT served as a basis for the entire evaluation of adaptive replanning strategies on synthetic CBCT, referring to and expanding on the work previously published¹²⁹.

4.2.1 Standard treatment plan evaluation methods

In order to compare the four replanning approaches of IGRT, SAM-based ART1 and ART2 as well as the full re-optimization ART3 different standard methods of treatment plan evaluation were used. Exemplary dose difference maps (Figure 3.6), mean DVH including point-wise SD (Figure 3.7) and specific, dose-forming dose-volume criteria

given by the PACE-C guidelines (Figure 3.8) helped to figure out dosimetric differences between the four replanning approaches with clinically established evaluation methods.

Regarding the conventional IGRT approach, overdoses to the OAR close to the PTV prescription dose of 36.25 Gy and, as expected, an incapability of covering the CTV together with the small 4 mm-margin of the PTV in a conformal way could be identified. The dose difference maps also showed that with an IGRT-based delivery doses above 20 Gy would have been delivered to surrounding healthy tissue. Furthermore, the analysis of the mean DVH revealed the highest SD among all four replanning approaches with 7.87/5.35% for the bladder/rectum volumes, particularly in the overlap region of both OAR and the two target volumes. Regarding the CTV and PTV, differences between the obtained SD of all four replanning approaches were not that distinct but again revealed the IGRT approach to have largest variations with mean volume SD of 1.12% and 1.43%, respectively (see Figure 3.7).

These general findings were reinforced by the results obtained through the specific dose criteria. The IGRT approach exhibited the highest variation with most identified outliers for every dose-volume parameter. Mean values of the criteria $D_{98\%}(PTV) \geq 34.4$ Gy and $V_{36Gy}(\text{rectum}) \leq 2$ cm³ were 32.9 Gy and 2.01 cm³, respectively, and thus even located beyond the given threshold value of the PACE-C guidelines with largest IQR of 3.0 Gy and 2.29 cm³. This implies that translational and rotational correction of standard image guidance cannot compensate for daily anatomical deformations of either target or OAR structures as well as varying organ fillings as it has been previously stated in the literature^{167,168}. Even though the evaluated setup of IGRT was based on daily kV CBCT-imaging and thus eliminated a major proportion of anatomical variations, additional techniques of image guidance were not implemented that could have further improved the dosimetric accuracy of the presented IGRT approach. For example, patient monitoring by means of fiducial markers is highly recommended by the PACE-C guidelines which could have increased the robustness of the daily matching process between the CBCT and pCT, consequently reducing the time for image registration and potential manual corrections of automated segmentation. As presented by Winkel et al., two major reasons for treatment plan adaption have to be considered separately from each other: Positional changes or a deformed shape of the daily patient's anatomy¹⁰. With regard to positional changes, adaptive replanning can be applied although it is not entirely necessary. Already marker-based IGRT can account for any deviations in the three degrees of freedom of translations or rotations in a comparably faster way than plan adaptation and without further need of additional software for plan generation and QA¹⁶⁹. On the contrary, this technique is not able to correct for noteworthy deformations or any large filling discrepancy of the bladder and rectum which would leave an adaptation of the initial treatment plan as the only viable solution.

But even for this scenario, methods such as rectal spacers⁸⁸, rectal balloons¹⁷⁰ or strict drinking protocols for achieving similar daily bladder fillings¹⁷¹ have proven to be robust alternatives to daily ART techniques. At the end, the choice between strict patient

preparation or application of daily ART methods depend on the individual expertise of the RT department and the specific conditions of the patients' treatment site. While ART is in general more comfortable for the patient in contrast to sometimes invasive preparations with, for instance, marker implantations, it also requires more skilled personnel and additional QA prior to the treatment. Once the relevant technology, software and capacity is robustly available, ART procedures might be easier to implement in clinical routine, in particular for hypofractionated treatments with a low number of fractions. The aforementioned techniques of motion mitigation and fiducial markers can substantially enhance the fast SAM-based adaptation approaches like ART1 and ART2 with regard to reduced optimization times and dosimetric robustness whereas additional, clinically relevant dosimetric benefits might fail to be realized through combination with a full re-optimization (ART3 approach).

The obtained results of the proposed re-optimization approaches implied that already a SAM-based replanning with a weight modification (ART1) can gain additional dosimetric benefits over the IGRT approach, requiring a calculation time below 1 min (3 mm grid) or below 3 min (2 mm grid). Based on this fast treatment plan generation time and due to the determined insignificance to the ART2 approach regarding the $V_{36\text{Gy}}(\text{rectum})$ criterion, the ART1 approach could be regarded as the favorable method of choice for an efficient implementation in daily ART workflows at C-arm linacs. Both mean DVH and dose-volume results for specific PACE-C criteria suggested very similar dosimetric distributions for target and OAR structures. Mean volume SD of the DVH were identified as 6.88/4.73% and 7.04/5.02% for the bladder/rectum volumes, respectively, for the ART1 and ART 2 approach. Differences for the CTV/PTV were even smaller between the two SAM-based approaches with volume SD of 0.76/0.81% and 0.63/0.73%.

For PACE-C dose criteria of both ART1 and ART2 approaches, all mean values for every relevant dose criterion were either identified in the optimal (green-colored) region or close to it, even showing very similar IQR as well as outliers. The evaluation of the two most restrictive dose criteria of the OAR $V_{37\text{Gy}}(\text{bladder}) \leq 10 \text{ cm}^3$ and $V_{36\text{Gy}}(\text{rectum}) \leq 2 \text{ cm}^3$ yielded almost identical mean values of 5.92/6.05 cm^3 and 1.37/1.3 cm^3 for the ART1/ART2 approaches, respectively. However, an additional re-optimization of the segment shapes (ART2 approach) could be of advantage as a larger extent of MLC position changes allows for an improved conformality to the daily deformed target shape. This can be seen in Figure 3.6 where the ART2 approach achieved a better match between the isodose line of 40 Gy to the CTV compared to the ART1 approach. The boxplots of the $D_{98\%}(\text{PTV})$ and $V_{36.25\text{Gy}}(\text{PTV})$ criteria support this observation by showing slightly better coverage values for the ART2 approach with 95.2% and 34.9 Gy compared to 94.8% and 34.7 Gy for the ART1 approach. Besides, a dosimetric benefit through additional shape optimization could be identified for the criteria $V_{14.5\text{Gy}}(\text{right femoral head})$ (Figure 3.8) and $V_{14.5\text{Gy}}(\text{left femoral head})$ (Figure 7.3) with obtained results of 1.29/0.89% and 1.0/0.69% for the ART1/ART2 approaches, respectively.

Moreover, in case of single and exceptionally large structure deformations mainly detected for the rectum on the sCT it was noticeable that specific ART1 optimizations reached their limits and had to be recalculated with adapted weight parameters of both target and OAR volumes (P6, sCT5; P8, sCT5; P17, sCT4; P20, sCT2). In contrast to that the ART2 approach was able to provide robust dose distributions for every aforementioned patient and, although this is not of concern within the SBRT prescription, could avoid a large proportion of dosimetric hotspots above 48 Gy.

Since no literature for SAM-based replanning within SBRT of C-arm linacs was available to our knowledge indirect comparisons were performed for studies that also investigated SAM optimization for other treatment regimens and machines. Related research on different body sites of prostate, pancreatic and lung cancer with FFF delivery argued that the treatment plan quality of SAM-based adaptation clearly constitutes a benefit over repositioned IGRT plans while being close to the dosimetric properties of a full re-optimized treatment plan¹⁷². This is in line with our results since a rising degree of re-optimization clearly yields increasing target coverage and OAR sparing. Winkel et al.⁶⁶ investigated SBRT of lymph node oligometastases at the MR linac and presented similar findings of a full-extent SAM-approach being dosimetric superior to weight-optimization, for instance, while taking longest for the plan generation.

The highest treatment plan quality and best results for the PACE-C criteria were obtained by the full re-optimization with identical IMRT constraints through the ART3 approach. With this start from scratch, the daily anatomy of the patient can be accounted for in the best possible way. Consequently, largest dosimetric benefits in the dose difference maps above 8 Gy compared to the IGRT approach were obtained as well as smallest volume SD in the mean DVH of only 6.11/3.79% for the bladder/rectum and 0.61/0.70% for the CTV/PTV. A review from a few years ago concluded that rather replanning approaches are more promising than simpler MLC adjustments matching a deformed or shifted organ structure or the alternative use of treatment libraries¹⁷³. While the presented SAM-approaches were limited to a certain extent regarding their maximum MLC displacement and specific WSO parameters, the ART3 approach had most degree of freedoms during the re-optimization and therefore achieved the best results for all 11 investigated PACE-C dose criteria except for the $V_{36.26\text{Gy}}(\text{PTV})$ with 93.67%. Compared to the ART1/ART2 approaches, the analysis of the ART3 approach yielded mean dosimetric benefits of 0.37%/0.20%, 0.76cm³/0.89cm³ and 0.33cm³/0.35cm³ for the criteria $D_{98\%}(\text{PTV})$, $V_{37\text{Gy}}(\text{bladder})$ and $V_{36\text{Gy}}(\text{rectum})$, respectively. For these three dose criteria, even the 1.5IQR of the ART3 approach results managed to come closest to the given thresholds and thus was able to restore the reference dose distributions on the pCT for a large majority of every single sCT.

This condition was also related to the configuration of the SBRT treatment planning template in Monaco since a sparing of OAR was more prioritized than maximum coverage of the PTV. Besides, the ART1 and ART2 approaches are natively build to

restore the initial target coverage rather than minimizing doses to adjacent healthy tissue⁶⁴. On account of this, a time-consuming full re-optimization of the initial treatment plan is only recommended when comparable large structural deformations of the target shape occur, pushing the SAM-based approaches to their limits of MLC-adaptations, or nearby OAR unexpectedly intersect with high dose regions. This outcome corresponds to the general perception in the field of daily online ART^{174,175} and of course, relies to a large degree on the utilized CTV-to-PTV margin¹⁷⁶.

4.2.2 Additional treatment plan evaluation methods

Along with the general validation of adaptive replanning approaches in terms of efficiency and achieving clinically given dose criteria, another objective of this thesis was to further categorize the dosimetric benefits by means of additional treatment plan evaluation methods. For this purpose, a penalty score S (inter-patient and inter-modality) was calculated in order to enable a detailed categorization of dosimetric benefits and gain insights into the distribution over the total patient collective of each adaptation approach. On top of that, an overlap volume between the PTV and bladder or rectum, respectively, was calculated for every sCT together with the DSC to compare the ability of predicting potential overdose to OAR in advance of the actual treatment plan adaptation. This could facilitate and accelerate the daily process of deciding on the most suitable treatment plan adaptation approach.

Averaged over all patients, the mean inter-patient penalty score S amounted up to 1.7 ± 2.0 , 57.1 ± 87.4 , 11.9 ± 25.7 , 13.9 ± 30.6 and 3.9 ± 11.8 for the reference plan, the IGRT, ART1, ART2 and ART3 approaches, respectively. This clearly shows the dosimetric inferiority of the IGRT approach which is reinforced by the accumulated inter-modality scores of S being obtained as 544, 852, 1800 and 5943 for the dose criteria of $V_{36.25\text{Gy}}(\text{PTV})$, $D_{98\%}(\text{PTV})$, $V_{37\text{Gy}}(\text{bladder})$ and $V_{36\text{Gy}}(\text{rectum})$ (see Figure 3.10). Moreover, it could be observed from Figure 3.9 that the majority of S reductions of the IGRT approach was rather concentrated on single patients (in particular on P4, P14 and P24) than scattered throughout the 32 patients and each single sCT. This finding indicates that the SAM-based approaches work in a robust and reliable way because dosimetric outliers allegedly are mainly related to large anatomical variations among the 5 different treatment fractions of specific patients. With assistance of the overlap volumes of these “exceptional” three patients it becomes evident why they exhibited single large penalty scores and such a comparably high SD, even for the ART3 approach. P4, P14, P24 had large mean $V_{\text{PTV} \cap \text{bladder}}$ and $V_{\text{PTV} \cap \text{rectum}}$ of (8.7 cm^3 , 13.9 cm^3 , 15.5 cm^3) and (4.9 cm^3 , 3.0 cm^3 , 4.1 cm^3) (shown in Figure 3.11), respectively, implying that perhaps only a fully re-optimized plan with modified IMRT constraints, stricter patient preparation or an entire exclusion from the SBRT regimen would have avoided these dosimetric violation. Furthermore, P24 exhibited the largest benefit gained through the ART3 approach. A different filling of the rectum caused deformations to the CTV in the anterior direction of up to 0.6 cm and thus the ART1

and ART2 approaches were not able to compensate such large respective change to the target volume adequately. On top of that, the ART3 approach was the only method that managed to eliminate a large amount of all violations identified for patients P27 and P29. As before, the evaluation of the overlap volume revealed very high mean $V_{PTV \cap bladder} / V_{PTV \cap rectum}$ of $12.9 \text{ cm}^3 / 4.4 \text{ cm}^3$ and $8.3 \text{ cm}^3 / 3.9 \text{ cm}^3$. The DSC of the CTV, bladder and rectum displayed in Figure 7.5 were not as meaningful as the overlap volume since all three metrics for P27 and P29 showed over average results except for the DSC(bladder) of P29 with 74.0%. The reason for the bad performance of the ART1 and ART2 approaches throughout almost every sCT of P27 and P29 can be found in the composition of IMRT constraints and the resulting dose distribution of the reference plan on the pCT. Both reference plans had very strict constraints for the serial function of both rectum and bladder with 100 cGy and 200 cGy lower than the constraints of the standard template shown in Figure 2.5. This also resulted in higher limits of the quadratic underdose function, leading to reference treatment plans of both patients being close to the limits of optimization. As a consequence, initial treatment plans with very stringent constraints afar from standard templates have to be monitored with extra caution during every daily plan modification with SAM.

The penalty score accumulated over every of the four dose criteria in Figure 3.10 revealed that by far most violations were determined for the $V_{36\text{Gy}}(\text{rectum})$ with $S=5943/1424/1754/254$ for the IGRT/ART1/ART2/ART3 approach in comparison to the total $S=9139/1897/2222/624$. The ART3 approach performed best for every dose criterion except for the $V_{36.25\text{Gy}}(\text{PTV})$ with $S=262$ due to aforementioned reasons. With regards to the simpler violation count, the superiority of all three re-optimization approaches ART1, ART2 and ART3 over IGRT was distorted to a certain degree as the $V_{36.25\text{Gy}}(\text{PTV})$ criterion made up large parts of all violations with $S=115/87/60/126$ versus the total $S=311/176/149/156$. The total violations of all three re-optimization approaches ART1, ART2 and ART3 were approximately half as high as the IGRT violation count. Consequently, with this simpler plan evaluation, it would not have been possible to identify that the ART1/ART2 approaches mainly generated dosimetric benefits through increasing target coverage while the ART3 approach focused on OAR sparing. Mean PTV/OAR reductions compared to the IGRT penalty score for the ART1, ART2 and ART3 approaches were obtained as 86.3%/79.9%, 89.9%/76.0% and 75.0%/95.3%.

In spite of disadvantages to simpler pass/fail countings regarding longer calculation times and potentially biased weighting toward stricter OAR criteria, the presented method of the percentage penalty score S demonstrated to offer a reliable treatment plan evaluation at one glance. It can therefore serve as a valuable action trigger for plan modifications if noteworthy deviations from a defined reference score occur during the daily treatment. Although the calculation of penalty scores can be automated, they have to be treated with caution since a visual inspection of the spatial dose distribution remains indispensable. A related research study investigating treatment plan scoring systems with SAM-based approaches at the MR linac demonstrated as well that a simple pass/fail scoring can already be helpful for a quick evaluation of different plan

adaptation strategies if specific mandatory plan criteria have to be met⁶⁶. However, if detailed knowledge about dose criteria is demanded it is definitely recommended to consider a weighted scoring system such as the presented one. It can help to guide the decision of choosing the most suitable plan adaptation strategy, especially if compromises between certain competitive dose criteria have to be made or tolerance ranges (such as for the PTV) are existent. For an efficient use in clinical routine, clear dosimetric goals have to be defined from the beginning and the number of different criteria needs to remain manageable, as presented in the ESTRO study of Bohsung et al.¹³⁷. Such a scoring system has great potential to improve the treatment planning quality of an entire department as it compares the treatment planning performance between different body sites as well as between different dosimetrists¹⁷⁷. Although requiring even more evaluated patient data and equally weighted dose criteria, a defined threshold for an accumulated penalty score rather than for single violations would be of great help for estimating the quality of a treatment plan very quickly, accelerating adaptive workflows that are lacking of standardization and systematic strategies at the moment^{25,27}.

The identified Pearson correlation coefficients between the overlap volume of the bladder or rectum and the total penalty score S indicated an intermediate correlation for every of the four treatment planning strategies, ranging between 0.43 and 0.55. In particular for the ART1/ART2 approaches this correlation was slightly higher for the rectum than for the bladder with 0.52/0.55 versus 0.50/0.49. Thus, the accumulated violations for these two SAM-based approaches were somewhat more based on rectum criterion violations than on overdose to the bladder. Contrary to this, the correlation between the DSC and the total penalty score was determined as very low with a maximum Pearson coefficient of -0.112 for the DSC(rectum) and the ART1 approach. It can be presumed on account of this correlation that the DSC is by far less suitable for correlating with certain dose-volume criteria than the overlap volume although being widely available in a lot of clinically established softwares. This corresponds to findings of similar research on the comparably small validity of the DSC in respect of dosimetric quality of a treatment plan¹³⁸.

The analysis of the coincidence of over-average overlap volumes and close-to-tolerance dose criteria of bladder/rectum yielded a good proportion for the IGRT approach with 68.5%/69.1% and very high proportions for all three re-optimization approaches with values of at least 86.9%. Therefore, the suggested overdose prediction ratio proved to be a fast and reliable measure for activating daily plan adaptation. Without doubt there is a need for such pre-defined action levels since most performed ART techniques in clinical routine are still primarily based on ad-hoc offline strategies³³. A combination of informative anatomical metrics and fast replanning methods could consequently serve as an important step for the transition from offline to online ART techniques. Similar to the obtained Pearson correlation of the DSC, the overdose prediction ratio for the DSC of bladder and rectum was much lower than in case of the overlap ratio with a maximum value of 66.7%. Although the DSC is established as a robust congruence metric for image segmentation purposes it only

reflects general similarity of organ structures instead of revealing specific regions where maximum deviations occur. The overlap volume is entirely located in the high dose region and accordingly enabled a more reliable prediction of potential overdosage to the OAR.

Besides, additional mean DVH and PACE-C criteria calculated for the $V_{\text{PTV} \cap \text{bladder}}$ and $V_{\text{PTV} \cap \text{rectum}}$ (see Figure 3.12 and Figure 7.4) proved that for the ART approaches the overlap region was the most sensitive one to dose outliers and received large parts of the total high dose. The analysis of the criteria $V_{37\text{Gy}}(V_{\text{PTV} \cap \text{bladder}})$ and $V_{36\text{Gy}}(V_{\text{PTV} \cap \text{rectum}})$ yielded a minimum ratio to its related V_x value of the total organ structure of at least 63.4%. Furthermore, the mean volume SD obtained through the DVH showed a more than twice as high value with 11.17% for the $V_{\text{PTV} \cap \text{rectum}}$ of the IGRT approach compared to the total rectum volume. The relation between the mean volume SD of the bladder and rectum of the IGRT, ART1 and ART3 approaches was more distinct than for the entire organ structures, implying again that the morphology of the rectum together with its dose criteria were the most limiting factors for adaptive replanning and that the overlap volume was able to quantify such characteristics in better detail.

Other related research argued that location-based metrics like displacement in a certain direction¹⁷⁸, a focus on air cavities in the rectum¹⁷⁹, rather high dose ($D_{1\%}$) than mediocre dose ($D_{35\%}$)¹⁸⁰ or a weighted combination of distance- and volume-based metrics¹⁸¹ correlate much better with OAR overdose than general organ volume metrics being mostly employed for segmentation quality analysis. Furthermore, methods of overlap volume histograms and analyses of wall structures in contrast to whole organs have gained increasing popularity during the last years¹⁸²⁻¹⁸⁴. Entirely alternative studies suggest to combine plan quality evaluation with a check of plan complexity in order to ensure a more stable plan delivery and a more robust dose distribution¹⁸⁵ which will be part of future research about the presented pelvic patient collective.

4.2.3 Efficiency and clinical feasibility

As presented in the previous sections, dosimetric accuracy of daily acquired sCT were within the same range as dose calculations on pCT (deviations <1.5% for dose-volume parameters and gamma pass rates > 98.7%) and achievement of specific SBRT dose criteria. However, all conceptual and technical developments retreat into the background if the proposed methods cannot be performed in a reasonable amount of time. With the patient lying on the treatment couch during the entire daily ART process, every accomplished compensation of moving organs could be mitigated the longer the segmentation or plan re-optimization takes. Although the results of a finer calculation grid of 2 mm were presented in this thesis in order to meet the SBRT treatment planning guidelines, an imminent realization in clinical routine can only be recommended with a 3mm grid or by employing a different dose calculation algorithm with a faster workstation. By using the scarcer grid, the required plan generation time was reduced

by a mean factor of 3. These obtained times depend a lot on the utilized delivery mode, degree of modulation, the set calculation uncertainty (often 1%) hardware components of the calculation workstation and also on the image resolution. Other studies using different warm-start approaches for treatment sites of prostate cancer reported plan generation times of approximately 3 min (SAM plus SWO and dose calculation)⁶⁵ and <2 min (in-house developed adaptive sequencer plus SWO including different shift methods)¹⁸⁶. Furthermore, a workflow based on priorly pre-shifted plans in combination with a SAM process was demonstrated to take 5-10 min for a collective of 6 prostate patients each having one daily image for evaluation¹³⁵. A publication about different SAM approaches at the MR linac for lymph node irradiation identified 11-119 s as total treatment generation times with a grid of 3 mm. Ates et al. made use of a similar SAM-method integrated in the Monaco TPS and presented a SAM (without dose calculation or SWO) of less than 10 s on a 16-CPU which lead to a total ART time of below 10 min for the processes of target delineation with ADMIRE, SAM, dose calculation, plan evaluation, transfer to Mosaiq and pre-delivery QA¹⁷². This is in line with the required time of our developed ART workflow of (7.1 ± 1.8) min, including the sCT creation, DIR-based automated segmentation plus subsequent manual structure correction and re-optimization of the ART1 approach (3 mm grid) of (30 ± 3) s, (30 ± 5) s and (5.2 ± 1.6) min¹²³ and (0.9 ± 0.1) min. An estimated timeframe of 2.9 min would be left to perform the steps of transferring the new plan to the record & verify system as well as for pre-treatment QA if 10 min are taken as a total reference time. Similar adaptation times have been reported within the project published by Zhang et al. that further accelerated processes through automation and parallel operations and thus were able to reduce the time of a full re-optimization-based ART workflow of 30 min reported by Ates¹⁷² to 15 min¹⁵⁶. Moreover, the issue and recommended order of applied image registrations during the daily adaptive treatment chain needs to be clarified regarding potential pitfalls. The presented approach of neural network-based sCT generation is characterized by its core feature of preserving the CBCT anatomy and only changing the HU or ED, respectively. Contrary to this, an sCT creation based on DIR includes a potential deformation of the CBCT anatomy depending on the respective morphological variation compared to the reference pCT¹⁸⁷. As a consequence, the sCT of the day should be generated prior to the DIR-based image registration onto to the pCT in order to avoid potentially large distortions and registration errors that further affect the precision of segmentation as well as dose calculation. Within our research study, the different outcomes of image registrations prior and after sCT generation were negligibly small due to the content preservation of the GAN-algorithm and the insignificant impact on the adaptive replanning approaches in which the MLC anyway underwent modifications. Potential differences between the presented IGRT approach using the same ISO as the pCT in comparison to an ISO defined as the center-of-mass of the daily contoured CTV on the sCT were identified as minor. A preliminary evaluation of the two ISO definitions based on image registration hardly showed any influence on the results for the $D_{98\%}(PTV)$ criterion, changing the dose from 32.9 Gy to 33.3 Gy. Possible shortcomings of the accomplished results within a potential online

ART workflow can be found in the lack of additional image guidance and intrafractional tracking. For a successful implementation of online adaptive replanning within SBRT regimens, the presented methods have to be combined with tracking devices such as ultrasound^{188,189}, markers/transponder beacons¹⁹⁰ or EPID megavoltage imaging¹⁹¹. These methods enable monitoring of the target and OAR volumes' motion during the plan delivery and thus further increase the accuracy of the deposited dose. Besides, the acquisition of a second CBCT in advance of the modified treatment plan's application, gating procedures or kV monitoring^{192,193} could generate additional dosimetric accuracy.

Regardless of the study's retrospective design, it was demonstrated that the evaluated adaptive replanning approaches were able to guarantee a precise daily dose delivery which constitutes a relevant step for the transition from offline to online adaptive methods in stereotactic prostate cancer radiation therapy²⁵. A lot of related research has been performed for the pelvic body site during the last decade, proving a successful compensation of organ motion and target deformation. However, most of the previously presented findings were performed within a normo-fractionated treatment regimen having larger PTV margin, investigated more than five fractions or were focused on the preservation of target coverage^{30,89,194}. Along with identifying deficiencies of an IGRT approach, this study was able to provide a variety of different warm-start and re-optimization approaches dependent on the available planning time (ART1 approach), with a focus on target coverage (ART2) or additional OAR sparing (ART3) within the framework of an internationally relevant SBRT trial. These results can be combined with techniques of automation and deep learning, for example with regard to image correction^{110,123}, segmentation^{55,151}, treatment planning¹⁹⁵ and QA¹⁹⁶, in order to reinforce the advantages gained through ART within the long-time debate about the cost-benefit assessment of online adaptive methods¹⁹⁷⁻¹⁹⁹.

More studies will be needed, performed on larger patient collectives and with an increased diversity of plan delivery modes in order to provide reliable estimations about total ART workflow times. A combination with automation and deep-learning processes seems inevitable but creates additional time for mandatory tracking methods or QA procedures. Especially in terms of high doses over 5Gy applied in only a few total number of fractions, methods of fast plan validation or online QA^{33,200-202} are highly recommended for ensuring dosimetric accuracy²⁰³. They ideally operate in real time prior or during the delivery and can be realized through systems such as transmission detectors⁷⁶, EPID dose verification^{204,205} or linac logfile tracking^{206,207}. With a total time of approximately 7.1min, the novel sCT-based approach provided promising and robust results in respect of image quality, image segmentation and adaptive replanning. If combined with the aforementioned methods of online QA, tracking, standardized action levels and automation, the presented ART techniques can be successfully transferred from offline to daily online applications and also to more tumor sites than male pelvis.

5 SUMMARY

The increasing use of ultra-hypofractionated, stereotactic radiation therapy during the last years for a lot of tumor sites including the prostate demands for higher precision of daily treatments. Together with recent advances in the field of deep learning, daily acquired images like CBCT could reach their full potential by being further processed for realizing strategies of adaptive radiation therapy (ART). Therefore, the goal of this thesis was to analyze the general accuracy of a novel deep learning-based approach for synthetic CT (sCT) generation with CBCT and, being complemented with different adaptive replanning strategies, evaluate the dosimetric benefits of the proposed adaptive methods over conventional image-guided radiation therapy (IGRT) with the aim of a clinical implementation in daily routine.

The first part of this thesis was concerned with the validation of the cycle-generative adversarial network (GAN)-based model for the pelvis. Having been trained with multimodal paired planning CT and CBCT, the pelvic sCT model was subsequently employed for creating sCT on the basis of daily acquired kV-CBCT for a separate collective of 15 prostate cancer patients. With a focus on clinical feasibility, the accuracy of successive core aspects of an adaptive workflow being imaging, segmentation and dose calculation was evaluated. The cyce-GAN algorithm implemented in the Monaco research environment demonstrated to successfully process CBCT and create sCT with image quality close to the reference pCT, serving as an alternative to CT on rails and MRI. All obtained mean errors and mean absolute errors were competitive to recent findings about sCT image uncertainties with mean values of (5.4 ± 4.6) HU and (41.8 ± 4.6) HU.

Moreover, the generation of a sCT was feasible within (30 ± 3) s and without the need of additional image registration to the pCT while disproving the major concern of distorting the daily patient anatomy. Subsequent image segmentation based on deformable image registration (DIR) provided acceptable organ structures within (30 ± 5) s per structure set, especially in terms of congruence to manual contouring for the bladder and prostate having mean dice similarity coefficients of $(90.5 \pm 3.6)\%$ and $(85.9 \pm 3.3)\%$ compared to the reference structure on the planning CT. Further refinements of image contrast are needed with respect to definition of organ overlaps in soft tissue regions, potentially accelerating the required time for automation and following manual edits. Through sCT generation, the obtained CT numbers were precise enough to ensure a robust and reliable dose accuracy with deviations between the sCT and pCT not exceeding $\pm 1.5\%$ for the target structure's dose parameters of D_{98} , D_{50} and D_2 and $\pm 1.0\%$ for the bladder and rectum parameters of V_{40} , V_{50} and V_{60} . Furthermore, mean gamma pass rates of $99.9 \pm 0.1\%$ (3%/3mm criterion) and $98.5 \pm 1.7\%$ (2%/2mm criterion) between the sCT and pCT were proven to be in the range of similar CBCT-based sCT studies and fulfilled the clinical threshold rate of 95% with a low standard variation. Thus, the novel approach of GAN-based sCT creation was proven to be clinically feasible with regard to every essential treatment component at

CBCT-based C-arm linacs. Most importantly, all workflow steps were performed within one established software environment and offer the possibility of being customized to individual department setups, not only due to the adjustable training procedure of the GAN-based sCT algorithm. Future enhancements of the novel sCT approach will focus on improving the soft tissue contrast with more training data including exceptional anatomies (implants, radioactive seeds,...), extending the field-of-view or correcting the native CBCT image contrast by means of an anti-scatter grid, for example. Additional time acceleration could be realized by improving the image conversion on a software or hardware level and complement the DIR-based segmentation with deep learning or atlas-based approaches.

Representing the next pending issue in an adaptive workflow, the evaluation of different adaptive replanning approaches on the previously validated sCT within the framework of recently relevant ultra-hypofractionated, stereotactic prostate cancer radiation therapy constituted this thesis' second main focus. Based on the analysis of a larger collective of 32 patients with each having 5 daily CBCT, the methods of segment aperture morphing-based warm start optimization (ART1/ART2 approaches) accomplished substantial dosimetric benefits over the conventional IGRT approach by improving the mean PACE-C dose criteria $D_{98\%}(PTV)$ and $V_{36Gy}(rectum)$ from 32.9% and 2.0 cm³ to 34.7%/34.9% and 1.4 cm³/1.4 cm³, respectively. The ART1 approach was able to provide a modified treatment plan within 3 min (2 mm grid) or under 1 min (3 mm grid). Although achieving best dosimetric distributions particularly for the OAR with mean results of 5.2 cm³/1.0 cm³ for the bladder/rectum criteria, the ART3 approach cannot be entirely recommended yet for online adaptations due to its time-consuming calculation of at least 6.7 min. Apart from the conventional analysis with dose-volume parameters, the evaluation with a penalty scoring system revealed that criteria-violating plans among the total patient collective were rather concentrated on single patients than randomly scattered. In contrast to the target prioritization of the SAM-based ART1 and ART2 approaches, the ART3 approach focused on improving OAR sparing. The consideration of additional segmentation metrics showed that an overlap ratio between the PTV and the bladder or rectum ensured a superior prediction of potential overdose to OAR with ratios of at least 86.9%, particularly when being compared to the performance of the DSC with a maximum ratio of 66.7%. These outcomes enable a guidance for the decision of when to apply which adaptation strategy. Based on the specific characteristics of each different adaptation approach and the knowledge gained through anatomical metrics, valuable time prior to the actual treatment plan modification can therefore be saved.

Overall, an entire adaptive workflow was demonstrated to become feasible within 0.5 min + 0.5 min + 5.2 min + 0.9 min (ART1 approach) = 7.1 min. Complemented with currently missing standardized action levels as well as methods of online QA and intrafractional tracking, the investigated techniques were sufficiently accurate and fast to constitute a crucial step towards the clinical implementation of online adaptation methods for prostate cancer therapy at C-arm linacs and besides have the potential to be transferred to other relevant body sites which are in need of daily adaptation.

6 BIBLIOGRAPHY

1. Deutschland, SB: Anzahl der Gestorbenen nach Kapiteln der IDC-10 und nach Geschlecht für 2019. https://www.destatis.de/DE/Themen/Gesellschaft-Umwelt/Gesundheit/Todesursachen/Tabellen/gestorbene_anzahl.html;jsessionid=81C7BF1E72F132A8A31B85377D069536internet8711, Accessed, 2020.
2. Cancer, IAFro, W.H.O.: All cancers. <https://gco.iarc.fr/today/data/factsheets/cancers/39-All-cancers-fact-sheet.pdf>, Accessed: January 5th, 2020.
3. International Agency for Research on Cancer, WHO: Cancer today. <https://gco.iarc.fr/today>, Accessed: January 5th, 2020.
4. Sautter-Biel, ML, Bamberg, M: *Strahlen für das Leben*, Deutsche Gesellschaft für Radioonkologie e.V., 2015.
5. Wannemacher, M, Wenz, F, Debus, J: *Strahlentherapie*, Springer Berlin Heidelberg, 2013.
6. Schlegel, W, Karger, CP, Jäkel, O: *Medizinische Physik*, 2018.
7. Sheng, K: Artificial intelligence in radiotherapy: a technological review. *Front Med*, 14: 431-449, 2020.
8. Lim-Reinders, S, Keller, BM, Al-Ward, S, Sahgal, A, Kim, A: Online Adaptive Radiation Therapy. *Int J Radiat Oncol Biol Phys*, 99: 994-1003, 2017.
9. Thompson, RF, Valdes, G, Fuller, CD, Carpenter, CM, Morin, O, Aneja, S, Lindsay, WD, Aerts, H, Agrimson, B, Deville, C, Jr., Rosenthal, SA, Yu, JB, Thomas, CR, Jr.: Artificial intelligence in radiation oncology: A specialty-wide disruptive transformation? *Radiother Oncol*, 129: 421-426, 2018.
10. Winkel, D, Bol, GH, Kroon, PS, van Asselen, B, Hackett, SS, Werensteijn-Honingh, AM, Intven, MPW, Eppinga, WSC, Tijssen, RHN, Kerkmeijer, LGW, de Boer, HCJ, Mook, S, Meijer, GJ, Hes, J, Willemsen-Bosman, M, de Groot-van Breugel, EN, Jurgenliemk-Schulz, IM, Raaymakers, BW: Adaptive radiotherapy: The Elekta Unity MR-linac concept. *Clin Transl Radiat Oncol*, 18: 54-59, 2019.
11. Jones, D: ICRU Report 50—Prescribing, Recording and Reporting Photon Beam Therapy. *Medical Physics*, 21: 833-834, 1994.
12. Landberg, T, Chavaudra, J, Dobbs, J, Gerard, J-P, Hanks, G, Horiot, J-C, Johansson, K-A, Möller, T, Purdy, J, Suntharalingam, N, Svensson, H: Report 62. *Journal of the International Commission on Radiation Units and Measurements*, os32: NP-NP, 2016.
13. Emami, B, Lyman, J, Brown, A, Coia, L, Goitein, M, Munzenrider, JE, Shank, B, Solin, LJ, Wesson, M: Tolerance of normal tissue to therapeutic irradiation. *Int J Radiat Oncol Biol Phys*, 21: 109-122, 1991.
14. Sanghani, M, Mignano, J: Intensity modulated radiation therapy: a review of current practice and future directions. *Technol Cancer Res Treat*, 5: 447-450, 2006.
15. Herman Tde, L, Schnell, E, Young, J, Hildebrand, K, Algan, O, Syzek, E, Herman, T, Ahmad, S: Dosimetric comparison between IMRT delivery modes: Step-and-shoot, sliding window, and volumetric modulated arc therapy - for whole pelvis radiation therapy of intermediate-to-high risk prostate adenocarcinoma. *J Med Phys*, 38: 165-172, 2013.
16. Khan, FM, Gibbons, JP, Sperduto, PW: *Khan's treatment planning in radiation oncology*, Lippincott Williams and Wilkins, 2016.
17. Miften, M, Olch, A, Mihailidis, D, Moran, J, Pawlicki, T, Molineu, A, Li, H, Wijesooriya, K, Shi, J, Xia, P, Papanikolaou, N, Low, DA: Tolerance limits and methodologies for IMRT measurement-based verification QA:

- Recommendations of AAPM Task Group No. 218. *Med Phys*, 45: e53-e83, 2018.
18. Low, DA, Moran, JM, Dempsey, JF, Dong, L, Oldham, M: Dosimetry tools and techniques for IMRT. *Med Phys*, 38: 1313-1338, 2011.
 19. Bourland, JD: *Image-Guided Radiation Therapy*, Baton Rouge, UNITED STATES, Taylor & Francis Group, 2012.
 20. Boda-Heggemann, J, Lohr, F, Wenz, F, Flentje, M, Guckenberger, M: kV cone-beam CT-based IGRT: a clinical review. *Strahlenther Onkol*, 187: 284-291, 2011.
 21. Bujold, A, Craig, T, Jaffray, D, Dawson, LA: Image-guided radiotherapy: has it influenced patient outcomes? *Semin Radiat Oncol*, 22: 50-61, 2012.
 22. Abel, S, Lee, S, Ludmir, EB, Verma, V: Principles and Applications of Stereotactic Radiosurgery and Stereotactic Body Radiation Therapy. *Hematol Oncol Clin North Am*, 33: 977-987, 2019.
 23. Kupelian, P, Meyer, JL: Image-Guided, Adaptive Radiotherapy of Prostate Cancer: Toward New Standards of Radiotherapy Practice. *Frontiers of Radiation Therapy and Oncology*, 43: 344-368, 2011.
 24. Posiewnik, M, Piotrowski, T: A review of cone-beam CT applications for adaptive radiotherapy of prostate cancer. *Phys Med*, 59: 13-21, 2019.
 25. McVicar, N, Popescu, IA, Heath, E: Techniques for adaptive prostate radiotherapy. *Phys Med*, 32: 492-498, 2016.
 26. Zaorsky, NG, Harrison, AS, Trabulsi, EJ, Gomella, LG, Showalter, TN, Hurwitz, MD, Dicker, AP, Den, RB: Evolution of advanced technologies in prostate cancer radiotherapy. *Nat Rev Urol*, 10: 565-579, 2013.
 27. Stankiewicz, M, Li, W, Rosewall, T, Tadic, T, Dickie, C, Velec, M: Patterns of practice of adaptive re-planning for anatomic variances during cone-beam CT guided radiotherapy. *Technical Innovations & Patient Support in Radiation Oncology*, 12: 50-55, 2019.
 28. Jensen, AD, Nill, S, Huber, PE, Bendl, R, Debus, J, Munter, MW: A clinical concept for interfractional adaptive radiation therapy in the treatment of head and neck cancer. *Int J Radiat Oncol Biol Phys*, 82: 590-596, 2012.
 29. Moller, DS, Holt, MI, Alber, M, Tvilum, M, Khalil, AA, Knap, MM, Hoffmann, L: Adaptive radiotherapy for advanced lung cancer ensures target coverage and decreases lung dose. *Radiother Oncol*, 121: 32-38, 2016.
 30. Qin, A, Sun, Y, Liang, J, Yan, D: Evaluation of online/offline image guidance/adaptation approaches for prostate cancer radiation therapy. *Int J Radiat Oncol Biol Phys*, 91: 1026-1033, 2015.
 31. Sonke, JJ, Aznar, M, Rasch, C: Adaptive Radiotherapy for Anatomical Changes. *Semin Radiat Oncol*, 29: 245-257, 2019.
 32. Yan, D, Vicini, F, Wong, J, Martinez, A: Adaptive radiation therapy. *Physics in Medicine and Biology*, 42: 123-132, 1997.
 33. Bertholet, J, Anastasi, G, Noble, D, Bel, A, van Leeuwen, R, Roggen, T, Duchateau, M, Pilskog, S, Garibaldi, C, Tilly, N, Garcia-Molla, R, Bonaque, J, Oelfke, U, Aznar, MC, Heijmen, B: Patterns of practice for adaptive and real-time radiation therapy (POP-ART RT) part II: Offline and online plan adaption for interfractional changes. *Radiother Oncol*, 2020.
 34. Green, OL, Henke, LE, Hugo, GD: Practical Clinical Workflows for Online and Offline Adaptive Radiation Therapy. *Semin Radiat Oncol*, 29: 219-227, 2019.
 35. Poludniowski, GG, Evans, PM, Webb, S: Cone beam computed tomography number errors and consequences for radiotherapy planning: an investigation of correction methods. *Int J Radiat Oncol Biol Phys*, 84: e109-114, 2012.

36. Schulze, R, Heil, U, Gross, D, Bruellmann, DD, Dranischnikow, E, Schwanecke, U, Schoemer, E: Artefacts in CBCT: a review. *Dentomaxillofac Radiol*, 40: 265-273, 2011.
37. Giacometti, V, Hounsell, AR, McGarry, CK: A review of dose calculation approaches with cone beam CT in photon and proton therapy. *Phys Med*, 76: 243-276, 2020.
38. Fotina, I, Hopfgartner, J, Stock, M, Steininger, T, Lutgendorf-Caucig, C, Georg, D: Feasibility of CBCT-based dose calculation: comparative analysis of HU adjustment techniques. *Radiother Oncol*, 104: 249-256, 2012.
39. Schröder, L, Stankovic, U, Remeijer, P, Sonke, J-J: Evaluating the impact of cone-beam computed tomography scatter mitigation strategies on radiotherapy dose calculation accuracy. *Physics and Imaging in Radiation Oncology*, 10: 35-40, 2019.
40. Srinivasan, K, Mohammadi, M, Shepherd, J: Applications of linac-mounted kilovoltage Cone-beam Computed Tomography in modern radiation therapy: A review. *Pol J Radiol*, 79: 181-193, 2014.
41. Brock, KK, Mutic, S, McNutt, TR, Li, H, Kessler, ML: Use of image registration and fusion algorithms and techniques in radiotherapy: Report of the AAPM Radiation Therapy Committee Task Group No. 132. *Med Phys*, 44: e43-e76, 2017.
42. Rigaud, B, Simon, A, Castelli, J, Lafond, C, Acosta, O, Haigron, P, Cazoulat, G, de Crevoisier, R: Deformable image registration for radiation therapy: principle, methods, applications and evaluation. *Acta Oncol*, 58: 1225-1237, 2019.
43. Paganelli, C, Meschini, G, Molinelli, S, Riboldi, M, Baroni, G: "Patient-specific validation of deformable image registration in radiation therapy: Overview and caveats". *Med Phys*, 45: e908-e922, 2018.
44. Cole, AJ, Veiga, C, Johnson, U, D'Souza, D, Lalli, NK, McClelland, JR: Toward adaptive radiotherapy for lung patients: feasibility study on deforming planning CT to CBCT to assess the impact of anatomical changes on dosimetry. *Phys Med Biol*, 63: 155014, 2018.
45. Maier, A, Syben, C, Lasser, T, Riess, C: A gentle introduction to deep learning in medical image processing. *Z Med Phys*, 29: 86-101, 2019.
46. Kaji, S, Kida, S: Overview of image-to-image translation by use of deep neural networks: denoising, super-resolution, modality conversion, and reconstruction in medical imaging. *Radiol Phys Technol*, 12: 235-248, 2019.
47. Hesamian, MH, Jia, W, He, X, Kennedy, P: Deep Learning Techniques for Medical Image Segmentation: Achievements and Challenges. *J Digit Imaging*, 32: 582-596, 2019.
48. Sahiner, B, Pezeshk, A, Hadjiiski, LM, Wang, X, Drukker, K, Cha, KH, Summers, RM, Giger, ML: Deep learning in medical imaging and radiation therapy. *Med Phys*, 46: e1-e36, 2019.
49. Boldrini, L, Bibault, JE, Masciocchi, C, Shen, Y, Bittner, MI: Deep Learning: A Review for the Radiation Oncologist. *Front Oncol*, 9: 977, 2019.
50. Barragan-Montero, A, Javaid, U, Valdes, G, Nguyen, D, Desbordes, P, Macq, B, Willems, S, Vandewinckele, L, Holmstrom, M, Lofman, F, Michiels, S, Souris, K, Stepin, E, Lee, JA: Artificial intelligence and machine learning for medical imaging: A technology review. *Phys Med*, 83: 242-256, 2021.
51. Spadea, MF, Maspero, M, Zaffino, P, Seco, J: Deep learning-based synthetic-CT generation in radiotherapy and PET: a review. *Med Phys*, 2021.
52. Maspero, M, Houweling, AC, Savenije, MHF, van Heijst, TCF, Verhoeff, JJC, Kotte, ANTJ, van den Berg, CAT: A single neural network for cone-beam computed

- tomography-based radiotherapy of head-and-neck, lung and breast cancer. *Physics and Imaging in Radiation Oncology*, 14: 24-31, 2020.
53. Harms, J, Lei, Y, Wang, T, Zhang, R, Zhou, J, Tang, X, Curran, WJ, Liu, T, Yang, X: Paired cycle-GAN-based image correction for quantitative cone-beam computed tomography. *Med Phys*, 2019.
54. Hansen, DC, Landry, G, Kamp, F, Li, M, Belka, C, Parodi, K, Kurz, C: ScatterNet: A convolutional neural network for cone-beam CT intensity correction. *Med Phys*, 45: 4916-4926, 2018.
55. Cardenas, CE, Yang, J, Anderson, BM, Court, LE, Brock, KB: Advances in Auto-Segmentation. *Semin Radiat Oncol*, 29: 185-197, 2019.
56. Samarasinghe, G, Jameson, M, Vinod, S, Field, M, Dowling, J, Sowmya, A, Holloway, L: Deep learning for segmentation in radiation therapy planning: a review. *J Med Imaging Radiat Oncol*, 65: 578-595, 2021.
57. Vrtovec, T, Mocnik, D, Strojanc, P, Pernus, F, Ibragimov, B: Auto-segmentation of organs at risk for head and neck radiotherapy planning: From atlas-based to deep learning methods. *Med Phys*, 47: e929-e950, 2020.
58. Wong, J, Fong, A, McVicar, N, Smith, S, Giambattista, J, Wells, D, Kolbeck, C, Giambattista, J, Gondara, L, Alexander, A: Comparing deep learning-based auto-segmentation of organs at risk and clinical target volumes to expert inter-observer variability in radiotherapy planning. *Radiother Oncol*, 144: 152-158, 2019.
59. Yang, Y, Jiang, H, Sun, Q: A Multiorgan Segmentation Model for CT Volumes via Full Convolution-Deconvolution Network. *Biomed Res Int*, 2017: 6941306, 2017.
60. Yang, J, Veeraraghavan, H, Armato, SG, 3rd, Farahani, K, Kirby, JS, Kalpathy-Kramer, J, van Elmpt, W, Dekker, A, Han, X, Feng, X, Aljabar, P, Oliveira, B, van der Heyden, B, Zamdborg, L, Lam, D, Gooding, M, Sharp, GC: Autosegmentation for thoracic radiation treatment planning: A grand challenge at AAPM 2017. *Med Phys*, 45: 4568-4581, 2018.
61. Antico, M, Prinsen, P, Cellini, F, Fracassi, A, Isola, AA, Cobben, D, Fontanarosa, D: Real-time adaptive planning method for radiotherapy treatment delivery for prostate cancer patients, based on a library of plans accounting for possible anatomy configuration changes. *PLoS One*, 14: e0213002, 2019.
62. Heijkoop, ST, Langerak, TR, Quint, S, Bondar, L, Mens, JW, Heijmen, BJ, Hoogeman, MS: Clinical implementation of an online adaptive plan-of-the-day protocol for nonrigid motion management in locally advanced cervical cancer IMRT. *Int J Radiat Oncol Biol Phys*, 90: 673-679, 2014.
63. Crijns, W, Van Herck, H, Defraene, G, Van den Bergh, L, Slagmolen, P, Haustermans, K, Maes, F, Van den Heuvel, F: Dosimetric adaptive IMRT driven by fiducial points. *Med Phys*, 41: 061716, 2014.
64. Ahunbay, EE, Peng, C, Chen, GP, Narayanan, S, Yu, C, Lawton, C, Li, XA: An online replanning scheme for interfractional variations. *Med Phys*, 35: 3607-3615, 2008.
65. Ahunbay, EE, Peng, C, Holmes, S, Godley, A, Lawton, C, Li, XA: Online adaptive replanning method for prostate radiotherapy. *Int J Radiat Oncol Biol Phys*, 77: 1561-1572, 2010.
66. Winkel, D, Bol, GH, Werensteijn-Honingh, AM, Kiekebosch, IH, van Asselen, B, Intven, MPW, Eppinga, WSC, Raaymakers, BW, Jürgenliemk-Schulz, IM, Kroon, PS: Evaluation of plan adaptation strategies for stereotactic radiotherapy of lymph node oligometastases using online magnetic resonance image guidance. *Physics and Imaging in Radiation Oncology*, 9: 58-64, 2019.

67. Hussein, M, Heijmen, BJM, Verellen, D, Nisbet, A: Automation in intensity modulated radiotherapy treatment planning-a review of recent innovations. *Br J Radiol*, 91: 20180270, 2018.
68. Campbell, WG, Miften, M, Olsen, L, Stumpf, P, Schefter, T, Goodman, KA, Jones, BL: Neural network dose models for knowledge-based planning in pancreatic SBRT. *Med Phys*, 44: 6148-6158, 2017.
69. Wang, M, Zhang, Q, Lam, S, Cai, J, Yang, R: A Review on Application of Deep Learning Algorithms in External Beam Radiotherapy Automated Treatment Planning. *Front Oncol*, 10: 580919, 2020.
70. Cai, B, Green, OL, Kashani, R, Rodriguez, VL, Mutic, S, Yang, D: A practical implementation of physics quality assurance for photon adaptive radiotherapy. *Z Med Phys*, 28: 211-223, 2018.
71. Yang, D, Moore, KL: Automated radiotherapy treatment plan integrity verification. *Med Phys*, 39: 1542-1551, 2012.
72. Sekar, Y, Thoelking, J, Eckl, M, Kalichava, I, Sihono, DSK, Lohr, F, Wenz, F, Wertz, H: Characterization and clinical evaluation of a novel 2D detector array for conventional and flattening filter free (FFF) IMRT pre-treatment verification. *Z Med Phys*, 28: 134-141, 2018.
73. Rose, MS, Tirpak, L, Van Casteren, K, Zack, J, Simon, T, Schoenfeld, A, Simon, W: Multi-institution validation of a new high spatial resolution diode array for SRS and SBRT plan pretreatment quality assurance. *Med Phys*, 47: 3153-3164, 2020.
74. Stelljes, TS, Harmeyer, A, Reuter, J, Looe, HK, Chofor, N, Harder, D, Poppe, B: Dosimetric characteristics of the novel 2D ionization chamber array OCTAVIUS Detector 1500. *Med Phys*, 42: 1528-1537, 2015.
75. Hoffmann, L, Alber, M, Söhn, M, Elstrøm, UV: Validation of the Acuros XB dose calculation algorithm versus Monte Carlo for clinical treatment plans. *Medical Physics*, 45: 3909-3915, 2018.
76. Thoelking, J, Fleckenstein, J, Sekar, Y, Boggula, R, Lohr, F, Wenz, F, Wertz, H: Patient-specific online dose verification based on transmission detector measurements. *Radiother Oncol*, 119: 351-356, 2016.
77. Zwan, BJ, Caillet, V, Booth, JT, Colvill, E, Fuangrod, T, O'Brien, R, Briggs, A, O'Connor, DJ, Keall, PJ, Greer, PB: Toward real-time verification for MLC tracking treatments using time-resolved EPID imaging. *Med Phys*, 2020.
78. Razinskas, G, Wegener, S, Greber, J, Sauer, OA: Sensitivity of the IQM transmission detector to errors of VMAT plans. *Med Phys*, 2018.
79. Stanhope, CW, Drake, DG, Liang, J, Alber, M, Sohn, M, Habib, C, Willcut, V, Yan, D: Evaluation of machine log files/MC-based treatment planning and delivery QA as compared to ArcCHECK QA. *Med Phys*, 45: 2864-2874, 2018.
80. Pasler, M, Kaas, J, Perik, T, Geuze, J, Dreindl, R, Kunzler, T, Wittkamper, F, Georg, D: Linking log files with dosimetric accuracy--A multi-institutional study on quality assurance of volumetric modulated arc therapy. *Radiother Oncol*, 117: 407-411, 2015.
81. Menten, MJ, Mohajer, JK, Nilawar, R, Bertholet, J, Dunlop, A, Pathmanathan, AU, Moreau, M, Marshall, S, Wetscherek, A, Nill, S, Tree, AC, Oelfke, U: Automatic reconstruction of the delivered dose of the day using MR-linac treatment log files and online MR imaging. *Radiother Oncol*, 145: 88-94, 2020.
82. Chetty, IJ, Rosu-Bubulac, M: Deformable Registration for Dose Accumulation. *Semin Radiat Oncol*, 29: 198-208, 2019.
83. Kamerling, CP, Fast, MF, Ziegenhein, P, Menten, MJ, Nill, S, Oelfke, U: Online dose reconstruction for tracked volumetric arc therapy: Real-time

- implementation and offline quality assurance for prostate SBRT. *Med Phys*, 44: 5997-6007, 2017.
84. Portaluri, M, Barba, MC, Musio, D, Tramacere, F, Pati, F, Bambace, S: Hypofractionation in COVID-19 radiotherapy: A mix of evidence based medicine and of opportunities. *Radiother Oncol*, 150: 191-194, 2020.
85. Lehrer, EJ, Kishan, AU, Yu, JB, Trifiletti, DM, Showalter, TN, Ellis, R, Zaorsky, NG: Ultrahypofractionated versus hypofractionated and conventionally fractionated radiation therapy for localized prostate cancer: A systematic review and meta-analysis of phase III randomized trials. *Radiother Oncol*, 148: 235-242, 2020.
86. Scaife, JE, Thomas, SJ, Harrison, K, Romanchikova, M, Sutcliffe, MP, Forman, JR, Bates, AM, Jena, R, Parker, MA, Burnet, NG: Accumulated dose to the rectum, measured using dose-volume histograms and dose-surface maps, is different from planned dose in all patients treated with radiotherapy for prostate cancer. *Br J Radiol*, 88: 20150243, 2015.
87. Bostel, T, Sachpazidis, I, Splinter, M, Bougatf, N, Fechter, T, Zamboglou, C, Jakel, O, Huber, PE, Baltas, D, Debus, J, Nicolay, NH: Dosimetric Impact of Interfractional Variations in Prostate Cancer Radiotherapy-Implications for Imaging Frequency and Treatment Adaptation. *Front Oncol*, 9: 940, 2019.
88. Jmour, O, Benna, M, Champagnol, P, Ben Mrad, M, Hamrouni, A, Obeid, L, Lahmamssi, C, Bousarsar, A, Vial, N, Rehailla-Blanchard, A, Sotton, S, Lan, M, Langrand-Escure, J, Vallard, A, Magne, N: CBCT evaluation of inter- and intra-fraction motions during prostate stereotactic body radiotherapy: a technical note. *Radiat Oncol*, 15: 85, 2020.
89. Bockelmann, F, Putz, F, Kallis, K, Lettmaier, S, Fietkau, R, Bert, C: Adaptive radiotherapy and the dosimetric impact of inter- and intrafractional motion on the planning target volume for prostate cancer patients. *Strahlenther Onkol*, 2020.
90. McMahon, SJ: The linear quadratic model: usage, interpretation and challenges. *Phys Med Biol*, 64: 01TR01, 2018.
91. Sauer, R: *Strahlentherapie und Onkologie*, München, Elsevier: Urban und Fischer, 2010.
92. Thames, HD, Jr., Withers, HR, Peters, LJ, Fletcher, GH: Changes in early and late radiation responses with altered dose fractionation: implications for dose-survival relationships. *Int J Radiat Oncol Biol Phys*, 8: 219-226, 1982.
93. Nahum, AE: The radiobiology of hypofractionation. *Clin Oncol (R Coll Radiol)*, 27: 260-269, 2015.
94. Wolf, F, Sedlmayer, F, Aebbersold, D, Albrecht, C, Bohmer, D, Flentje, M, Ganswindt, U, Ghadjar, P, Hocht, S, Holscher, T, Muller, AC, Niehoff, P, Pinkawa, M, Schmidt-Hegemann, NS, Zamboglou, C, Zips, D, Wiegel, T: Ultrahypofractionation of localized prostate cancer : Statement from the DEGRO working group prostate cancer. *Strahlenther Onkol*, 2020.
95. Hocht, S, Aebbersold, DM, Albrecht, C, Bohmer, D, Flentje, M, Ganswindt, U, Holscher, T, Martin, T, Sedlmayer, F, Wenz, F, Zips, D, Wiegel, T: Hypofractionated radiotherapy for localized prostate cancer. *Strahlenther Onkol*, 193: 1-12, 2017.
96. van Leeuwen, CM, Oei, AL, Crezee, J, Bel, A, Franken, NAP, Stalpers, LJA, Kok, HP: The alfa and beta of tumours: a review of parameters of the linear-quadratic model, derived from clinical radiotherapy studies. *Radiat Oncol*, 13: 96, 2018.
97. Wang, JZ, Guerrero, M, Li, XA: How low is the alpha/beta ratio for prostate cancer? *Int J Radiat Oncol Biol Phys*, 55: 194-203, 2003.

98. Pilonis, KA, Vanpouille-Box, C, Demaria, S: Combination of radiotherapy and immune checkpoint inhibitors. *Semin Radiat Oncol*, 25: 28-33, 2015.
99. Kishan, AU, Dang, A, Katz, AJ, Mantz, CA, Collins, SP, Aghdam, N, Chu, FI, Kaplan, ID, Appelbaum, L, Fuller, DB, Meier, RM, Loblaw, DA, Cheung, P, Pham, HT, Shaverdian, N, Jiang, N, Yuan, Y, Bagshaw, H, Prionas, N, Buyyounouski, MK, Spratt, DE, Linson, PW, Hong, RL, Nickols, NG, Steinberg, ML, Kupelian, PA, King, CR: Long-term Outcomes of Stereotactic Body Radiotherapy for Low-Risk and Intermediate-Risk Prostate Cancer. *JAMA Netw Open*, 2: e188006, 2019.
100. Kothari, G, Loblaw, A, Tree, AC, van As, NJ, Moghanaki, D, Lo, SS, Ost, P, Siva, S: Stereotactic Body Radiotherapy for Primary Prostate Cancer. *Technol Cancer Res Treat*, 17: 1533033818789633, 2018.
101. Wilkins, A, Mossop, H, Syndikus, I, Khoo, V, Bloomfield, D, Parker, C, Logue, J, Scrase, C, Patterson, H, Birtle, A, Staffurth, J, Malik, Z, Panades, M, Eswar, C, Graham, J, Russell, M, Kirkbride, P, O'Sullivan, JM, Gao, A, Cruickshank, C, Griffin, C, Dearnaley, D, Hall, E: Hypofractionated radiotherapy versus conventionally fractionated radiotherapy for patients with intermediate-risk localised prostate cancer: 2-year patient-reported outcomes of the randomised, non-inferiority, phase 3 CHHiP trial. *The Lancet Oncology*, 16: 1605-1616, 2015.
102. Dearnaley, D, Syndikus, I, Mossop, H, Khoo, V, Birtle, A, Bloomfield, D, Graham, J, Kirkbride, P, Logue, J, Malik, Z, Money-Kyrle, J, O'Sullivan, JM, Panades, M, Parker, C, Patterson, H, Scrase, C, Staffurth, J, Stockdale, A, Tremlett, J, Bidmead, M, Mayles, H, Naismith, O, South, C, Gao, A, Cruickshank, C, Hassan, S, Pugh, J, Griffin, C, Hall, E: Conventional versus hypofractionated high-dose intensity-modulated radiotherapy for prostate cancer: 5-year outcomes of the randomised, non-inferiority, phase 3 CHHiP trial. *The Lancet Oncology*, 17: 1047-1060, 2016.
103. Incrocci, L, Wortel, RC, Alemayehu, WG, Aluwini, S, Schimmel, E, Krol, S, van der Toorn, P-P, Jager, Hd, Heemsbergen, W, Heijmen, B, Pos, F: Hypofractionated versus conventionally fractionated radiotherapy for patients with localised prostate cancer (HYPRO): final efficacy results from a randomised, multicentre, open-label, phase 3 trial. *The Lancet Oncology*, 17: 1061-1069, 2016.
104. Jackson, WC, Silva, J, Hartman, HE, Dess, RT, Kishan, AU, Beeler, WH, Gharzai, LA, Jaworski, EM, Mehra, R, Hearn, JWD, Morgan, TM, Salami, SS, Cooperberg, MR, Mahal, BA, Soni, PD, Kaffenberger, S, Nguyen, PL, Desai, N, Feng, FY, Zumsteg, ZS, Spratt, DE: Stereotactic Body Radiation Therapy for Localized Prostate Cancer: A Systematic Review and Meta-Analysis of Over 6,000 Patients Treated On Prospective Studies. *Int J Radiat Oncol Biol Phys*, 104: 778-789, 2019.
105. Widmark, A, Gunnlaugsson, A, Beckman, L, Thellenberg-Karlsson, C, Hoyer, M, Lagerlund, M, Kindblom, J, Ginman, C, Johansson, B, Björnlinger, K, Seke, M, Agrup, M, Fransson, P, Tavelin, B, Norman, D, Zackrisson, B, Anderson, H, Kjellén, E, Franzén, L, Nilsson, P: Ultra-hypofractionated versus conventionally fractionated radiotherapy for prostate cancer: 5-year outcomes of the HYPO-RT-PC randomised, non-inferiority, phase 3 trial. *The Lancet*, 394: 385-395, 2019.
106. Brand, DH, Tree, AC, Ostler, P, van der Voet, H, Loblaw, A, Chu, W, Ford, D, Tolan, S, Jain, S, Martin, A, Staffurth, J, Camilleri, P, Kancherla, K, Frew, J, Chan, A, Dayes, IS, Henderson, D, Brown, S, Cruickshank, C, Burnett, S,

- Duffton, A, Griffin, C, Hinder, V, Morrison, K, Naismith, O, Hall, E, van As, N, Dodds, D, Lartigau, E, Patton, S, Thompson, A, Winkler, M, Wells, P, Lymberiou, T, Saunders, D, Vilarino-Varela, M, Vavassis, P, Tsakiridis, T, Carlson, R, Rodrigues, G, Tanguay, J, Iqbal, S, Winkler, M, Morgan, S, Mihai, A, Li, A, Din, O, Panades, M, Wade, R, Rimmer, Y, Armstrong, J, Panades, M, Oommen, N: Intensity-modulated fractionated radiotherapy versus stereotactic body radiotherapy for prostate cancer (PACE-B): acute toxicity findings from an international, randomised, open-label, phase 3, non-inferiority trial. *The Lancet Oncology*, 20: 1531-1543, 2019.
107. Mohler, JL, Antonarakis, ES, Armstrong, AJ, D'Amico, AV, Davis, BJ, Dorff, T, Eastham, JA, Enke, CA, Farrington, TA, Higano, CS, Horwitz, EM, Hurwitz, M, Ippolito, JE, Kane, CJ, Kuettel, MR, Lang, JM, McKenney, J, Netto, G, Penson, DF, Plimack, ER, Pow-Sang, JM, Pugh, TJ, Richey, S, Roach, M, Rosenfeld, S, Schaeffer, E, Shabsigh, A, Small, EJ, Spratt, DE, Srinivas, S, Tward, J, Sheard, DA, Freedman-Cass, DA: Prostate Cancer, Version 2.2019, NCCN Clinical Practice Guidelines in Oncology. *J Natl Compr Canc Netw*, 17: 479-505, 2019.
108. Morgan, SC, Hoffman, K, Loblaw, DA, Buyyounouski, MK, Patton, C, Barocas, D, Bentzen, S, Chang, M, Efstathiou, J, Greany, P, Halvorsen, P, Koontz, BF, Lawton, C, Leyrer, CM, Lin, D, Ray, M, Sandler, H: Hypofractionated Radiation Therapy for Localized Prostate Cancer: An ASTRO, ASCO, and AUA Evidence-Based Guideline. *J Clin Oncol*: JCO1801097, 2018.
109. Zhang, Y, Yue, N, Su, MY, Liu, B, Ding, Y, Zhou, Y, Wang, H, Kuang, Y, Nie, K: Improving CBCT Quality to CT Level using Deep-Learning with Generative Adversarial Network. *Med Phys*, 2020.
110. Chen, L, Liang, X, Shen, C, Jiang, S, Wang, J: Synthetic CT generation from CBCT images via deep learning. *Med Phys*, 47: 1115-1125, 2020.
111. Liang, X, Chen, L, Nguyen, D, Zhou, Z, Gu, X, Yang, M, Wang, J, Jiang, S: Generating synthesized computed tomography (CT) from cone-beam computed tomography (CBCT) using CycleGAN for adaptive radiation therapy. *Phys Med Biol*, 64: 125002, 2019.
112. Barateau, A, Garlopeau, C, Cugny, A, De Figueiredo, BH, Dupin, C, Caron, J, Antoine, M: Dose calculation accuracy of different image value to density tables for cone-beam CT planning in head & neck and pelvic localizations. *Phys Med*, 31: 146-151, 2015.
113. Liu, Y, Lei, Y, Wang, Y, Shafai-Erfani, G, Wang, T, Tian, S, Patel, P, Jani, AB, McDonald, M, Curran, WJ, Liu, T, Zhou, J, Yang, X: Evaluation of a deep learning-based pelvic synthetic CT generation technique for MRI-based prostate proton treatment planning. *Phys Med Biol*, 64: 205022, 2019.
114. Maspero, M, Savenije, MHF, Dinkla, AM, Seevinck, PR, Intven, MPW, Jurgentliemk-Schulz, IM, Kerkmeijer, LGW, van den Berg, CAT: Dose evaluation of fast synthetic-CT generation using a generative adversarial network for general pelvis MR-only radiotherapy. *Phys Med Biol*, 63: 185001, 2018.
115. Goodfellow, I, Pouget-Abadie, J, Mirza, M, Xu, B, Warde-Farley, D, Ozair, S, Courville, A, Bengio, Y: Generative Adversarial Networks. *Advances in Neural Information Processing Systems*, 3, 2014.
116. Zhu, J, Park, T, Isola, P, Efros, AA: Unpaired Image-to-Image Translation Using Cycle-Consistent Adversarial Networks. *2017 IEEE International Conference on Computer Vision (ICCV)*. 2017 pp 2242-2251.
117. Tian, C, Fei, L, Zheng, W, Xu, Y, Zuo, W, Lin, CW: Deep learning on image denoising: An overview. *Neural Netw*, 131: 251-275, 2020.

118. Li, Y, Zhu, J, Liu, Z, Teng, J, Xie, Q, Zhang, L, Liu, X, Shi, J, Chen, L: A preliminary study of using a deep convolution neural network to generate synthesized CT images based on CBCT for adaptive radiotherapy of nasopharyngeal carcinoma. *Phys Med Biol*, 64: 145010, 2019.
119. Xu, J, Han, X, Hibbard, L, Willcut, V: A Deep Convolutional Neural Network for Cone-Beam CT Artefacts Reduction: SU-K-FS4-14. *Medical Physics*, 44: 3011-3012, 2017.
120. Cohen, J, Honari, S: Distribution Matching Losses Can Hallucinate Features in Medical Image Translation. In, 2018, pp 529-536.
121. Kida, S, Kaji, S, Nawa, K, Imae, T, Nakamoto, T, Ozaki, S, Ohta, T, Nozawa, Y, Nakagawa, K: Visual enhancement of Cone-beam CT by use of CycleGAN. *Med Phys*, 47: 998-1010, 2020.
122. Wolterink, JM, Dinkla, AM, Savenije, MHF, Seevinck, PR, van den Berg, CAT, Išgum, I: Deep MR to CT Synthesis Using Unpaired Data. Cham, Springer International Publishing, 2017 pp 14-23.
123. Eckl, M, Hoppen, L, Sarria, GR, Boda-Heggemann, J, Simeonova-Chergou, A, Steil, V, Giordano, FA, Fleckenstein, J: Evaluation of a cycle-generative adversarial network-based cone-beam CT to synthetic CT conversion algorithm for adaptive radiation therapy. *Physica Medica*, 80: 308-316, 2020.
124. Nomura, Y, Xu, Q, Shirato, H, Shimizu, S, Xing, L: Projection-domain scatter correction for cone beam computed tomography using a residual convolutional neural network. *Med Phys*, 46: 3142-3155, 2019.
125. Elekta AB, S, CMS: Admire guide whitepaper. 2017.
126. Elekta AB, S, Software, C: ABAS: Intra-Patient Deformable Image Registration for Adaptive Radiotherapy – A White Paper. 2014.
127. Dong, X, Lei, Y, Wang, T, Thomas, M, Tang, L, Curran, WJ, Liu, T, Yang, X: Automatic multiorgan segmentation in thorax CT images using U-net-GAN. *Med Phys*, 46: 2157-2168, 2019.
128. Hussein, M, Clark, CH, Nisbet, A: Challenges in calculation of the gamma index in radiotherapy - Towards good practice. *Phys Med*, 36: 1-11, 2017.
129. Eckl, M, Sarria, GR, Springer, S, Willam, M, Ruder, AM, Steil, V, Ehmann, M, Wenz, F, Fleckenstein, J: Dosimetric benefits of daily treatment plan adaptation for prostate cancer stereotactic body radiotherapy. *Radiat Oncol*, 16: 145, 2021.
130. PACE: International randomised study of prostatectomy vs stereotactic body radiotherapy (SBRT) and conventional radiotherapy vs SBRT for organ-confined prostate cancer. <https://www.icracuk/our-research/centres-and-collaborations/centres-at-the-icr/clinical-trials-and-statistics-unit/clinical-trials/pace>, Accessed: August 30th, 2020.
131. Schmitt, D, Blanck, O, Gauer, T, Fix, MK, Brunner, TB, Fleckenstein, J, Loutfi-Krauss, B, Manser, P, Werner, R, Wilhelm, ML, Baus, WW, Moustakis, C: Technological quality requirements for stereotactic radiotherapy : Expert review group consensus from the DGMP Working Group for Physics and Technology in Stereotactic Radiotherapy. *Strahlenther Onkol*, 196: 421-443, 2020.
132. Guckenberger, M, Baus, WW, Blanck, O, Combs, SE, Debus, J, Engenhardt-Cabillic, R, Gauer, T, Grosu, AL, Schmitt, D, Tanadini-Lang, S, Moustakis, C: Definition and quality requirements for stereotactic radiotherapy: consensus statement from the DEGRO/DGMP Working Group Stereotactic Radiotherapy and Radiosurgery. *Strahlenther Onkol*, 196: 417-420, 2020.
133. Elekta AB, S: Monaco v5.19.03 Research User Guide Supplement. 2017.
134. Ahunbay, EE, Li, XA: Gradient maintenance: A new algorithm for fast online replanning. *Med Phys*, 42: 2863-2876, 2015.

135. Ahunbay, EE, Ates, O, Li, XA: An online replanning method using warm start optimization and aperture morphing for flattening-filter-free beams. *Med Phys*, 43: 4575, 2016.
136. Elekta AB, S: Warm Start Optimization, Technical Reference, v13c. 2017.
137. Bohsung, J, Gillis, S, Arrans, R, Bakai, A, De Wagter, C, Knoos, T, Mijnheer, BJ, Paiusco, M, Perrin, BA, Welleweerd, H, Williams, P: IMRT treatment planning:- a comparative inter-system and inter-centre planning exercise of the ESTRO QUASIMODO group. *Radiother Oncol*, 76: 354-361, 2005.
138. Sherer, MV, Lin, D, Elguindi, S, Duke, S, Tan, LT, Cacicedo, J, Dahele, M, Gillespie, EF: Metrics to evaluate the performance of auto-segmentation for radiation treatment planning: A critical review. *Radiother Oncol*, 160: 185-191, 2021.
139. Oelfke, U, Tücking, T, Nill, S, Seeber, A, Hesse, B, Huber, P, Thilmann, C: Linac-integrated kV-cone beam CT: technical features and first applications. *Med Dosim*, 31: 62-70, 2006.
140. Bell, K, Heitfeld, M, Licht, N, Rube, C, Dzierma, Y: Influence of daily imaging on plan quality and normal tissue toxicity for prostate cancer radiotherapy. *Radiat Oncol*, 12: 7, 2017.
141. Oehler, C, Lang, S, Dimmerling, P, Bolesch, C, Kloeck, S, Tini, A, Glanzmann, C, Najafi, Y, Studer, G, Zwahlen, DR: PTV margin definition in hypofractionated IGRT of localized prostate cancer using cone beam CT and orthogonal image pairs with fiducial markers. *Radiat Oncol*, 9: 229, 2014.
142. Kurz, C, Maspero, M, Savenije, MHF, Landry, G, Kamp, F, Pinto, M, Li, M, Parodi, K, Belka, C, Van den Berg, CAT: CBCT correction using a cycle-consistent generative adversarial network and unpaired training to enable photon and proton dose calculation. *Phys Med Biol*, 2019.
143. Landry, G, Hansen, D, Kamp, F, Li, M, Hoyle, B, Weller, J, Parodi, K, Belka, C, Kurz, C: Comparing Unet training with three different datasets to correct CBCT images for prostate radiotherapy dose calculations. *Phys Med Biol*, 64: 035011, 2019.
144. Fu, J, Yang, Y, Singhrao, K, Ruan, D, Chu, FI, Low, DA, Lewis, JH: Deep learning approaches using 2D and 3D convolutional neural networks for generating male pelvic synthetic computed tomography from magnetic resonance imaging. *Med Phys*, 46: 3788-3798, 2019.
145. Thummerer, A, Zaffino, P, Meijers, A, Marmitt, GG, Seco, J, Steenbakkens, R, Langendijk, JA, Both, S, Spadea, MF, Knopf, AC: Comparison of CBCT based synthetic CT methods suitable for proton dose calculations in adaptive proton therapy. *Phys Med Biol*, 65: 095002, 2020.
146. Nyholm, T, Jonsson, J, Soderstrom, K, Bergstrom, P, Carlberg, A, Frykholm, G, Behrens, CF, Geertsen, PF, Trepikas, R, Hanvey, S, Sadozye, A, Ansari, J, McCallum, H, Frew, J, McMenemin, R, Zackrisson, B: Variability in prostate and seminal vesicle delineations defined on magnetic resonance images, a multi-observer, -center and -sequence study. *Radiat Oncol*, 8: 126, 2013.
147. Fu, Y, Lei, Y, Wang, T, Tian, S, Patel, P, Jani, AB, Curran, WJ, Liu, T, Yang, X: Pelvic multi-organ segmentation on cone-beam CT for prostate adaptive radiotherapy. *Med Phys*, 47: 3415-3422, 2020.
148. Berenguer, R, de la Vara, V, Lopez-Honrubia, V, Nunez, AT, Rivera, M, Villas, MV, Sabater, S: The influence of the image registration method on the adaptive radiotherapy. A proof of the principle in a selected case of prostate IMRT. *Phys Med*, 45: 93-98, 2018.

149. Konig, L, Derksen, A, Papenberg, N, Haas, B: Deformable image registration for adaptive radiotherapy with guaranteed local rigidity constraints. *Radiat Oncol*, 11: 122, 2016.
150. Woerner, AJ, Choi, M, Harkenrider, MM, Roeske, JC, Surucu, M: Evaluation of Deformable Image Registration-Based Contour Propagation From Planning CT to Cone-Beam CT. *Technol Cancer Res Treat*: 1533034617697242, 2017.
151. Schreier, J, Genghi, A, Laaksonen, H, Morgas, T, Haas, B: Clinical evaluation of a full-image deep segmentation algorithm for the male pelvis on cone-beam CT and CT. *Radiother Oncol*, 145: 1-6, 2020.
152. Gardner, SJ, Wen, N, Kim, J, Liu, C, Pradhan, D, Aref, I, Cattaneo, R, Vance, S, Movsas, B, Chetty, IJ, Elshaikh, MA: Contouring variability of human- and deformable-generated contours in radiotherapy for prostate cancer. *Phys Med Biol*, 60: 4429-4447, 2015.
153. Liang, X, Bibault, JE, Leroy, T, Escande, A, Zhao, W, Chen, Y, Buyyounouski, MK, Hancock, SL, Bagshaw, H, Xing, L: Automated contour propagation of the prostate from pCT to CBCT images via deep unsupervised learning. *Med Phys*, 48: 1764-1770, 2021.
154. Brion, E, Leger, J, Barragan-Montero, AM, Meert, N, Lee, JA, Macq, B: Domain adversarial networks and intensity-based data augmentation for male pelvic organ segmentation in cone beam CT. *Comput Biol Med*, 131: 104269, 2021.
155. Iglesias, JE, Sabuncu, MR: Multi-atlas segmentation of biomedical images: A survey. *Medical Image Analysis*, 24: 205-219, 2015.
156. Zhang, J, Ahunbay, E, Li, XA: Technical Note: Acceleration of online adaptive replanning with automation and parallel operations. *Med Phys*, 45: 4370-4376, 2018.
157. Cha, E, Elguindi, S, Onochie, I, Gorovets, D, Deasy, JO, Zelefsky, M, Gillespie, EF: Clinical implementation of deep learning contour autosegmentation for prostate radiotherapy. *Radiother Oncol*, 159: 1-7, 2021.
158. Vaassen, F, Hazelaar, C, Vaniqui, A, Gooding, M, van der Heyden, B, Canters, R, van Elmpt, W: Evaluation of measures for assessing time-saving of automatic organ-at-risk segmentation in radiotherapy. *Physics and Imaging in Radiation Oncology*, 13: 1-6, 2020.
159. Nikolov, S, Blackwell, S, Zverovitch, A, Mendes, R, Livne, M, De Fauw, J, Patel, Y, Meyer, C, Askham, H, Romera-Paredes, B, Kelly, C, Karthikesalingam, A, Chu, C, Carnell, D, Boon, C, D'Souza, D, Moinuddin, SA, Garie, B, McQuinlan, Y, Ireland, S, Hampton, K, Fuller, K, Montgomery, H, Rees, G, Suleyman, M, Back, T, Hughes, CO, Ledsam, JR, Ronneberger, O: Clinically Applicable Segmentation of Head and Neck Anatomy for Radiotherapy: Deep Learning Algorithm Development and Validation Study. *J Med Internet Res*, 23: e26151, 2021.
160. Marchant, TE, Joshi, KD, Moore, CJ: Accuracy of radiotherapy dose calculations based on cone-beam CT: comparison of deformable registration and image correction based methods. *Phys Med Biol*, 63: 065003, 2018.
161. Dunlop, A, McQuaid, D, Nill, S, Murray, J, Poludniowski, G, Hansen, VN, Bhide, S, Nutting, C, Harrington, K, Newbold, K, Oelfke, U: Comparison of CT number calibration techniques for CBCT-based dose calculation. *Strahlenther Onkol*, 191: 970-978, 2015.
162. Onozato, Y, Kadoya, N, Fujita, Y, Arai, K, Dobashi, S, Takeda, K, Kishi, K, Umezawa, R, Matsushita, H, Jingu, K: Evaluation of on-board kV cone beam computed tomography-based dose calculation with deformable image

- registration using Hounsfield unit modifications. *Int J Radiat Oncol Biol Phys*, 89: 416-423, 2014.
163. Bird, D, Henry, AM, Sebag-Montefiore, D, Buckley, DL, Al-Qaisieh, B, Speight, R: A Systematic Review of the Clinical Implementation of Pelvic Magnetic Resonance Imaging-Only Planning for External Beam Radiation Therapy. *Int J Radiat Oncol Biol Phys*, 105: 479-492, 2019.
164. Tocco, BR, Kishan, AU, Ma, TM, Kerkmeijer, LGW, Tree, AC: MR-Guided Radiotherapy for Prostate Cancer. *Front Oncol*, 10: 616291, 2020.
165. Liu, Y, Lei, Y, Wang, T, Fu, Y, Tang, X, Curran, WJ, Liu, T, Patel, P, Yang, X: CBCT-based synthetic CT generation using deep-attention cycleGAN for pancreatic adaptive radiotherapy. *Med Phys*, 47: 2472-2483, 2020.
166. Uh, J, Wang, C, Acharya, S, Krasin, MJ, Hua, CH: Training a deep neural network coping with diversities in abdominal and pelvic images of children and young adults for CBCT-based adaptive proton therapy. *Radiother Oncol*, 160: 250-258, 2021.
167. Godley, A, Ahunbay, E, Peng, C, Li, XA: Accumulating daily-varied dose distributions of prostate radiation therapy with soft-tissue-based kV CT guidance. *J Appl Clin Med Phys*, 13: 3859, 2012.
168. Peng, C, Ahunbay, E, Chen, G, Anderson, S, Lawton, C, Li, XA: Characterizing interfraction variations and their dosimetric effects in prostate cancer radiotherapy. *Int J Radiat Oncol Biol Phys*, 79: 909-914, 2011.
169. Deutschmann, H, Kametrise, G, Steininger, P, Scherer, P, Scholler, H, Gaisberger, C, Mooslechner, M, Mitterlechner, B, Weichenberger, H, Fastner, G, Wurstbauer, K, Jeschke, S, Forstner, R, Sedlmayer, F: First clinical release of an online, adaptive, aperture-based image-guided radiotherapy strategy in intensity-modulated radiotherapy to correct for inter- and intrafractional rotations of the prostate. *Int J Radiat Oncol Biol Phys*, 83: 1624-1632, 2012.
170. Greco, C, Stroom, J, Vieira, S, Mateus, D, Cardoso, MJ, Soares, A, Pares, O, Pimentel, N, Louro, V, Nunes, B, Kociolek, J, Fuks, Z: Reproducibility and accuracy of a target motion mitigation technique for dose-escalated prostate stereotactic body radiotherapy. *Radiother Oncol*, 160: 240-249, 2021.
171. Yoon, S, Cao, M, Aghdam, N, Shabsovich, D, Kahlon, S, Ballas, L, Collins, S, Steinberg, ML, Kishan, AU: Prostate bed and organ-at-risk deformation: Prospective volumetric and dosimetric data from a phase II trial of stereotactic body radiotherapy after radical prostatectomy. *Radiother Oncol*, 148: 44-50, 2020.
172. Ates, O, Ahunbay, EE, Moreau, M, Li, XA: Technical Note: A fast online adaptive replanning method for VMAT using flattening filter free beams. *Med Phys*, 43: 2756-2764, 2016.
173. Thornqvist, S, Hysing, LB, Tuomikoski, L, Vestergaard, A, Tanderup, K, Muren, LP, Heijmen, BJ: Adaptive radiotherapy strategies for pelvic tumors - a systematic review of clinical implementations. *Acta Oncol*, 55: 943-958, 2016.
174. Thongphiew, D, Wu, QJ, Lee, WR, Chankong, V, Yoo, S, McMahon, R, Yin, FF: Comparison of online IGRT techniques for prostate IMRT treatment: adaptive vs repositioning correction. *Med Phys*, 36: 1651-1662, 2009.
175. Wahl, M, Descovich, M, Shugard, E, Pinnaduwege, D, Sudhyadhom, A, Chang, A, Roach, M, Gottschalk, A, Chen, J: Interfraction Anatomical Variability Can Lead to Significantly Increased Rectal Dose for Patients Undergoing Stereotactic Body Radiotherapy for Prostate Cancer. *Technol Cancer Res Treat*, 16: 178-187, 2017.

176. Battista, JJ, Johnson, C, Turnbull, D, Kempe, J, Bzdusek, K, Van Dyk, J, Bauman, G: Dosimetric and radiobiological consequences of computed tomography-guided adaptive strategies for intensity modulated radiation therapy of the prostate. *Int J Radiat Oncol Biol Phys*, 87: 874-880, 2013.
177. Laura Licon, A, Defoor, D, Ford, J, Crownover, R, Li, Y, Ha, C, Eng, T, Jones, W, Mavroidis, P, Papanikolaou, N, Stathakis, S: A quantitative measure for radiation treatment plan quality. *J buon*, 23: 1460-1466, 2018.
178. Akino, Y, Yoshioka, Y, Fukuda, S, Maruoka, S, Takahashi, Y, Yagi, M, Mizuno, H, Isohashi, F, Ogawa, K: Estimation of rectal dose using daily megavoltage cone-beam computed tomography and deformable image registration. *Int J Radiat Oncol Biol Phys*, 87: 602-608, 2013.
179. Chen, Z, Yang, Z, Wang, J, Hu, W: Dosimetric impact of different bladder and rectum filling during prostate cancer radiotherapy. *Radiat Oncol*, 11: 103, 2016.
180. Devlin, L, Dodds, D, Sadozye, A, McLoone, P, MacLeod, N, Lamb, C, Currie, S, Thomson, S, Duffton, A: Dosimetric impact of organ at risk daily variation during prostate stereotactic ablative radiotherapy. *Br J Radiol*, 93: 20190789, 2020.
181. Hargrave, C, Deegan, T, Poulsen, M, Bednarz, T, Harden, F, Mengersen, K: A feature alignment score for online cone-beam CT-based image-guided radiotherapy for prostate cancer. *Med Phys*, 45: 2898-2911, 2018.
182. Burton, A, Norvill, C, Ebert, MA: Predictive performance of an OVH-based treatment planning quality assurance model for prostate VMAT: Assessing dependence on training cohort size and composition. *Med Dosim*, 44: 315-323, 2019.
183. Janssen, TM, Kusters, M, Wang, Y, Wortel, G, Monshouwer, R, Damen, E, Petit, SF: Independent knowledge-based treatment planning QA to audit Pinnacle autoplanning. *Radiother Oncol*, 133: 198-204, 2019.
184. Wall, PDH, Carver, RL, Fontenot, JD: An improved distance-to-dose correlation for predicting bladder and rectum dose-volumes in knowledge-based VMAT planning for prostate cancer. *Phys Med Biol*, 63: 015035, 2018.
185. Hernandez, V, Hansen, CR, Widesott, L, Back, A, Canters, R, Fusella, M, Gotstedt, J, Jurado-Bruggeman, D, Mukumoto, N, Kaplan, LP, Koniarova, I, Piotrowski, T, Placidi, L, Vaniqui, A, Jornet, N: What is plan quality in radiotherapy? The importance of evaluating dose metrics, complexity, and robustness of treatment plans. *Radiother Oncol*, 153: 26-33, 2020.
186. Kontaxis, C, Bol, GH, Kerkmeijer, LGW, Lagendijk, JJW, Raaymakers, BW: Fast online replanning for interfraction rotation correction in prostate radiotherapy. *Med Phys*, 44: 5034-5042, 2017.
187. Kida, S, Nakamoto, T, Nakano, M, Nawa, K, Haga, A, Kotoku, J, Yamashita, H, Nakagawa, K: Cone Beam Computed Tomography Image Quality Improvement Using a Deep Convolutional Neural Network. *Cureus*, 10: e2548, 2018.
188. Li, M, Ballhausen, H, Hegemann, NS, Reiner, M, Tritschler, S, Gratzke, C, Manapov, F, Corradini, S, Ganswindt, U, Belka, C: Comparison of prostate positioning guided by three-dimensional transperineal ultrasound and cone beam CT. *Strahlenther Onkol*, 193: 221-228, 2017.
189. Sihono, DSK, Ehmann, M, Heitmann, S, von Swietochowski, S, Grimm, M, Boda-Heggemann, J, Lohr, F, Wenz, F, Wertz, H: Determination of Intrafraction Prostate Motion During External Beam Radiation Therapy With a Transperineal 4-Dimensional Ultrasound Real-Time Tracking System. *Int J Radiat Oncol Biol Phys*, 101: 136-143, 2018.
190. Lovelock, DM, Messineo, AP, Cox, BW, Kollmeier, MA, Zelefsky, MJ: Continuous monitoring and intrafraction target position correction during treatment improves

- target coverage for patients undergoing SBRT prostate therapy. *Int J Radiat Oncol Biol Phys*, 91: 588-594, 2015.
191. Azcona, JD, Li, R, Mok, E, Hancock, S, Xing, L: Automatic prostate tracking and motion assessment in volumetric modulated arc therapy with an electronic portal imaging device. *Int J Radiat Oncol Biol Phys*, 86: 762-768, 2013.
 192. Hewson, EA, Nguyen, DT, O'Brien, R, Kim, JH, Montanaro, T, Moodie, T, Greer, PB, Hardcastle, N, Eade, T, Kneebone, A, Hruby, G, Hayden, AJ, Turner, S, Siva, S, Tai, KH, Hunter, P, Sams, J, Poulsen, PR, Booth, JT, Martin, J, Keall, PJ: The accuracy and precision of the KIM motion monitoring system used in the multi-institutional TROG 15.01 Stereotactic Prostate Ablative Radiotherapy with KIM (SPARK) trial. *Med Phys*, 46: 4725-4737, 2019.
 193. Vanhanen, A, Poulsen, P, Kapanen, M: Dosimetric effect of intrafraction motion and different localization strategies in prostate SBRT. *Phys Med*, 75: 58-68, 2020.
 194. Liu, H, Wu, Q: Evaluations of an adaptive planning technique incorporating dose feedback in image-guided radiotherapy of prostate cancer. *Med Phys*, 38: 6362-6370, 2011.
 195. Lee, H, Kim, H, Kwak, J, Kim, YS, Lee, SW, Cho, S, Cho, B: Fluence-map generation for prostate intensity-modulated radiotherapy planning using a deep-neural-network. *Sci Rep*, 9: 15671, 2019.
 196. Osman, AFI, Maalej, NM: Applications of machine and deep learning to patient-specific IMRT/VMAT quality assurance. *J Appl Clin Med Phys*, 22: 20-36, 2021.
 197. Li, XA, Wu, Q, Orton, CG: Point/Counterpoint. Online adaptive planning for prostate cancer radiotherapy is necessary and ready now. *Med Phys*, 41: 080601, 2014.
 198. Fiorino, C, Cozzarini, C, Passoni, P: The promise of adaptive radiotherapy for pelvic tumors: "too high cost for too little result" or "a low cost for a significant result"? *Acta Oncol*, 55: 939-942, 2016.
 199. Ghilezan, M, Yan, D, Martinez, A: Adaptive radiation therapy for prostate cancer. *Semin Radiat Oncol*, 20: 130-137, 2010.
 200. Fast, MF, Kamerling, CP, Ziegenhein, P, Menten, MJ, Bedford, JL, Nill, S, Oelfke, U: Assessment of MLC tracking performance during hypofractionated prostate radiotherapy using real-time dose reconstruction. *Phys Med Biol*, 61: 1546-1562, 2016.
 201. Jurado-Bruggeman, D, Hernandez, V, Saez, J, Navarro, D, Pino, F, Martinez, T, Alayrach, ME, Ailleres, N, Melero, A, Jornet, N: Multi-centre audit of VMAT planning and pre-treatment verification. *Radiother Oncol*, 124: 302-310, 2017.
 202. Crijns, W, Defraene, G, Van Herck, H, Depuydt, T, Haustermans, K, Maes, F, Van den Heuvel, F: Online adaptation and verification of VMAT. *Med Phys*, 42: 3877-3891, 2015.
 203. Esposito, M, Villaggi, E, Bresciani, S, Cilla, S, Falco, MD, Garibaldi, C, Russo, S, Talamonti, C, Stasi, M, Mancosu, P: Estimating dose delivery accuracy in stereotactic body radiation therapy: A review of in-vivo measurement methods. *Radiother Oncol*, 149: 158-167, 2020.
 204. Defoor, DL, Vazquez-Quino, LA, Mavroidis, P, Papanikolaou, N, Stathakis, S: Anatomy-based, patient-specific VMAT QA using EPID or MLC log files. *J Appl Clin Med Phys*, 16: 5283, 2015.
 205. Rozendaal, RA, Mijnheer, BJ, Hamming-Vrieze, O, Mans, A, van Herk, M: Impact of daily anatomical changes on EPID-based in vivo dosimetry of VMAT treatments of head-and-neck cancer. *Radiother Oncol*, 116: 70-74, 2015.

206. Tyagi, N, Yang, K, Gersten, D, Yan, D: A real time dose monitoring and dose reconstruction tool for patient specific VMAT QA and delivery. *Med Phys*, 39: 7194-7204, 2012.
207. Hirashima, H, Nakamura, M, Miyabe, Y, Uto, M, Nakamura, K, Mizowaki, T: Monitoring of mechanical errors and their dosimetric impact throughout the course of non-coplanar continuous volumetric-modulated arc therapy. *Radiat Oncol*, 13: 27, 2018.

7 APPENDIX

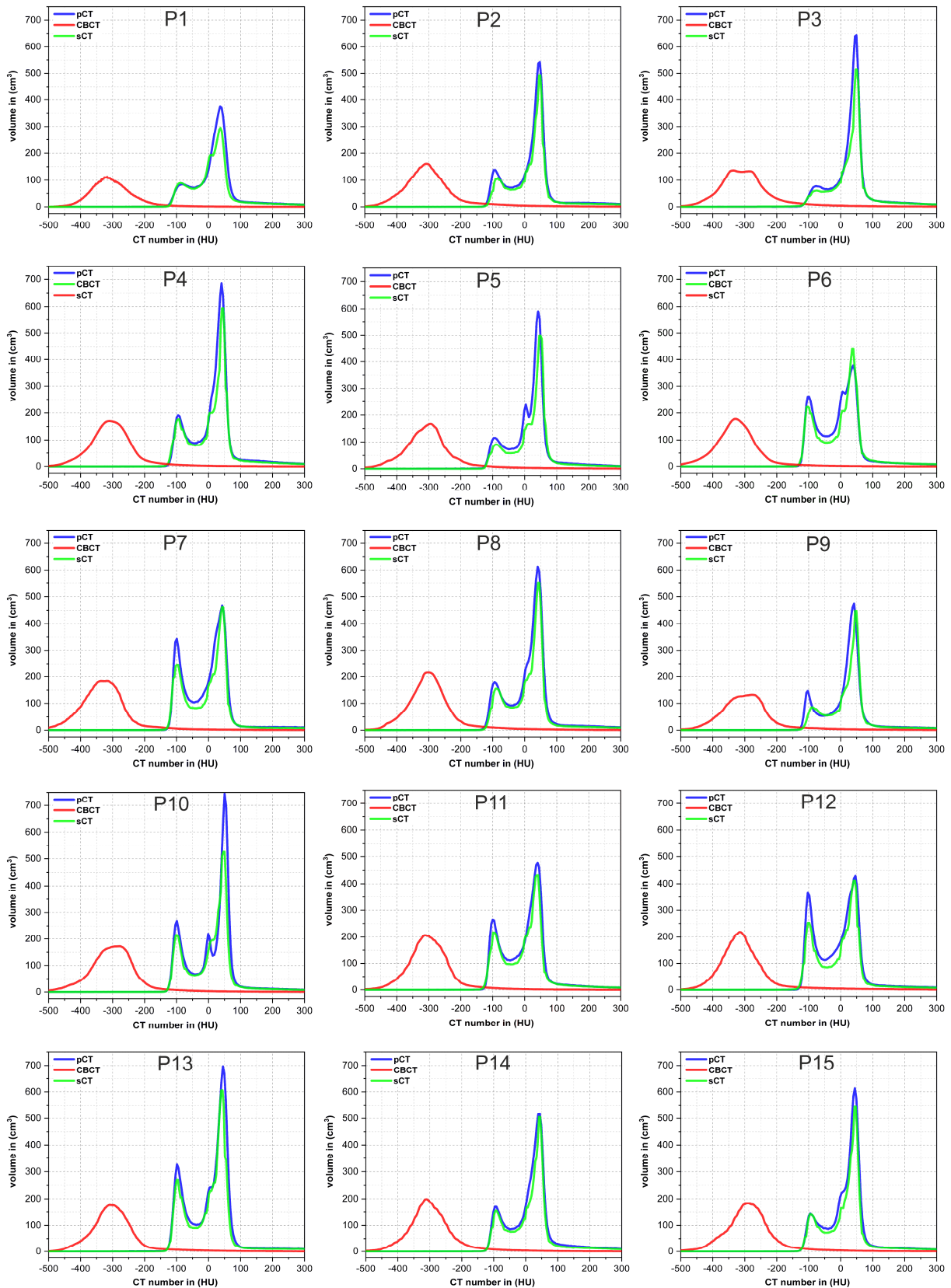


Figure 7.1: Intensity-volume-histograms of 15 prostate cancer patients (referred to as P1-P15), each including plots for the planning CT (blue), CBCT (red) and sCT (green). Distributions were generated for the CBCT body contour VOI minus a 15mm margin.

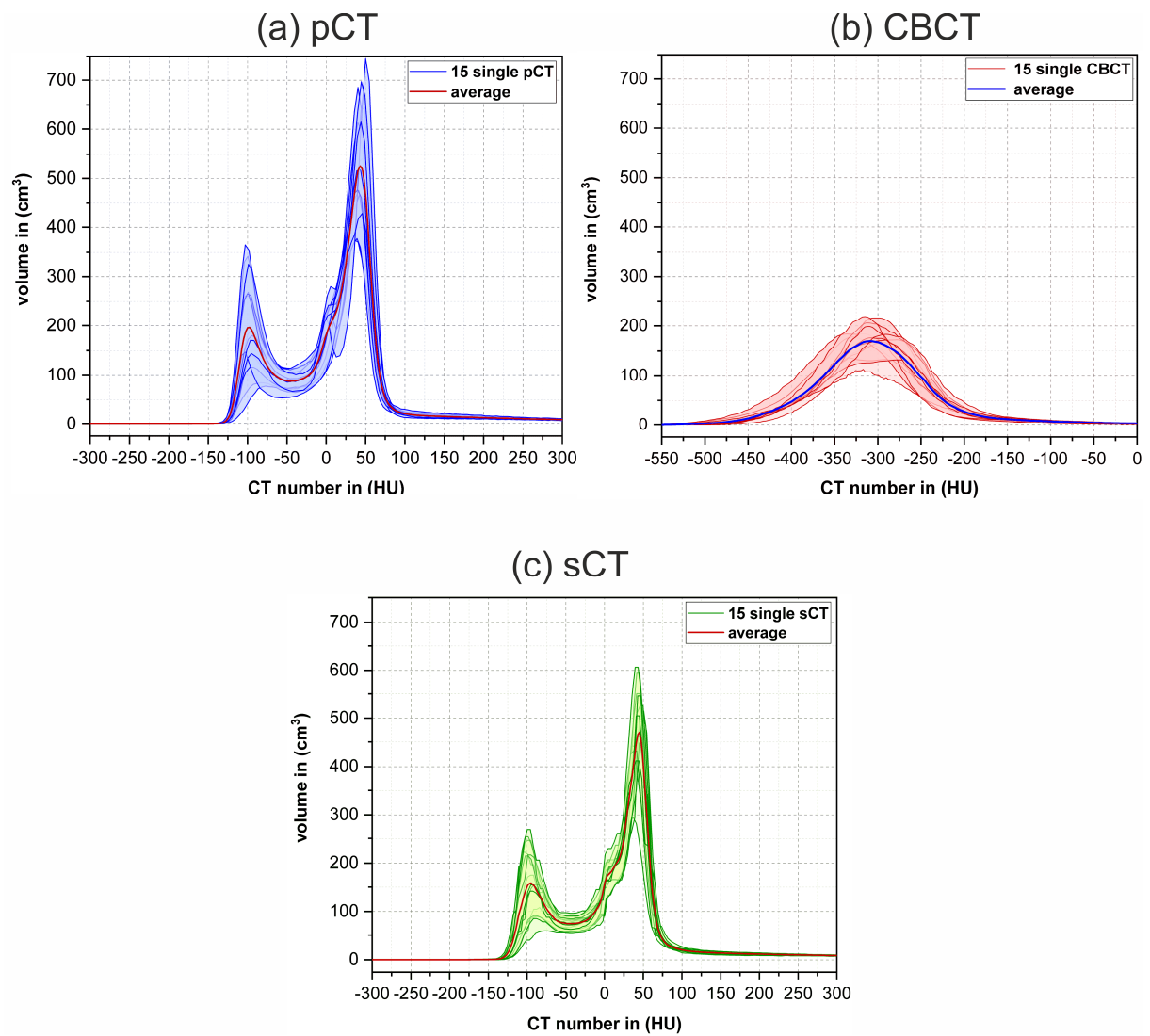


Figure 7.2: Range plots of the intensity-volume-histograms for the planning CT (a), CBCT (b) and sCT (c). Average lines were based on the collective of 15 prostate cancer patients. Shaded areas denote the range between the minimum and maximum points of every included single plot. Distributions were generated for the CBCT body contour VOI minus a 15mm margin.

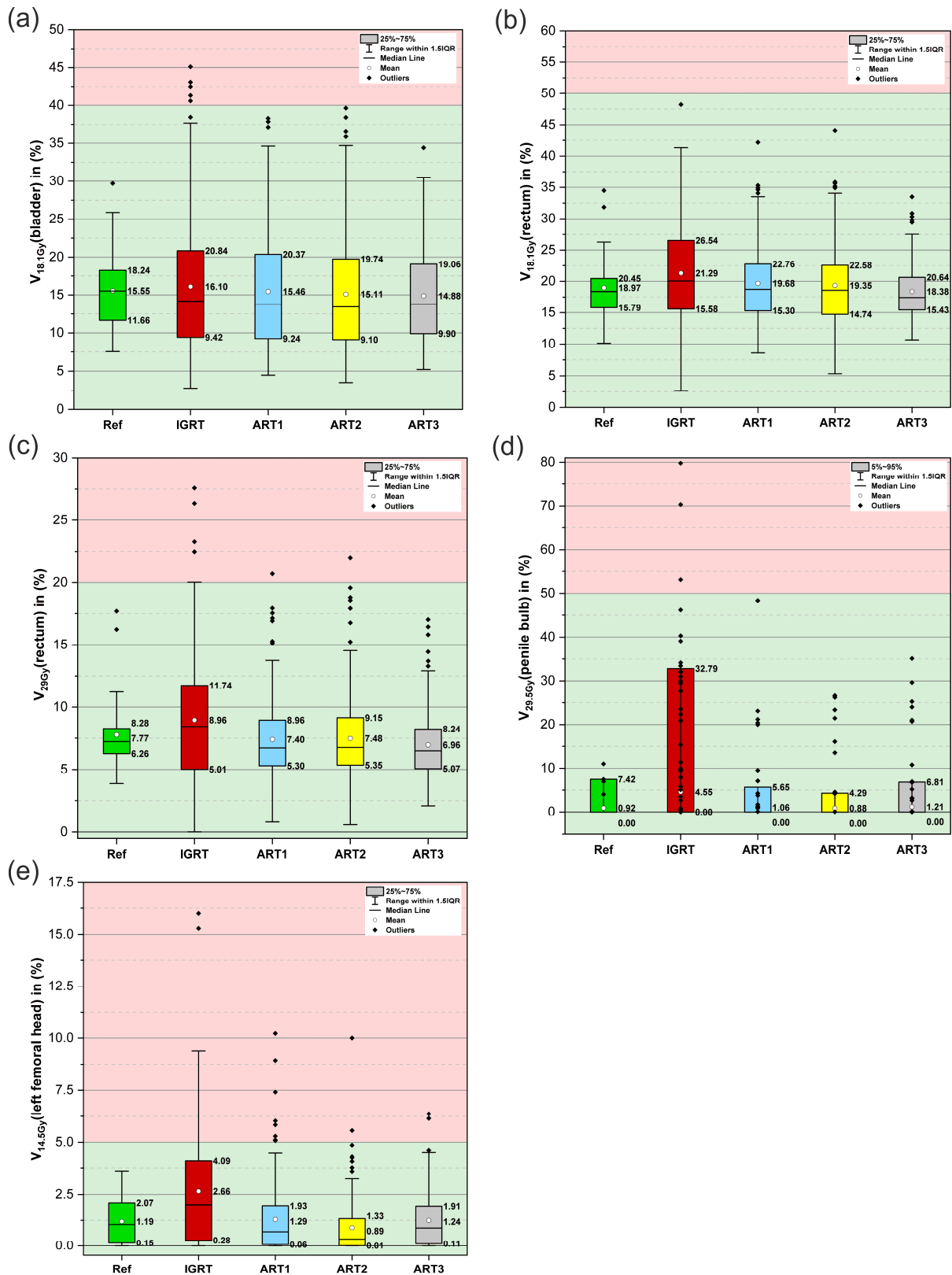


Figure 7.3: Boxplots of five additional dose-volume criteria for the bladder ((a)), rectum ((b)-(c)), penile bulb (d), and left femoral head (e) on the planning CT (Ref) and sCT (IGRT, ART1, ART2 and ART3 approaches). Whiskers denote the data within 1.5 times of the interquartile range (IQR) based on the 32 plans for the reference and 160 for the four adaptation approaches. Since the majority of results for the penile bulb criterion were located around 0, the IQR was exclusively adapted to 5%-95%. Background colors indicate optimal (green), acceptable (yellow) and unacceptable (red) results according to the PACE-C treatment planning guideline.

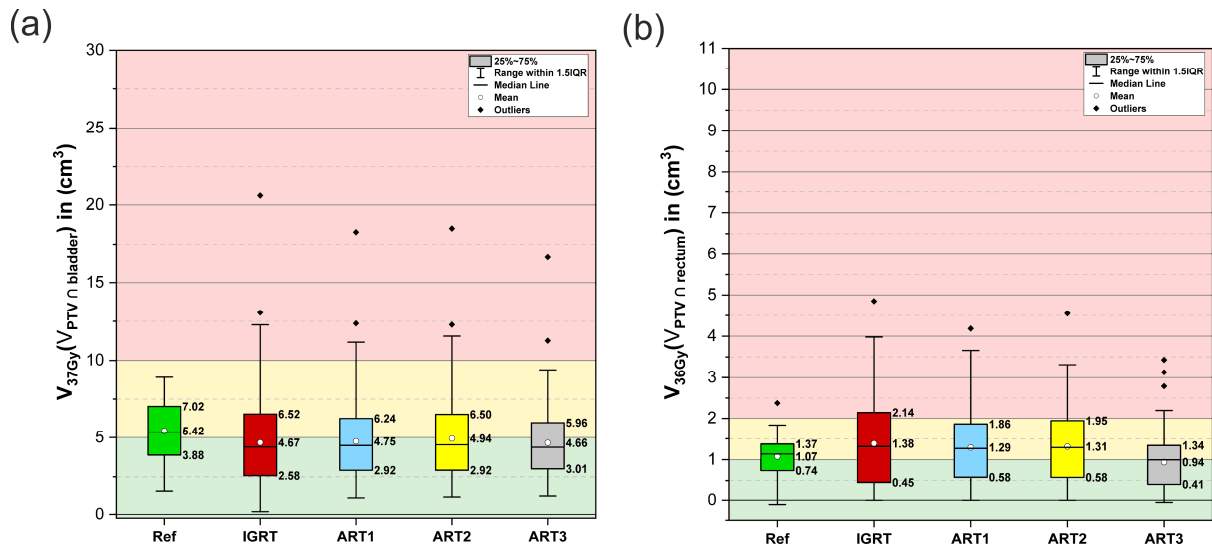


Figure 7.4: Boxplots of the two dose-volume criteria for the $V_{PTV \cap bladder}$ ((a)) and $V_{PTV \cap rectum}$ ((b)) on the planning CT (Ref) and sCT (IGRT, ART1, ART2 and ART3 approaches). Whiskers denote the data within 1.5 times of the interquartile range (IQR) based on the 32 plans for the reference and 160 for the four adaptation approaches. Background colors indicate optimal (green), acceptable (yellow) and unacceptable (red) results according to the PACE-C treatment planning guideline.

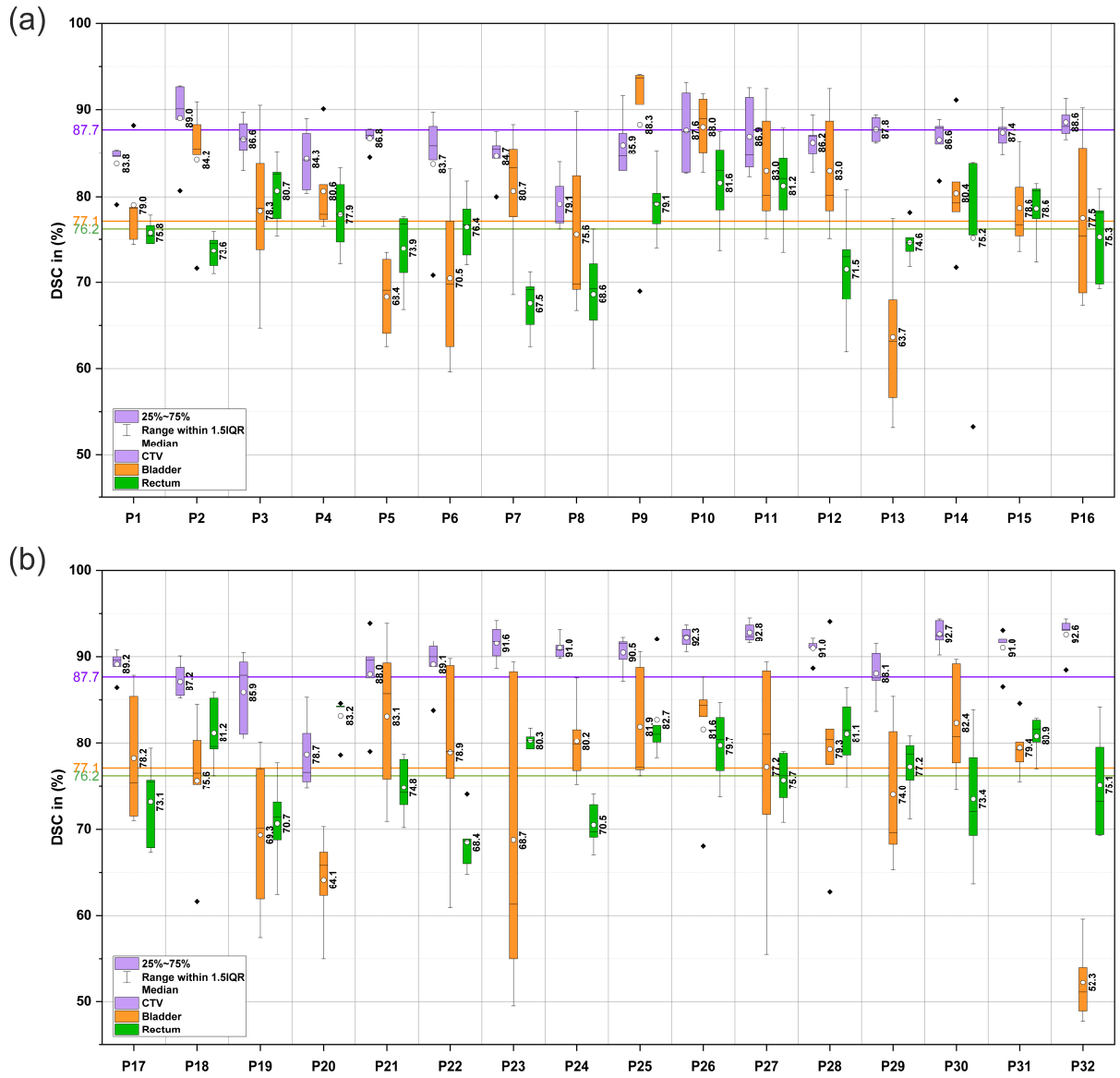


Figure 7.5: Dice similarity coefficient (DSC) of the CTV (purple), bladder (orange) and the rectum (green) for Patients P1-P16 (panel (a)) and P17-32 (panel (b)). Boxplots denote the IQR and whiskers a range of 1.5IQR. Mean results of the three organ structures were 87.7%, 77.1% and 76.2%, as indicated by reference lines.

8 CURRICULUM VITAE

PERSONAL INFORMATION

Name: Miriam Eckl
Date of birth: 24.08.1992
Place of birth: Ludwigshafen am Rhein, Germany
Marital status: single
Nationality: German

EDUCATION

08/1999 – 06/2002 Primary school (Mozartschule Rheingönheim, Ludwigshafen)
08/2002 – 03/2010 Secondary school (Carl-Bosch-Gymnasium, Ludwigshafen)
German university entrance certificate (Abitur): 12.03.2010
(Grade: 1.0)
08/2010 – 02/2011 Media and communication studies, University of Mannheim
04/2011 – 08/2016 Biophysics (German diploma), Technical University of
Kaiserslautern
Thesis title: „Aufbau eines ex-vivo Modells der perfundierten
Schweineniere zur Untersuchung von Laserlicht-Gewebe-
Wechselwirkung und im Vergleich zu einer HF-
Elektrokoagulation“
Degree: Dipl.-Biophys. (Grade: 1.3, 06.06.2016)
12/2016 – present Academic employee, Department of Radiation Oncology,
University Medical Center Mannheim
04/2017 – present Teacher for medical assistants and dosimetrists, UMM
Academy, University Medical Center Mannheim
07/2018 – present PhD student (*doctor scientiarum humanarum*)
06/2019 – present State-certified medical physicist

9 OWN PUBLICATIONS

Journal Articles

1. Eckl, M, Sarria, GR, Springer, S, Willam, M, Ruder, AM, Steil, V, Ehmann, M, Wenz, F, Fleckenstein, J: Dosimetric benefits of daily treatment plan adaptation for prostate cancer stereotactic body radiotherapy. *Radiat Oncol*, 16: 145, 2021
2. Eckl, M*, Hoppen, L*, Sarria, GR, Boda-Heggemann, J, Simeonova-Chergou, A, Steil, V, Giordano, FA, Fleckenstein, J: Evaluation of a cycle-generative adversarial network-based cone-beam CT to synthetic CT conversion algorithm for adaptive radiation therapy. *Physica Medica*, 80: 308-316, 2020 (*: first and second author contributed equally to this work)
3. Sekar, Y, Thoelking, J, Eckl, M, Kalichava, I, Sihono, DSK, Lohr, F, Wenz, F, Wertz, H: Characterization and clinical evaluation of a novel 2D detector array for conventional and flattening filter free (FFF) IMRT pre-treatment verification. *Z Med Phys*, 28: 134-141, 2018.

Posters and conference talks

1. Eckl, M, Sarria, GR, Steil, V, Ehmann, M, Fleckenstein, J: Dosimetric benefits of daily treatment plan adaptation for prostate cancer stereotactic body radiotherapy based on synthetic cone-beam CT. Talk at the 21st Asia-Oceania Congress of Medical Physics (AOCMP), Dhaka, Bangladesh, December 2021
2. Eckl, M, Sarria, GR, Springer, S, Willam, M, Ruder, AM, Steil, V, Ehmann, M, Wenz, F, Fleckenstein, J: Dosimetric benefits of daily treatment plan adaptation for prostate cancer stereotactic body radiotherapy based on synthetic cone-beam CT. Oral communication at the joint conference of the ÖGMP, DGMP and SGSMP, virtual event, September 2021, ISBN: 978-3-948023-16-4
3. Willam, W, Eckl, M, Schneider, F, Fleckenstein, J: Automation of dose recalculation based on daily imaging and treatment logfiles. Poster at the joint conference of the ÖGMP, DGMP and SGSMP, virtual event, September 2021, ISBN: 978-3-948023-16-4
4. Eckl, M, Hoppen, L, Sarria, GR, Boda-Heggemann, J, Simeonova-Chergou, A, Steil, V, Giordano, FA, Fleckenstein, J: Evaluation of a cycle-generative adversarial network-based synthetic cone-beam CT generation method for adaptive radiation therapy and daily treatment planning. Oral communication at the 3rd European congress of medical physics (ECMP), virtual event, June 2021
5. Eckl, M, Sarria, GR, Steil, V, Wenz, F, Fleckenstein, J: Implementation of adaptive radiation therapy for prostate cancer. Talk at the 15th Sino-German radiation oncology symposium, virtual event, March 2021
6. Eckl, M, Hoppen, L, Sarria, GR, Steil, V, Wenz, F, Fleckenstein, J: Clinical applications of adaptive radiotherapy based on CBCT. Talk at the BIR annual radiotherapy and oncology meeting, virtual event, March 2021

7. Hoppen, L, Eckl, M, Sarria, GR, Boda-Heggemann, J, Simeonova-Chergou, A, Steil, V, Giordano, FA, Fleckenstein, J: Auswertung der Genauigkeit einer künstlichen Intelligenz-basierten Methode zur Erstellung synthetischer CTs für die adaptive Strahlentherapie. Poster at the 51. DGMP conference, virtual event, 2020, ISBN 978-3-948023-10-2
8. Willam, M, Eckl, M, Ehmann, M, Schneider, F, Fleckenstein, J: Ein Verfahren zur automatisierten Dosisnachberechnung aus Linearbeschleuniger-Protokolldaten. Poster at the 51st DGMP conference, virtual event, 2020, ISBN 978-3-948023-10-2
9. Hoppen, L, Simeonova-Chergou, A, Jahnke, A, Eckl, M, Boda-Heggemann, J, Steil, V, Wenz, F, Wertz, HJ, Fleckenstein, J: Verfahren zur Bestimmung von Elektronendichteverteilungen auf Cone-Beam-CTs (CBCT) für die adaptive Strahlentherapie der Lunge. Poster at the 49. DGMP conference, Nürnberg, 2018, ISBN: 978-3-9816002-5-4
10. Eckl, M, Jahnke, A, Fleckenstein, J, Schneider, F, Kalichava, I, Siebenlist, K, Wenz, F, Wertz, HJ: Adaptive Strahlentherapie der Prostata: Evaluation der Gesamtbehandlungsqualität unter Berücksichtigung dosimetrischer Schwankungen (Linac-Output) und Organdeformationen. Poster at the 24th conference of the "Deutsche Gesellschaft für Radioonkologie" (DEGRO), Leipzig, 2018, DOI: 10.1007/s00066-018-1301-7
11. Kalichava, I, Eckl, M, Wenz, F, Wertz, HJ: Verification and validation of a transmission detector for linear accelerator quality assurance. Poster at the 24th conference of the DEGRO, Leipzig, 2018, DOI: 10.1007/s00066-018-1301-7
12. Kalichava, I, Eckl, M, Wenz, F, Wertz, H: Investigation of the fluence correction method for COMPASS. Poster at the 24th conference of the DEGRO, Leipzig, 2018, DOI: 10.1007/s00066-018-1301-7
13. Ohlmann, C, Schneider, F, Arns, A, Eckl, M, Hoppen L, Wenz, F, Fleckenstein, J: Experimenteller Vergleich zwischen stereotaktischer Lungenbestrahlung mit volumenmodulierter Strahlentherapie (VMAT) und dynamisch-konformaler Bogenbestrahlung (DCAT) hinsichtlich Bestrahlungszeit und Planqualität. Poster at the 24th conference of the DEGRO, Leipzig, 2018, DOI: 10.1007/s00066-018-1301-7
14. Eckl, M, Giuliacci, A, Sevela, O, Wenz, F, Wertz, HJ: Evaluation of new gantry angle dependence correction factors for pre-treatment IMRT plan verification with MatriXX Multicube Lite and myQA. Poster at the "Jahrestagung der Biomedizinischen Technik und Dreiländertagung der Medizinischen Physik", Dresden, 2017, DOI: 10.1515/bmt-2017-5000 Biomed. Eng.-Biomed. Tech. 2017

10 ACKNOWLEDGEMENT

The completion of this PhD thesis would not have been possible without the encouragement, support and contributions of many people. Therefore, I wish to express my gratitude to

- my thesis supervisor Prof. Dr. Frederik Wenz for giving me the opportunity of working on this project and offering support for presenting my work at conferences of all kind. Moreover, I am grateful for being given the chance of starting my education as a medical physicist at the University Medical Center Mannheim and expanding on my knowledge since then.
- Dr. Jens Fleckenstein for proof-reading this thesis and the extraordinary as well as continuous support as my direct supervisor and project leader. Also with regard to work in clinical routine, it has been truly motivating and informative to work with you.
- Dr. Frank Schneider and Marvin Willam for their insightful work- and non-work-related discussions as well as their constant availability for support.
- Dr. Gustavo Sarria and Dr. Judit Boda-Heggemann for supporting all of our projects with their medical experience and always finding time to provide constructive input on any issue.
- Uwe Gros and Uwe Schröder from Elekta AB for always helping me in respect of any technical issues and sharing their knowledge of linac and CBCT systems.
- Nicolette O'Connell, Jiaofeng Xu, Gustav Meedt and Peter Voet from Elekta AB for their continuous support for the ADMIRE and Monaco research software, hence providing the basis for all of the presented results.
- my present and former colleagues of the physics team in the department of medical physics and radiation protection: Volker Steil, Dr. Anna Arns, Dr. Anika Jahnke, Dr. Lennart Jahnke, Dr. Hansjörg Wertz, Dr. Johannes Thölking, Dr. Florian Stieler, Dr. Sven Clausen, Dr. Martin Polednik, Carsten Ohlmann, Lena Mertens, Philipp Aumüller, Luis Probst, Hans Oppitz and Kerstin Siebenlist who created a motivating team atmosphere and contributed to the presented results.
- all other colleagues of the radiation oncology department who accompanied me in my scientific journey and made my time in Mannheim a valuable experience.
- all my friends for showing patience and helping me out in difficult moments.
- Leo for always being at my side during the last years and encouraging me like no one ever did.
- my parents for their unconditional support and love.